13TH PLANETARY CRATER CONSORTIUM MEETING

Program and Abstracts

LPI Contribution No. 2702

13TH PLANETARY CRATER CONSORTIUM MEETING

August 10–12, 2022
Boulder, Colorado/Virtual

Institutional Support

Lunar and Planetary Institute
Universities Space Research Association
Southwest Research Institute

Convener

Stuart Robbins
Southwest Research Institute

Science Organizing Committee

Michelle Kirchoff
Southwest Research Institute

Kassandra Martin-Wells
Ursinus College

Margaret Landis
Laboratory for Atmospheric and Space Physics, University of Colorado

Jamie Riggs
Northwestern University

Stuart Robbins
Southwest Research Institute

Lunar and Planetary Institute   3600 Bay Area Boulevard   Houston TX 77058-1113

Compiled in 2022 by

Meeting and Publication Services
Lunar and Planetary Institute
USRA Houston
3600 Bay Area Boulevard, Houston TX 77058-1113

This material is based upon work supported by NASA under Award No. 80NSSC20M0173. Any opinions, findings, and conclusions or recommendations expressed in this volume are those of the author(s) and do not necessarily reflect the views of the National Aeronautics and Space Administration.

The Lunar and Planetary Institute is operated by the Universities Space Research Association under a cooperative agreement with the Science Mission Directorate of the National Aeronautics and Space Administration.

ISSN No. 0161-5297

Abstracts for this meeting are available via the meeting website at

https://www.hou.usra.edu/meetings/crater2022/

Abstracts can be cited as

Author A. B. and Author C. D. (2022) Title of abstract. In *13th Planetary Crater Consortium Meeting,* Abstract #XXXX. LPI Contribution No. 2702, Lunar and Planetary Institute, Houston.

13TH PLANETARY CRATER CONSORTIUM MEETING

Agenda

Wednesday, August 10, 2022		
9:00 a.m.	Fourth Floor Conference Room	Introduction and Welcome; Planetary Crater Consortium Business
9:40 a.m.	Fourth Floor Conference Room	Lunar Craters
1:20 p.m.	Fourth Floor Conference Room	Martian Craters
3:40 p.m.	Fourth Floor Conference Room	Wrap-Up Discussion and PCC Business, Day 1

Thursday, August 11, 2022		
9:00 a.m.	Fourth Floor Conference Room	Introduction and Welcome; PCC Election Speeches
9:10 a.m.	Fourth Floor Conference Room	Laboratory and Modeling Experiments
12:30 p.m.	Fourth Floor Conference Room	Laboratory and Modeling Experiments (continued)
2:10 p.m.	Fourth Floor Conference Room	Lightning Round
2:55 p.m.	Fourth Floor Conference Room	Wrap-Up Discussion and PCC Business, Day 2

Friday, August 12, 2022		
9:00 a.m.	Fourth Floor Conference Room	Introduction and Welcome
9:05 a.m.	Fourth Floor Conference Room	Icy Bodies
10:50 a.m.	Fourth Floor Conference Room	Elections, Wrap-Up Discussion, and PCC Business, Day 3

Print Only

Wednesday, August 10, 2022
INTRODUCTION AND WELCOME; PLANETARY CRATER CONSORTIUM BUSINESS
9:00 a.m. Fourth Floor Conference Room

Times	Authors (*Presenter)	Abstract Title and Summary
9:00 a.m.	Robbins S. J. *	*Introduction and Welcome; Meeting Logistics*
9:05 a.m.	Canup R. M. *	*Welcome to Southwest Research Institute*
9:10 a.m.		*Brief Introduction of Attendees*
9:20 a.m.	Robbins S. J. *	*PCC Business: New Council Member, Follow-Up on Repeatability Experiment*
9:25 a.m.	Robbins S. J. *	*PCC as a Resource: Website Resources for Crater Databases, Tutorials, Anything Else?*
9:30 a.m.	Harwell M. L. *	*Other Resource: Crater Resource Wiki*

Wednesday, August 10, 2022
LUNAR CRATERS
9:40 a.m. Fourth Floor Conference Room
Chair: Margaret Landis

Times	Authors (*Presenter)	*Abstract Title and Summary*
9:40 a.m.	Powers L. T. * Dickinson A. Ways T. Martin-Wells K. S.	*Automatic Data Aggregation to Assist in the Systematic Classification of Small Lunar Craters* **[#2023]** Using automatically extracted data from lunar datasets, we attempt to capture key elements humans use in counting in order to develop a tool to assist human classification of craters below 5 km in diameter.
10:10 a.m.	Huang Y. H. * Riedel C. Soderblom J. M. Krein S. B. Orgel C. Hirabayashi M. Minton D. A.	*Understanding the Global Spatial Distribution of Impact Craters on the Moon Using the Buffered Non-Sparseness Correction Technique* **[#2019]** We present an updated global density map of all impact craters ≥20 km in diameter on the Moon using the buffered non-sparseness correction technique and apply statistical analyses to evaluate the global spatial distribution of those impact craters.
10:40 a.m.		Break

10:50 a.m.	Huffman M. R. * Singer K. N.	*Updates on the Search for Tertiary Craters (Secondary Craters of Secondary Craters) on the Moon* **[#2027]** We present a set of tertiary craters from a small, fresh primary crater to the SSW of Glushko crater on the Moon, and use it to provide a data-based check on scaling laws outside of the hypervelocity regime.
11:20 p.m.	Robbins S. J. *	*Progress Towards Deriving New Empirical Crater Production Functions for Volcanic Terrain on Mercury, Moon, and Mars* **[#2025]** A long-standing work / Must eventually be / Completed. Yes, soon ...
11:50 p.m.	Chertok M. A. * Lucey P. G. Costello E. S. Ireland S. M.	*The Mare Protolith Thickness and Competence: A Control of Rocky Crater Populations* **[#2003]** We examine craters with rocky ejecta across a range of mare units. We find that the abundance of rocky craters is independent of surface age, but may be influenced by the mechanical properties of the mare protolith.
12:20 p.m.		Break

Wednesday, August 10, 2022
MARTIAN CRATERS
1:20 p.m. Fourth Floor Conference Room
Chair: Kassie Martin-Wells

Times	**Authors (*Presenter)**	***Abstract Title and Summary***
1:20 p.m.	Conrad J. W. * Fassett C. I.	*Using Secondary Craters to Assess Strength Differences Between Neighboring Surface Units* **[#2012]** Secondary craters can be of use in estimating contrasts of neighboring units material properties. When the necessary observations coincide, the clear differences in the crater distribution can translate to value ratios with crater scaling equations.

1:50 p.m.	Boatwright B. D. * Head J. W. Kreslavsky M. A.	*Topographic Diffusion of Impact Craters on Mars: Sources, Atmospheric Effects, and Dependence on Climate* **[#2007]** We describe advances in modeling topographic diffusion on Mars due to impact bombardment. Nonlinear scaling of degradation rates due to crater emplacement and production, filtering of impactors as a function of atmospheric pressure are discussed.
2:20 p.m.		Break
2:30 p.m.	Landis M. E. * DeCoster M. E. Stickle A. M. Rivera-Valentín E. G.	*Preliminary Results from Crater Mapping and Analysis for the South Polar Layered Deposits, Mars* **[#2020]** We present initial results from mapping, statistical analysis, and shock physics modeling to understand the impact crater population, and therefore geologic history, of the south polar layered deposits, the largest surface ice sheet on Mars.
3:00 p.m.	Boyce J. M. * Mouginis-Mark P. J.	*Why Ramparts of Martian Impact Crater are High Relief?* **[#2005]** The unusually high-relief ramparts of martian crater ejecta are caused by the influence of the impact process on the processes that control the flow of dense, polydispersive granular debris like impact ejecta, landslides and debris flows.
4:30 p.m.		Break

Wednesday, August 10, 2022
WRAP-UP DISCUSSION AND PCC BUSINESS, DAY 1
3:40 p.m.   Fourth Floor Conference Room
Chairs: Stuart Robbins and Rachael Hoover

Times	Authors (*Presenter)	Abstract Title and Summary
3:40 p.m.	Boyce J. M. *	*Nomenclature Committee Report, Request for Volunteers to Lead Nomenclature Committee*
3:50 p.m.		Discussion

Thursday, August 11, 2022
INTRODUCTION AND WELCOME; PCC ELECTION SPEECHES
9:00 a.m.   Fourth Floor Conference Room

Times	Authors (*Presenter)	Abstract Title and Summary
9:00 a.m.	Robbins S. J. *	*Introduction and Welcome; Meeting Logistics; PCC Election Nomination and Speeches*

Thursday, August 11, 2022
LABORATORY AND MODELING EXPERIMENTS
9:10 a.m. Fourth Floor Conference Room
Chairs: Jamie Riggs and Margaret Landis

Times	**Authors (*Presenter)**	***Abstract Title and Summary***
9:10 a.m.	Marchi S. * Alexander A.	*Heavy Metal Cratering: Impact Experiments and Simulations in Fe-Ni Alloys* **[#2022]** We study cratering in heavy metals.
9:40 a.m.	Holmes M. C. * Caldwell W. K.	*Modeling Micrometeorite Bombardment into Metal Targets Using the FLAG Hydrocode* **[#2009]** We summarize preliminary results obtained using parameters typical for problems of interest, and we discuss our research plan, which upon execution should improve our understanding of the effects of high strain rates or shock conditions on materials.
10:10 a.m.		*Break and Group Photo*
10:30 a.m.	Caldwell W. K. * Hunter A. Plesko C. S.	*Exploring Porosity in Asteroid 16 Psyche with 3D Hydrocode Modeling of Its Deepest Impact Structure* **[#2010]** We present 3D modeling of Psyche's deepest impact structure to better understand its porosity composition. We consider uniform microporosity, layered microporosity, and rubble piles.
11:00 p.m.	Runyon K. D. * Barnouin O. S. Tsang C. Durda D. D. Ernst C. M. Smith H. T. Martin A. Nguyen A. Klein V.	*Reduced Gravity Ejecta Emplacement Experiments* **[#2008]** Reduced Gravity / Catapult the ejecta / Does ejecta scale?
11:30 p.m.		Break

Thursday, August 11, 2022
LABORATORY AND MODELING EXPERIMENTS (CONTINUED)
12:30 p.m. Fourth Floor Conference Room
Chairs: Jamie Riggs and Margaret Landis

Times	Authors (*Presenter)	*Abstract Title and Summary*
12:30 p.m.	Alexander A. M. * Johnson B. Marchi S.	*Crustal Fragmentation from the Chicxulub Impact: Preliminary Results* **[#2024]** We use a newly modified version of iSALE to simulate the Chicxulub formation event, using input parameters from literature and compare particular outputs to observational data (e.g., peak ring porosity and block size as measured by seismic and drill core data).
1:00 p.m.	Boslough M. B. * Schultz P. H. Harris R. S.	*Hypervelocity Airburst Shower Formation of the Pica Glass* **[#2021]** Computational shock physics models demonstrate that multiple discrete low-altitude airbursts from a small comet that fragmented upon low-angle entry into the atmosphere is compatible with the distribution and extent of the Pica Glass.
1:30 p.m.	Harwell M. L. * Stewart S. T. Citron R. I. Caldwell W. K. Plesko C. S.	*Regime Tracking and Benchmarks for the Impact Modeling Community* **[#2028]** We introduce a method of tracking rheology regimes activated in the cratering process in real time and discuss rheological benchmark problems for the impact modeling community.
2:00 p.m.		Break

Thursday, August 11, 2022
LIGHTNING ROUND
2:10 p.m. Fourth Floor Conference Room
Chairs: Kassie Martin-Wells

Times	Authors (*Presenter)	*Abstract Title and Summary*
2:10 p.m.	Hoover R. H. * Robbins S. J. Hynek B. M.	*Update on the Morphometric Measurements for the Robbins Lunar Crater Database* **[#2030]** Update and current status on the morphometric measurements for lunar craters for the Robbins lunar crater database.

2:25 p.m.	Burgener J. A. *	*Update on Our Software Simulating Low Angle Skip Impacts — Now 3D and Showing the Ejecta Secondary Impacts* **[#2002]** Presenting 3D software for low angle impacts and associated secondary impacts on Earth. Shows the secondary impact angles, speed, orientation, crater shape. Demonstrates Lake Michigan may be a skip impact, Carolina Bays its secondary craters.
2:40 p.m.	Schedl A. *	*Tracking Incremental Strain Histories as a Shock Wave Passes Through Rocks During Meteorite Impact Using Calcite Twin Analysis* **[#2029]** Recent modeling papers have examined the stress and strain during shock metamorphism. This paper compares these models to the incremental strains determined using calcite twin analysis. Results are used to measure the amount of erosion of a crater.

Thursday, August 11, 2022
WRAP-UP DISCUSSION AND PCC BUSINESS, DAY 2
2:55 p.m. Fourth Floor Conference Room
Chairs: Stuart Robbins and Rachael Hoover

Times	*Abstract Title and Summary*
2:55 p.m.	Discussion

Friday, August 12, 2022
INTRODUCTION AND WELCOME
9:00 a.m. Fourth Floor Conference Room

Times	Authors (*Presenter)	Abstract Title and Summary
9:00 a.m.	Robbins S. J. *	*Introduction and Welcome*

Friday, August 12, 2022
ICY BODIES
9:05 a.m. Fourth Floor Conference Room
Chairs: Stuart Robbins

Times	Authors (*Presenter)	*Abstract Title and Summary*
9:05 a.m.	Rossignoli N. L. * Di Sisto R. P.	*Modeling a Planetocentric Source of Impactors for the Uranian Satellites* **[#2017]** We model a planetocentric source of impactors for the mid-sized uranian satellites and compare our results with updated crater counts.

9:35 a.m.	Crósta A. P. Silber E. A. * Lopes R. M. C. Malaska M. J.	*Large Impacts on Icy Bodies s a Feasible Mechanism for Inducing Habitability: The Case of Menrva Crater on Titan* **[#2018]** We examined the role of large impacts on Titan in creating habitable conditions by simulating the formation of Menrva crater and investigating its potential role in creating niches for the development of primitive lifeforms.
10:05 a.m.	McKinnon W. B. * Schenk P. M. Bland M. T. Singer K. N. Robbins S. J.	*Viscous Relaxation of Craters on Pluto: Possible Indication of Early High Heat Flow* **[#2026]** We explore both the evidence for viscous relaxation of large impact craters on Pluto as well as implications for the history of heat flow on the dwarf planet.
10:35 a.m.		Break

Friday, August 12, 2022
ELECTIONS, WRAP-UP DISCUSSION AND PCC BUSINESS, DAY 3
10:50 a.m.   Fourth Floor Conference Room
Chairs: Stuart Robbins and Rachael Hoover

Times	Authors (*Presenter)	*Abstract Title and Summary*
10:50 a.m.		Discussion
11:50 p.m.	Martin-Wells K. *	*PCC Business: Elections for Council, Nomination/Election/Appointment for Nomenclature Committee Chair*
12:10 p.m.	Robbins S. J. *	*PCC Business: 2023 Meeting*

PRINT ONLY

Authors (*Denotes Presenter)	*Abstract Title and Summary*
Burt D. M.	*Distinguishing Impactoclastic from Pyroclastic Layered Rocks on Mars* **[#2031]** Martian layered impactoclastic deposits may be difficult to distinguish from those deposited by pyroclastic (volcanic) processes. Both can resemble those formed by water or wind-driven flows. Sample return may be needed for differentiation.
Leliwa-Kopystynski J. Wlodarczyk I.	*The Sizes of Impactors that Formed Asteroids Families* **[#2004]** From well-known, poorly known, or assumed values of physical parameters of the asteroid families members we reconstructed the sizes of impactors that produced 13 families. Impactors that formed Vesta, Eunomia, and Adeona families had sizes 8 km.

Moore R. B.	*Decaying Oblique Orbits as a Hypothesis for the Origin of Nearly Horizontal Impact Craters — A Survey of Some Candidate Paterae on Mars* **[#2011]** Factors influencing the occurrence of nearly horizontal impact craters are discussed hypothetically and tested by tabulating a set of 13 such craters on Mars over 20 km long. It is observed that these have headings >35deg from the equatorial plane.
Pathare A. V. Russell A. Howard A. Morgan G. Perry M. Putzig N.	*The Modification of Udzha Crater in the Martian North Polar Layered Deposits* **[#2016]** Our 3D SHARAD radargram mapping of the near-surface stratigraphy within Udzha Crater in the Martian North Polar Layered Deposits suggests possible localized episodes of preferential deposition and erosion within the Udzha Crater cavity.

Table of Contents

13TH PLANETARY CRATER CONSORTIUM MEETING

Abstracts

Crustal fragmentation from the Chicxulub impact: preliminary results

A. M. Alexander[1,2], B. Johnson[3] and S. Marchi[1], [1]Southwest Research Institute, Boulder CO, 80301, [2]University of Colorado Boulder, Boulder CO 80309, [3]Purdue University, West Lafayette IN 47907

Introduction:

Chicxulub is one of most studied terrestrial impact craters. Access to a wealth of geophysical data (e.g., seismic data, drill cores, [1-4]) have allowed researchers to build a detailed understanding of Chicxulub's formation. Prominent features, such as the downward dipping of a pre-impact sedimentary layer (modeled as calcite) overlain by pre-impact granitic basement approximately 40-50 km from the crater center, as well as composition and porosity measurements of the peak ring material, are key benchmarks when comparing numerical simulations with the actual structure. Seismic and drill core data indicate that the peak ring material is sourced from the overlying granitic basement material with the presence of significant porosity (up to 20%) and block size which decreases with depth (i.e., smaller fragments deeper).

In this work, we have simulated the Chicxulub formation event using a newly-implemented iSALE [5-7] subroutine that includes tensional fragmentation and porosity [8-9]. We have performed a suite of high resolution, 2D iSALE simulations (up to 80 cell-per-projectile-radius) using input parameters from previously successful simulations (e.g., [10]), and studied the resulting subsurface porosity and block size. The preliminary results will be presented at the meeting, and compared with available data from drill cores.

References:

[1] Morgan, J.V. et al., (2000) *Earth Planet. Sci. Lett. 183, 347–354.* [2] Morgan, J. V. et al., (2011) *J. Geophys. Res. 116, B06303*. [3] Morgan, J. V. et al., (2017) *Proceedings of the International Ocean Discovery Program 364*. [4] Gulick, S. P. S. et al., (2008) *Nat. Geosci. 1, 131–135*. [5] A. Amsden et al. (1980) *Los Alamos National Laboratories Report*, LA-8095:101p. [6] G. Collins et al. (2004) *Meteoritics and Planetary Science*, 39, 217. [7] K. Wünnemann et al. (2006) *Icarus* 180, 514. [8] Wiggins, S.E., et al., (2019) *JGR: Planets 124, 4, 941-957.* [9] Wiggins, S.E., et al., (2021) *LPSC LPI Contribution No. 2548, id.2307*. [10] Rae, A. S. P. et al., (2019) *JGR: Planets 124, 2, 396-417.*

TOPOGRAPHIC DIFFUSION OF IMPACT CRATERS ON MARS: SOURCES, ATMOSPHERIC EFFECTS, AND DEPENDENCE ON CLIMATE.

Benjamin D. Boatwright[1], James W. Head[1], and Mikhail A. Kreslavsky[2], [1]Dept. of Earth, Environmental, and Planetary Sciences, Brown University, Providence, RI 02912 USA, [2]Dept. of Earth and Planetary Sciences, University of California Santa Cruz, Santa Cruz, CA 95064 USA (benjamin_boatwright@brown.edu).

Introduction: The Moon is the most well understood of the terrestrial planetary bodies in terms of the quantitative effects of impact cratering on surface evolution through geologic time [1-4]. These studies have used largely empirical methods to determine, with certain caveats, that linear topographic diffusion provides the closest approximation to the process of steady-state lunar landform evolution.

Diffusion on Mars has usually been parameterized to match observations of background weathering rates not accounted for by processes such as fluvial bedrock detachment and is assumed to proceed at a quasi-constant rate [5-8]. This “black box” approach has limited application when attempting to distinguish between diffusive mechanisms despite the close coupling between many of these proposed mechanisms and climate.

Rainsplash, the ballistic action caused by individual falling droplets upon sediment grains, has been the *de facto* explanation for diffusive degradation on Mars, at least early in its history [9]. However, topographic diffusion can also occur through solifluction and gelifluction, which would require subfreezing climates [7], or can occur completely independently of climate, such as through impact cratering, as observed on airless bodies such as the Moon.

Here, we investigate the specific effects of diffusive degradation through impact bombardment on Mars. We explore a range of basic assumptions regarding the scaling of crater size-frequency distributions and the presence of an atmosphere to determine how these factors may have affected Mars landform evolution.

Crater size-frequency distributions and scaling laws: The net downslope volume flux due to crater emplacement is proportional to the topographic slope, which results in diffusive motion when mass is conserved [1,3]. True linear diffusion is scale-independent, i.e. the topographic diffusivity k is constant. However, studies of topographic diffusion on the Moon have revealed that crater degradation is better described by a scale-dependent process. This phenomenon is known as “anomalous” diffusion and is due primarily to the nonlinear nature of crater production and emplacement [3,10]. These nonlinear effects on the degradation state K (time-integrated diffusivity, $K = \int k\,dt$) [3,4] can be expressed as a power law function of the crater diameter D, $\boldsymbol{K \propto D^{\alpha}}$. The exponent α will depend on 1) a degradation function for each individual crater, and 2) the production function for all craters in the diffusive population. The exponents are defined as $\psi + 2$ for the degradation function and $-\eta$ for the production function, $\boldsymbol{\alpha = \psi + 2 - \eta}$ [4]. A likely range of $1 \leq \psi \leq 2$ is derived from both physical and empirical constraints [4]. The crater production function N for Mars contains separate power law branches according to crater size, $N \propto D^{-\eta}$, with a range of $1.8 \leq \eta \leq 3.8$ [11].

The landscape scale in question will implicitly determine the maximum crater size D_{max} that does geomorphic work within a diffusive crater population. On Mars specifically, the minimum crater size D_{min} depends on the introduction of atmospheric drag, which will curtail the impactor population according to the atmospheric pressure, gravity, and physical properties of the impacting body, $\boldsymbol{L = 0.15P/\rho g \sin\theta}$ [12]. L is the minimum bolide diameter (m) that reaches the ground at hypersonic velocity for a given atmospheric pressure P (pascals, 10^{-5} bar); ρ is the impactor density, taken to be 3000 kg/m^3 for an average basaltic composition; g is the acceleration due to gravity, 3.71 m/s^2 for Mars; and θ is the average impact angle, taken to be 45° [13]. For a given L, and assuming a similar target and impactor density, $\boldsymbol{D_{min} = 1.16L^{0.78}(v\sin\theta)^{0.44}g^{-0.22}}$ [14]. v is the average impact velocity, taken to be 9600 m/s [13].

The relative effects of the different combinations of ψ and η on the degradation state K are explored in Fig. 1. When $\psi + 2 - \eta = 0$, the degradation state’s dependence on D vanishes and K is constant (Fig. 1, solid diagonal line), as would be the case for linear diffusion. On either side of this dividing line, the relative influence of smaller vs. larger craters within the diffusive population is magnified. The regions $\psi < 1$, $\alpha < 0$ are considered physically implausible and shaded red in Fig. 1. Likewise, areas that are beyond the range of $1.8 \leq \eta \leq 3.8$ predicted for the Mars crater population are shaded yellow.

The effects of atmospheric filtering upon impact-induced diffusion are felt more strongly for smaller values of α (Fig. 1, arrow pointing upward toward the $\alpha = 0$ limit). Likewise, for fixed values of ψ and η, larger craters will experience relatively smaller decreases in their degradation state for a given pressure

P because less of their total diffusive population is removed by atmospheric filtering. Table 1 gives the calculated values for L and D_{min} over a range of theoretical atmospheric pressures for Mars. Atmospheric filtering would have played a more significant role early in Mars geologic history when the atmospheric pressure was highest [15]. However, due to the likelihood that $\alpha \gg 0$ for Mars (as observed on the Moon), the presence of an atmosphere should make relatively little difference in the overall effect of impact-induced topographic diffusion.

Outstanding questions: Craters on Mars are known to degrade diffusively, but the exact mechanisms responsible for this degradation have remained largely undetermined. We have explored a few basic assumptions regarding diffusive degradation of craters on Mars, including the effects of atmospheric filtering and crater size-frequency distributions. Below, we pose some of the major outstanding questions that have been raised by these observations.

1. How do predicted diffusive degradation rates compare to observed degradation states of craters on Mars? In order to assess the diffusive degradation state of craters on Mars, morphometric parameters relating to diffusion must be matched with a predicted evolution of these parameters as a function of time. Numerical diffusion model results on fresh crater topography, with input parameters derived from the theoretical predictions we have outlined above, could be used to obtain a theoretical evolution function of topographic curvature or other relevant values. This function could then be compared to similar measurements on actual crater topography to determine the degradation state of a given crater population, and what this would imply for both the duration and intensity of diffusive degradation brought about by impact bombardment under different initial conditions.

2. What can predictions of diffusive crater degradation on Mars tell us about early climate? The major outstanding question relating to diffusive degradation of craters on Mars is its source. Depending on the answer, this could have major implications for the climatic conditions under which the degradation occurred. Previous studies of Mars crater degradation have generally assumed that diffusive degradation occurred through the action of rainsplash from liquid precipitation in a warm and wet early Mars climate [5-8]. Decreasing atmospheric pressure throughout the Noachian could explain the transition from primarily diffusion- (rainsplash-)dominated to runoff-dominated fluvial erosion [9], but these results have been called into question [16]. If impact bombardment is demonstrated to be a major contributing factor to the diffusive degradation of craters on early Mars over a range of plausible atmospheric pressures, then traditionally accepted warm climate mechanisms such as rainsplash may be less important, allowing the possibility of diffusive crater degradation without the presence of liquid water.

References: [1] Soderblom L.A. (1970) JGR 75; [2] Craddock R.A., Howard A.D. (2000) JGR 105; [3] Fassett C.I., Thomson B.J. (2014) JGR 119; [4] Minton D.A. et al. (2019) Icarus 326; [5] Howard A.D. (1994) Water Resources Res. 30; [6] Craddock R.A. et al. (1997) JGR 102; [7] Craddock R.A., Howard A.D. (2002) JGR 107; [8] Forsberg-Taylor N.K. et al. (2004) JGR 109; [9] Craddock R. A., Lorenz R. D. (2017) Icarus 293; [10] Fassett C. I. et al. (2018) LPSC 49; [11] Hartmann W. K. (2005) Icarus 174; [12] Ivanov B.A. (2001) Chron. Ev. Mars; [13] Melosh H.J. (1989) Oxford U. Press; [14] Schmidt R. M., Housen K. R. (1987) Int. J. Impact Eng.; [15] Warren A. O. et al. (2019) JGR 124; [16] Palumbo A. M. et al. (2020) Icarus 347.

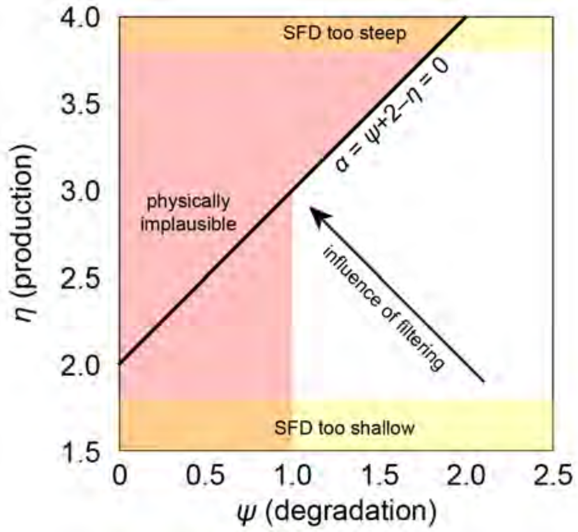

Figure 1. Relative effects of the exponents of ψ and η on the degradation state K for Mars.

P **(bar)**	***L*** **(m)**	D_{min} **(m)**
0	0	0
0.006 (modern-day)	0.01	1.3
0.1	0.2	12
0.5	1	40
1.5 [15]	3	100

Table 1. Minimum bolide and crater diameters for different Mars atmospheric pressures.

HYPERVELOCITY AIRBURST SHOWER FORMATION OF THE PICA GLASS.

Mark Boslough[1,2], Peter H. Schultz[3], R. Scott Harris[4], [1]Verification and Analysis, XCP-8, Los Alamos National Laboratory, Los Alamos, New Mexico, 87545, [2]Dept. of Earth and Planetary Sciences, University of New Mexico, MSC O3-2040 Albuquerque, NM 87131-0001, mbeb@unm.edu [3]Dept. of Earth, Environmental, and Planetary Sciences, Brown University; P.O. Box 1846, Providence, Rhode Island 02912, [4]Dept. of Space Sciences, Fernbank Science Center; 156 Heaton Park Drive, Atlanta, Georgia 30307.

Abstract: The recently discovered Pica Glass in the Atacama Desert, Chile [1] (Fig. 1) requires rapid heating and quenching of surface materials by multiple airburst fireballs. Based on the surviving mineral assemblages from the object, the most likely scenario involves cascading fragmentation of a comet that broke up upon low-angle entry into the atmosphere. Modeled low-altitude airbursts from six fragments of a single 120-m diameter comet generated separate airbursts in roughly aligned and discrete glass sites that spanned more than 70 km. This scenario is not a unique solution; there are tradeoffs among speed, size, strength, and height of burst. The Pica Glass, because of its young age, provides useful ground truth for airburst simulations in support of planetary defense risk assessment. Computational shock physics models demonstrate that multiple discrete low-altitude airbursts from a small comet that fragmented upon low-angle entry into the atmosphere is compatible with the distribution and extent of the Pica Glass. Such a scenario has a sufficiently high probability that it is compatible with the young age of the glass, and is also relevant to airburst risk assessment for planetary defense.

Fig. 1: Twisted and folded glasses occurring in the Chipana region on the Atacama Desert.

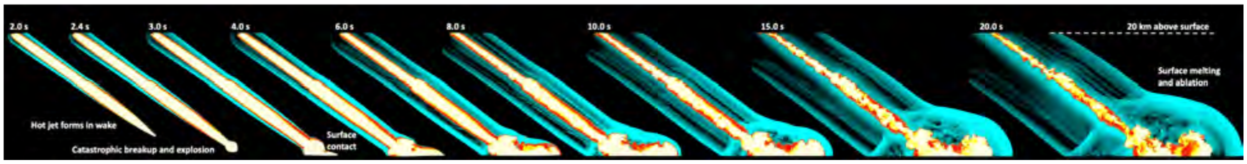

Fig. 2: 100-meter asteroid enters atmosphere at 35° elevation angle and 14.2 km/s (30 Mt kinetic yield) and explodes 2 km above surface. Type-2 "contact airburst" subjects the surface to a supersonic vapor jet that exceeds silicate melting temperature. Time relative to simulation start is shown for each frame.

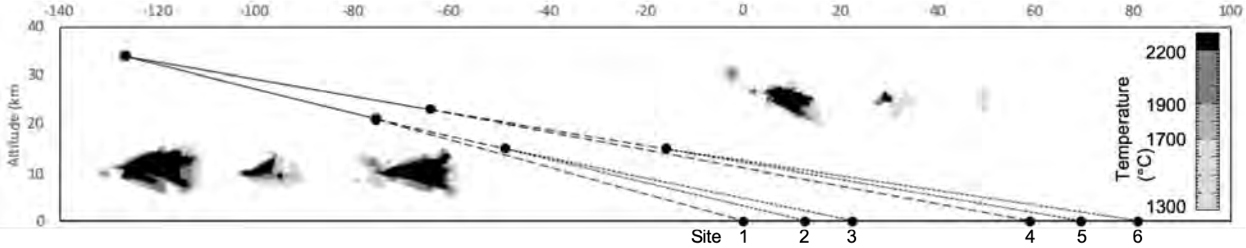

Fig. 3: Cascading fragmentation scenario defining simulation conditions for six Pica Glass sites. Solid circles are binary fragmentation locations and lines are trajectories with dashes indicating fragment level. Maximum surface temperature maps are in order of site number at 4x scale with fragments coming from left (north).

Single Airburst/Surface Interaction: (Fig. 2). The most probable asteroid entry elevation angle is 45° and the best model-based estimate for the 1908 Tunguska airburst is 35° [2]. However, there is no evidence that the hot vapor jet at Tunguska reached the surface, suggesting that it was a small object (~40 m diameter and ~5 Mt kinetic yield). A larger object would explode at lower altitude and contain enough mass and momentum for the high-temperature jet to descend to the surface. An object entering at that angle, however, would not melt the surface at widely separated locations. The Libyan Desert Glass probably formed by this mechanism [3] but has had 29 million years to be transported over the large area which it now occupies.

Multiple Airburst/Surface Interactions: An object with given size, velocity, and physical properties, can enter on a shallow (but not grazing) trajectory and undergo a cascading fragmentation that disperses fragments along its ground track (Fig. 3). Some of the fragments are large and strong enough to burst at low altitude and yield very hot fireballs directed downward to interact with the surface, thereby generating separate glass concentrations over a distance that spans over 70 km (Fig. 4). This represents our currently favored scenario that is the basis for our model. Further constraints, however, will emerge from ongoing geologic studies.

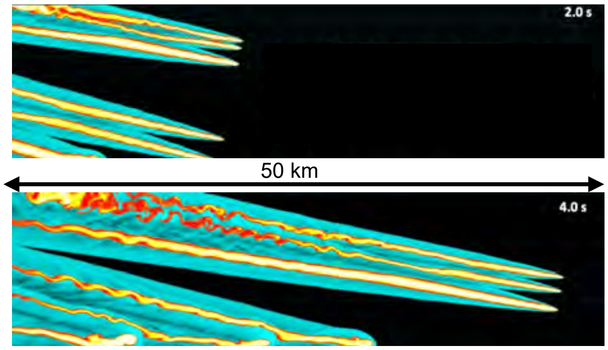

Fig. 4: Swarm of six objects generated by fragmentation cascade starting from single 120-m diameter object that begins breaking up at altitude of 35 km resulting in six discrete glass sites spanning distance of 70 km along track.

Two Types of Low Altitude Airburst: (Fig. 5). A low-altitude airburst generates a high-velocity, high-temperature jet of meteoritic vapor "fireball" that either stops before it reaches the surface (Type 1 non-contact airburst) or descends to and interacts with the surface (Type 2 contact airburst), [4]

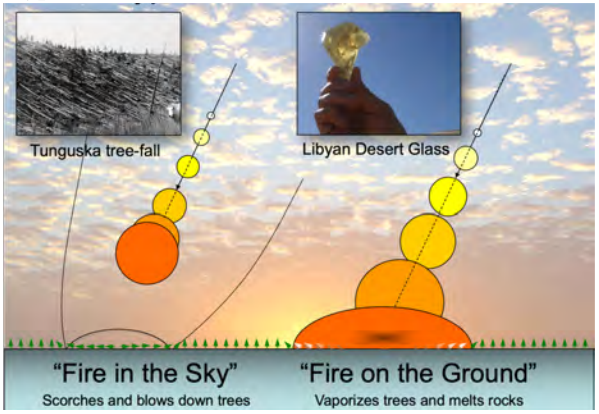

Fig. 5: Two types of low-altitude airburst.

Conclusions: Computational shock physics models demonstrate that multiple discrete low-altitude airbursts from a small comet that fragmented upon low-angle entry into the atmosphere is compatible with the distribution and extent of the Pica Glass. Such a scenario has a sufficiently high probability that it is compatible with the young age of the glass, and provides insight for the potential risks from low-altitude airbursts.

Acknowledgments: This work was supported by the US Department of Energy through the Los Alamos National Laboratory. Los Alamos National Laboratory is operated by Triad National Security, LLC, for the National Nuclear Security Administration of U.S. Dept. of Energy (Contract No. 89233218CNA000001). Additional funding provided by NASA/SSERVI.

References:

[1] Schultz, P. H. et al. (2021). *Geology*, *50*, 205–209. [2] Boslough M. B. and Crawford D. A. (1997). *Annals NY Acad. Sci, 822*, 236-282. [3] Boslough M. B. and Crawford D. A. (2008). *Int. J. Impact. Engng*, *35*, 1441-1448. [4] Boslough M. B. (2013). *Acta Astronautica,* doi:10.1016/j.actaastro.2013.09.00.

Why ramparts of Martian impact crater are high relief?

Joseph M. Boyce, and Peter J. Mouginis-Mark, Hawaii Institute of Geophysics & Planetology, University of Hawaii, Honolulu, HI 96822.

Introduction: One of the diagnostic features on Martian ejecta are rampart ridges that occur at the distal edge of each ejecta layer (Figure 1). These features also occur on impact crater ejecta of other planetary bodies, as well [1, 2]. [3, 4] found that the height of the rampart relative to the flow thickness of outer most Martian ramparts (the relief) of Martian craters is nearly 2 times greater than that of ridges formed on the other types of granular flows (Figure 2). We propose that this is due to the production of an unusually high volume fraction of large particles in the ejecta flows combined with the relatively high velocity of the ejecta flows (compared with that of geophysical flows).

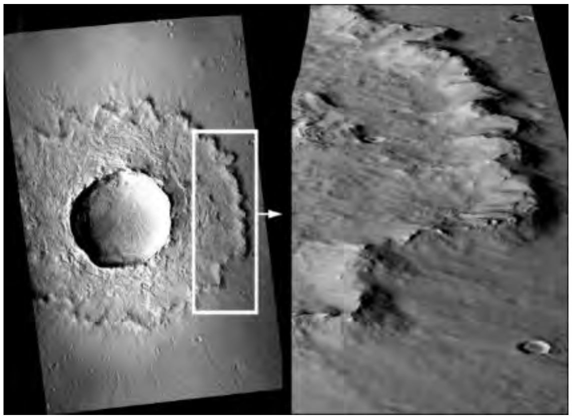

Figure 1. Examples of high relief ramparts on a SLE crater located at 36.35N, 80.54E. CTX image B04_011287_2163.

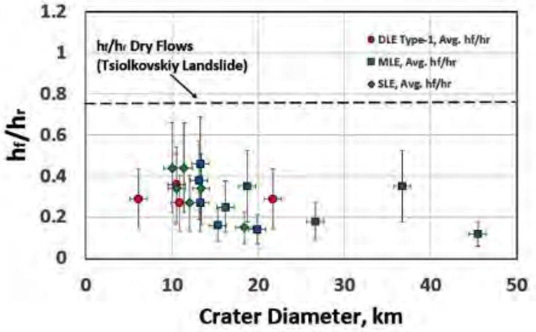

Figure 2. The ratio of flow bodies thickness (h_f) to thickness of the outermost ramparts (h_r) (i.e., relief) of the ramparts of 17 example fresh Martian craters of different types, and an example of a long runout, dry geophysical flow (Tsiolkovsky). This shows that relief of Martian ramparts are about a factor of ~ 2 greater than dry landslide ramparts. In addition, [3] found that rampart height did not vary across Mars indicating that it was incentive to location. The error bars are the standard deviation of the average measurement values [4].

Discussion: Granular flow studies provide valuable insight into formation of Martian ejecta ramparts, as well as ramparts on geophysical flows such as landslides, debris flows and pyroclastic density currents. Because both geophysical flows and ejecta flows are composed of poly-dispersive granular debris, the same physics and flow processes govern the flow of both [5, 9]. These studies have shown that if the flows contain high enough volume fraction of large particles, then these particles will accumulate at the flow fronts, and be pushed along as a dam of coarse particles [9]. If there is an unusually high volume fraction of large particles, then relatively more will accumulate at the flow front resulting in an unusually high volume dam. Upon halting, the flow body typically drains back from the flow front, leaving it standing as a rampart composed principally of large particles [10]. If the flow body contains substantial water, then after the flow drains away from the rampart, the water will leak from the flow, densifying (compacting) it and enhancing the relief between the flow body and rampart. However, this can account for > 10 % volume loss [12].

Similar to geophysical flows, the volume fraction of large particles in ejecta is of critical importance in producing ramparts, and, in particular, large volume ramparts. While slope collapse, volcanic eruptions, or primary impact events produce abundant coarse-grain particles, secondary craters [13, 14] generate even more large particles for a given volume of debris [14, 15]. This is because the relatively low velocity of secondary impacts subjects the target to low peak stress that causes greater spacing between fractures, and hence large particles (Figure 3) [14, 15]. While, thermal inertia data does not detect large particles in all ramparts, this is probably due to the dustiness of the Mars surface. In addition, ramparts typically do not form on ejecta blankets of craters on bodies whose surface have low-volatile content (e.g., the Moon), but they do form on long runout landslides on these bodies [16, 17]. We suggest that this is because for ramparts to form on ejecta, the ejecta must runout far enough to allow the rampart forming processes to fully operate. This suggests that the fluidization of Martian ejecta was also required for rampart production.

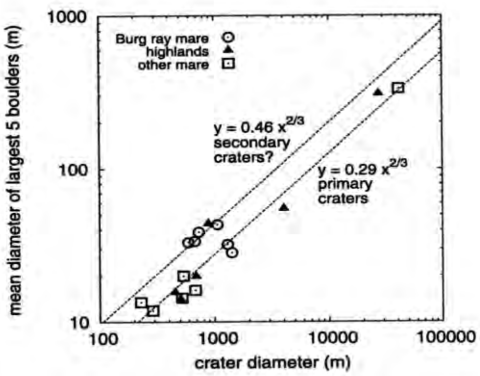

Figure 3. Comparison of the average diameter of five largest blocks around secondary craters on a ray from Burg crater and from primary craters nearby [15]. The upper line fits through craters on the Burg ray thought to be secondaries. The lower line fits through mare craters not on the ray from the crater Burg and thought to be primary craters.

In addition, the entire mass of geophysical flows typically starts movement at nearly the same time and from a local source. As a result, the velocity of particles and distribution of mass in these flows as the spread typically decrease with distance from the source [18]. In contrast, during impact crater formation, target material is ejected from the crater systematically outward from the point of impact until the kinetic energy drops below the strength of the target materials and ejection stops [19, 20]. Consequently, the first material ejected from the crater has the highest velocity and thrown furthest, while the last material ejected is the lowest velocity, and barely makes it out of the crater. These materials are eject along ballistic trajectories, which results in a cone-shaped ejecta curtain where the highest velocity ejecta particles land furthest away from the crater rim and the slowest at the crater rim. When this ejecta strikes the surface their vertical velocity component cancels out, but the horizontal component is relatively unaffected. As a result, the ejecta can produce an ejecta flow whose velocity distribution is initially the reverse of the velocity distribution in geophysical flows with the fastest flowing material further away from the rim. This means that, unlike most gravity-driven geophysical flow, inertia-driven ejecta flows are higher velocity throughout most of their radial flow compared with geophysical flows. As a result, the higher velocity of these flows would create a high hydraulic head within the flows that is capable of pushing the flow front and its large particles to build high ramparts.

Conclusions: Ramparts on Martian layered ejecta craters are unusually high relief because of the influence of ejecta emplacement processes. The two main factors responsible for building these high-relief ramparts are 1) the unusual high volume fraction of large particles in the ejecta flows produced by secondary cratering and 2) the high velocity of the Martian fluidized ejecta flows that provide the kinetic energy required to push large particle to the top of high ramparts.

References: [1] Boyce, J. et al., 2010, MAPS 45; 661; [2] Robbins et al., 2017, Icarus 287, 187–206.; [3[Mouginis-Mark, P., Baloga, S., 2006, MAPS 41, 10, 1469-1482; [4] Boyce, J., & Mouginis-Mark, P., 2018, LPSC, ab. 1116; [5] Forterre, Y., & Pouliquen, O., 2008; Annu. Rev. Fluid Mech. 40, 1–24. **[6]** Gray J. et al., 2008; [7] Iverson, R., et al., 2010, JGR, doi: 1029/2009 JF001514; [8] Johnson et al., 2012, JGR, 117, F01032, doi:10.1029/2011JF002185; [9] Gray, J., & Ancey, C., 2009, J. Fluid Mech., 629, 387–423, doi:10.1017/S0022112009006466; [10] Felix, G. & Thomas, N. 2004, Earth Planet. Sci. Lett., 221, 197-213; [12] Branney, M. & Kokelaar, P., 2002, Memoir of the Geo. Soc. of London, 152 p; [13] Oberbeck, V., 1975, Rev. Geophys. Space Phys. 13, 337–362.; [14] Collins et al., 2004, Met. & Planet Sci. 39, 217-231; [15] Bart and Melosh, H. J., 2007, Geophys Res. Ltr., 34, L07203, doi:10.1029/2007GL029306; [16] Boyce J., & Mouginis-Mark, P., 2019, LPSC Ab. 1065; [17] Schmidt B., et al., 2017, Nature, DOI:10.1038; [18] Simpson, 1997, Cambridge Univ. Press.; [19] Melosh, J., 1989, Oxford Univ. Press, N Y.; [20] Osinski et al., 2011, Earth &Planet. Sci. Lett. 310, 167–181.

UPDATE ON OUR SOFTWARE SIMULATING LOW ANGLE SKIP IMPACTS – NOW 3D AND SHOWING THE EJECTA SECONDARY IMPACTS.

John Burgener. Telegistics Inc. 944 Meadow Wood Rd., Mississauga, Ontario, Canada, L5J2S6. Email: john@burgener.ca.

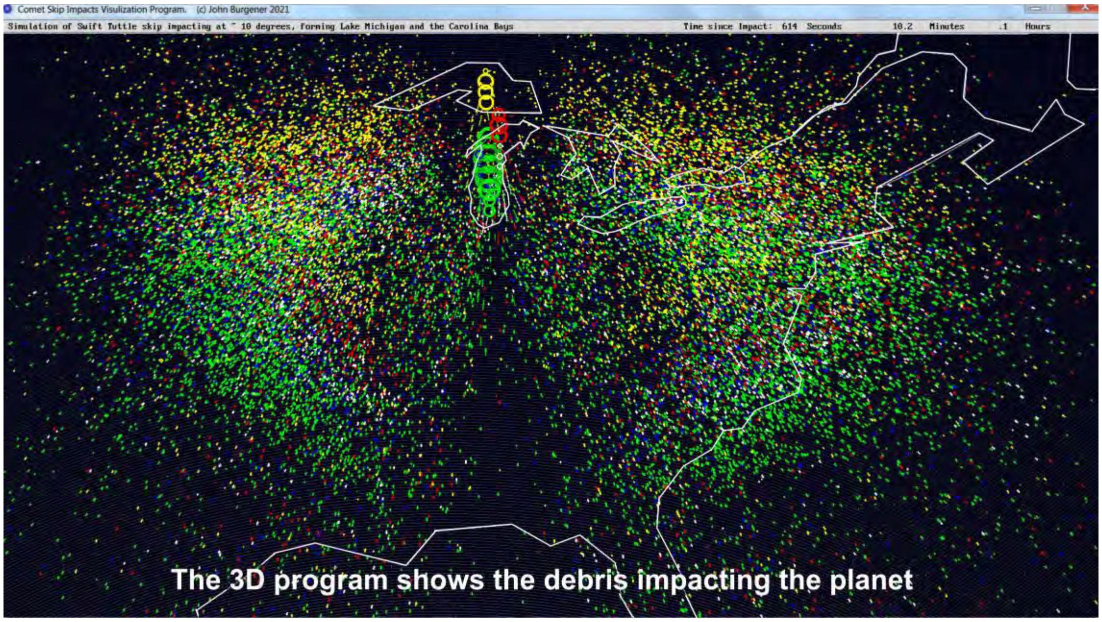

Comet Skip Impacts Visulization Program. (c) John Burgener 2021

```
Simulation of Swift Tuttle skip impacting at ~ 10 degrees, forming Lake Michigan and the Carolina Bays        Time since Impact: 614 Seconds        10.2 Minutes        .1 Hours
```

The 3D program shows the debris impacting the planet

Secondary Craters from ejecta of a skip impact hitting Lake Michigan. The proposed event would be 5 pieces, with the secondary craters color coded to match the pieces.

Introduction: Last year we proposed that a skip impact by comet Swift Tuttle would be a better fit to explain the observed distribution of the fireballs associated with the Perseids Meteor Shower in August. The presentation was supported by our software [1] that showed the ejecta from such a skip impact would indeed match the observed pattern of fireballs [2] much better than the presently accepted theory of outgassing as the source. We continued developing the software. It was previously 2 dimensional and only showed the ejecta being sent into orbit around the sun. While the point at the time was to demonstrate that the ejecta would produce the observed pattern of fireball orbits observed for the Perseids Meteor Showers, such an event would have many other effects and it was desired to demonstrate more completely how the ejecta that falls back to Earth would appear.

We have enhanced the software to include full 3D presentations of the ejecta that falls back to Earth, including the effects from the Earth's rotation, atmospheric drag, and resultant secondary craters size, orientation and shape.

The Skip Impact Program: The program is written in QB64, which is a free, available online compiler. It runs about 100 times faster than other compliers on Windows, and is easy to modify. At present it requires being coded for each set of initial conditions, but as a programmer, it is fairly easy to make such adjustments. The code is available at craters.ca

Skip Impact secondary craters: Studies with iSALE impact hydrocode show that secondary craters from the ejecta of a large impact would produce elliptical craters for a wide range of impacts. Assuming Swift Tuttle hit Earth during the recent ice age, forming Lake Michigan, then the ejecta would have been largely blocks and debris made of ice. iSALE shows that ice impacting at low angles of 10 to 25 degrees, at speeds of 3 to 5 km/sec would form very shallow elliptical craters. If the impact was by several pieces, and occurred over a long path as the various pieces hit, then the axis of the ellipses would point back to the origin of the impact, but would present many angles due to the individual pieces being derived from different locations.

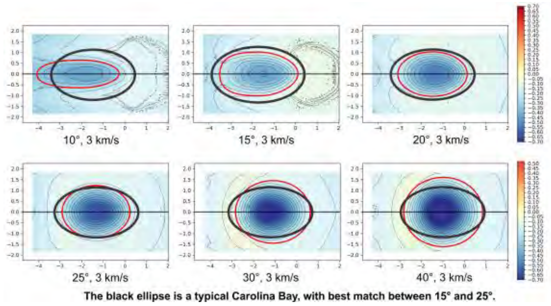

The black ellipse is a typical Carolina Bay, with best match between 15° and 25°.

iSALE calculated craters from ice blocks impacting sand.

The Skip Impact program starts with particles tossed by a low angle skip impact in the area of Lake Michigan, and then applies gravity, atmospheric drag, and the Earth's rotation to the particles. The particles initial velocities and sizes effect their paths and final destination. A very large portion of the particles that start with velocities less than escape velocity of 11 km/s end up hitting along the east coast of the US, landing in low angle, slow speed impacts, forming the same shape craters as predicted by iSALE. The secondary craters calculated by the program match the observed Carolina Bays very well.

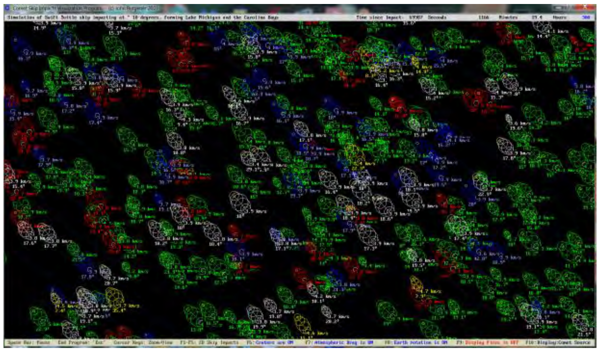

Skip Impact calculated craters from secondary impacts after a Lake Michigan skip impact. Note that the majority hit between 3 and 4 km/s, at angles between 15 and 25 degrees. The resultant pattern is the same as observed in the Carolina Bays.

Michael Davias has proposed that the Carolina Bays are secondary craters from a skip impact at Saginaw Bay, about 200 kilometers east of Lake Michigan. The Skip Impact program also shows that similar secondary craters that would be produced in such an impact. While the general result is very similar, there are less variations in the crater axis directions since this impact occurs over a much shorter path. The Lake Michigan proposal fits better.

Presentation of expected crater shapes: Typically impact studies focus on high angles. 90 degree impacts are the simplest to simulate in software, and since the cratering aspect of an impact is mainly due to the shock wave, craters are very similar to a 90 degree impact for any angle impact above 40 degrees. As the impact angle goes lower, the resulting craters become elliptical instead of circular, but elliptical craters are a small portion of the craters observed. However, impact craters of less than 20 degrees should be over 10 percent of all craters and are worth studying. The Skip Impact program has a simulation of thousands of comets impacting Earth on a grid pattern, showing the distribution of crater impact angles and shapes. The low angle impacts produce very unexpected crater shapes, suggesting that we do not see low angle impacts due to them being dramatically different shapes than expected. Lake Michigan, which is almost identical in shape to Mars' Orcus Platera, is similar in shape to low angle impacts calculated by the Skip Impact Program.

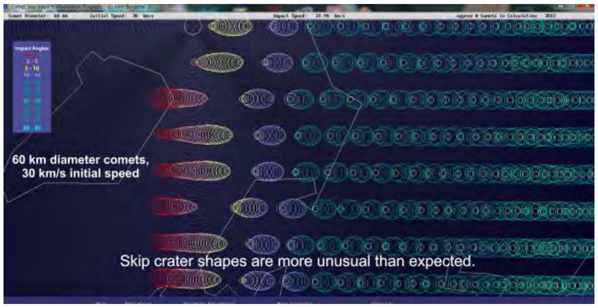

Skip Impact Program presentation of the range of craters possible from 0 to 90 degree impacts.

Conclusion: The SkipImpact 3D software indicates that a skip impact by Comet Swift Tuttle would fit as the source of the Carolina Bays as secondary impacts from the impact debris, and would explain the distribution of the fireball orbits associated with the Perseid Meteor Shower. The program predicts that very low angle craters will be of unusual shapes and often not recognized due to their elongated and shallow shapes.

Acknowledgments: We gratefully acknowledge the developers of iSALE-2D, including Gareth Collins, Kai Wünnemann, Dirk Elbeshausen, Tom Davison, Boris Ivanov and Jay Melosh, and we gratefully acknowledge the developers of iSALE-3D, including Dirk Elbeshausen, Kai Wünnemann, Gareth Collins and Tom Davison.

References:

[1] Burgener, J (2021) SkipImpact Program. Available to download and use freely from the web site: www.craters.ca

[2] Cooke, W. (2014-2021), NASA's All Sky Fireball Network daily charts of fireball orbits posted on www.spaceweather.com.
Included fireball chart from Aug 2015: https://www.spaceweather.com/FIREBALL_PARSER/fireball_data.png?PHPSESSID=ik2r3o2g28eob2n25cpmlc49o4

[3] Davias, M., Harris, T. (2019) "An Incomprehensible Cosmic Impact at the mid Pleistocene Transition, Searching for the Missing Crater using Australasian Tektite Suborbital Analysis and Carolina Bay's Major Axes Triangulation"; GSA Annual Meeting in Phoenix, Arizona, USA.
DOI: 10.1130/abs/2019AM-332326

DISTINGUISHING IMPACTOCLASTIC FROM PYROCLASTIC LAYERED ROCKS ON MARS.

D. M. Burt, ASU School of Earth and Space Exploration, Tempe, AZ 85287-6004, dmburt@asu.edu.

Introduction: Ancient layered rocks on Mars could well include both impactoclastic and pyroclastic (volcanic) density current deposits (IDC and PDC deposits respectively), based on the fact that ancient Mars (before about 3.5 Ga) [1] is believed to have had a relatively dense atmosphere and abundant volatiles, as well as widespread impact cratering and basaltic volcanism. Later, most of its atmosphere was gradually lost and both large-scale impact cratering and volcanism both tapered off, with volcanism probably tapering somewhat later.

Despite these considerations, the ancient cross-bedded, spherule-bearing clastic rocks on Mars studied by the initial three rovers at the two MER landing sites (Meridiani Planum and Gusev Crater) and later the concretion- and clay-bearing cross-bedded rocks at Gale Crater have mainly (with the exception of a pyroclastic interpretation for the beds at Home Plate in Gusev) been interpreted as deposited by flowing or standing liquid water or by wind [2]. From the beginning, my co-workers and I have alternatively interpreted these as being deposited by distal large-scale impactoclastic density currents [3,4].

In this regard, all of the rover landing sites to date occur near the Martian equator, which is the approximate boundary between the Martian highlands and lowlands. This boundary should have been the focus for density current flow generated by impacts or explosive volcanism anywhere in the highlands. The cold and thin late atmosphere of Mars helped preserve these old (Late Noachian to Early Hesperian) bedded rocks from erosion.

Confusing things, variable later diagenesis was caused both by neutral groundwater (in Gale Crater only, forming primitive clays and typical concretions [5]), and by surficial acid condensates (acid frost or mist, forming both acid and neutral sulfates near the surface [6]). Such weathering or diagenetic features can be confused with those caused during primary deposition. Similarly, sulfate-filled polygonal joints in Gale were confused wih sedimentary mud cracks [7] and erosion patterns, viewed from above, were mistaken for both festoon current bedding (Meridiani) and a volcanic bomb sag (Gusev).

The Problem: Given that both ancient impactoclastic or cratering (IDC) and pyroclastic or volcanic (PDC) deposits might well occur on Mars, how could they be distinguished from each other, given that both are deposited by dilute turbulent density currents caused by energetic blasts? The brief answer is probably not easily, even using observations by surface rovers, in addition to those from orbit. Sample return to Earth might be necesssary. This problem is summarized by Tables 1 and 2 below [8][9][10]. These tables must be regarded as prelimary and somewhat optimistic and conceptual rather than observational, especially given that recognized examples of impactoclastic rocks are rare to absent on Earth.

Discussion: Potential similarities (Table 1) include abundant low-angle cross bedding, presence of ballistic ejecta, low-density, friable nature, relatively poor sorting and rounding, except with distance, presence of dune forms and original dip draping topography, overriding small obstacles, large-scale control by topography (downhill flow), polygonal shrinkage cracks filled by veins (caliche on Earth, Ca-sulfates on Mars), presence of spheroidal accretionary lapilli, and being readily eroded, weathered, or diageneticaly altered. Potential differences (Table 2) might include relative age (Martian volcanics could be slightly younger), composition (basaltic suggests impactoclastic, especially for Mars, excepting small-scale maars), scale or extent (large scale again suggests impactoclastic), intensity of the explosition (larger for impacts), presence of high-pressure or high-temperature minerals, and abundance of melt spherules and related forms (higher for impacts).

Conclusions: Distinguishing impactoclastic from pyroclastic layered rocks, especially on Mars, is not a trivial task, especially from orbit. Spatial relations to impact as opposed to volcanic craters might be the best guide, as for rampart (layered ejecta) deposits on Mars, but mostly this is not available, owing to superposition and erosion.

Acknowledgments: For numerous observations and ideas, I remain grateful to former co-authors, mentors, and colleagues, including R.F. Dietz, M.F. Sheridan, K.H. Wohletz, and especially L.P. Knauth.

References: [1] Head, J.W. et al. (2020) *LPS LI,* Abstract #2967.[2] McLennan, S.M. et al. (2019) *AnnRevEarPlanetSci 47*, 91. [3] Knauth L.P. et al. (2005) *Nature, 438*, 1123. [4] Burt D.M. et al. (2008) *JVGR*, *177*, 755. [5] Sun, V.Z. et al. (2018) *Icarus 321*, 866. [6] Zolotov, M.Y. and Mironenko, M.V. (2007), *JGR 112*, E07006. [7] Stein N. et al., (2018) *Geology 46*, 515. [8] Wohletz (1998) *in* Freundt, A. and Rosi, A. *From Magma to Tephra*, Elsevier, Ch. 7, 247. [9] Branney, M.J. and Kokelaar, P. (2002) *GeolSocMemoir 27*. [10] Burt D.M. (2022) *in* Foulger, G.R. et al., eds., GSA Spec. Pap 553,Ch. 27, 347.

TABLE 1. COMMON FEATURES OF IMPACTOCLASTIC AND PYROCLASTIC DEPOSITS (Burt)

Features:	**Impactoclastic (IDC) Deposits**	**Pyroclastic (PDC) Deposits**
Bedding	Well-defined, if present; planar scouring leading to low-angle cross-bedding is typical. Beds can also be massive.	Well-defined, if present; planar scouring leading to low-angle cross-bedding is typical. Beds can also be massive near source.
Ballistic ejecta	Should be common at all scales, possibly leading to ballistic bomb sags in bedding.	Bomb deposits locally common around small-scale basaltic maar deposits, leading to distinctive bomb sags in bedding.
Low-density, friable deposits	Yes, very typical. Poorly cemented (on Mars, possibly mainly by water-soluble salts). Missing on Earth (eroded).	Yes, where not welded or deeply buried by lavas or sediments. Rapid weathering on Earth.
Sorting and rounding	Rather poor, relative to most water or wind deposits. Probably improves markedly with distance, however.	Rather poor, relative to most water or wind deposits. Improves markedly with distance, however.
Dune forms	Probably locally present, as are antidunes for especially sticky clasts.	Locally present, as are antidunes for especially sticky clasts.
Original dip; beds draping over topography	Should be common, especially for sticky particles. Beds can override obstacles.	Common; sticky particles s can even stick to trees and cliffs. Beds can override obstacles.
Control by topography	IDC's are deposited by turbulent density currents, flow downhill; could erode gullies and canyons.	PDC's are deposited by turbulent density currents, flow downhill; can erode gullies and small canyons.
Veining in shrinkage cracks and fractures.	Common; on Mars probably mainly Ca-sulfates in variable hydrations states. Polygonal cracks possible.	Common; on Mars probably mainly Ca-sulfates in variable hydrations states. Polygonal cracks common.
Diagenesis, including formation of concretions	Could be common if beds came in contact with groundwater; concretions irregula, unlike accretionary lapilli.	Could be common if beds came in contact with groundwater; iconcretions irregular, unlike accretionary lapilli.
Concentric color banding (accretionary lapilli)	Universal, if nature of turbulent cloud changed during growth	Universal if nature of turbulent cloud changed during growth

TABLE 2. IMPACTOCLASTIC (IDC) vs. PYROCLASTIC (PDC) DEPOSITS (Burt)

Deposit Features:	**Impactoclastic (IDC) Deposits**	**Pyroclastic (PDC) Deposits**
Relative Age:	Old; bombardment tapered off and atmosphere was lost. Some could be younger (LAERLE deposits)	Possibly somewhat younger; volcanism tapered off and atmosphere was lost
Composition:	Relatively unrestricted; related to composition of target. On Mars mafic to ultramafic.	Mostly silicic on Earth, except for small hydrovolcanic mafic maars
Scale/Extent	Unrestricted; related to energy of impact, planetary gravity, and atmospheric density	On Earth can be large if silicic; generally small if mafic (maars)
Intensity of explosion	High; very energy-intense	Moderate; steam explosions
Spherical accretionary lapilli (formed by sticky particles):	Yes; concentric spherules might contain high-temperature (specularite) or high-pressure (shocked) minerals	Yes; high T and P minerals unlikely in rapidly expanding and condensing steam
Glassy melt spherules and tectites	Yes; very common; smaller than accretionary lapilli; may be highly altered to clays	Yes; reported on Moon but rare. Pele's hair on Earth.
Geochemical anomalies (e.g., Ni, Ir, PGE)	Yes, but probably subtle, owing to dilution. Fumarolic and diagenetic alteration possible.	No? Fumarolic and diagenetic alteration possible.
Lateral facies changes	Yes, slow variations expected for large impacts, especially on low-gravity Mars	Yes, can be rapid for small volcanic exposions (maar-type), especially on Earth

EXPLORING POROSITY IN ASTEROID 16 PSYCHE WITH 3D HYDROCODE MODELING OF ITS DEEPEST IMPACT STRUCTURE.

W.K. Caldwell[1], A. Hunter[1], C.S. Plesko[1], [1]Los Alamos National Laboratory, Los Alamos, NM 87545, wkcaldwell@lanl.gov

Introduction: Asteroid 16 Psyche, the largest M-type (metallic) Main Belt Asteroid (MBA), is the subject of a forthcoming NASA discovery mission [1, 2]. In response to this mission, there have been recent efforts using experimental, observational, and modeling techniques to investigate Psyche. One of the fundamental remaining questions about Psyche is its composition. The degree of porosity and amount of non-metallic materials comprising Psyche is one of the most pressing questions regarding Psyche's composition [3].

This work seeks to further explore the effects of porosity on crater formation by simulating Psyche's deepest impact structure (i.e., a different impact structure than that modeled in our previous work) [4], located in its Southern hemisphere, with an estimated depth of 6.4 ± 0.64 km and an estimated diameter of 53 ± 15 km [5]. In particular, we consider varying amounts of uniform and layered microporosity, along with rubble-pile configurations, which include both macroporosity and microporosity. By varying the type of porosity, we test a number of potential compositions with bulk densities within the range of estimates obtained from other measuring techniques.

Methodology: For all simulations completed as part of this work, we used the ALE hydrocode FLAG, developed and maintained by Los Alamos National Laboratory [6, 7, 8, 9]. FLAG has been previously verified and validated for impact cratering problems [10, 11] and has been used for planetary science applications [4, 12]. FLAG is a multi-physics hydrocode with a variety of material modeling and equation of state (EOS) capabilities [6, 7, 8, 9]. FLAG can be used for 1D, 2D, and 3D simulations with Lagrangian, Eulerian, or ALE strategies, including adaptive mesh refinement (AMR) [6, 7, 8, 9, 13].

Because our simulations focused primarily on porosity rather than material, we chose to use the alloy Monel for both target and impactor in all simulations of our porosity study. Porous Monel was used in our prior study of Psyche and produced crater dimensions within the uncertainties of the measured dimensions [4]. Monel is a nickel alloy with a solid density of 8.81 g/cm^3 and is likely extraterrestrial in origin, which makes it a reasonable choice for modeling metallic asteroids [14, 15]. Monel also contains small amounts of non-metallic materials that are common in solid bodies in the solar system. Thus, we use Monel for both the target and impactor material, and vary the amount and type of porosity in Psyche to gain further insight into Psyche's probable porosity distribution.

For the EOS, we used an analytic Mie–Grüneisen EOS, which is an appropriate choice for these simulations because melt is not expected to play a significant role [16]. We used the Steinberg–Guinan constitutive model [17], and we set pressure and density thresholds to define damage. To model microporosity within Psyche, we used a P-α porosity model. The material surrounding Psyche, including the space between boulders in the rubble piles, was modeled as void. Figure 1 shows the simulation initializations for 3D simulations.

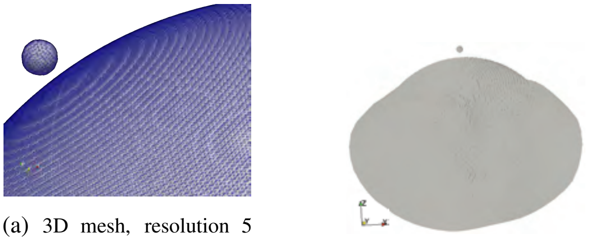

(a) 3D mesh, resolution 5 cells per projectile radius (cppr), corresponding to a zone size of 750 m, zoomed to show detail

(b) 3D Cartesian, uniform microporosity

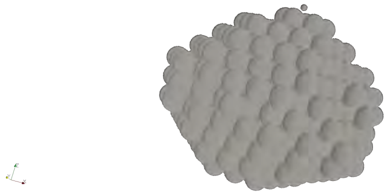

(c) 3D Cartesian, hexagonal close packing, rotated to show impactor height above surface. We again note that these spheres are boulders in a rubble-pile configuration and are not SPH particles.

Figure 1: 3D simulations at initialization, showing setups for uniform microporosity and rubble piles.

Simulation Results: Simulations modeling Psyche with uniform microporosity, with layered microporosity, and as a rubble-pile structure feature in this work. Simulations included both 2D and 3D models. Figure 2 shows each of these simulations plotted as depth vs. diameter as well as crater dimensions based on theory and radar data, shaded to include uncertainties. The best match to crater dimensions resulted from the simulation modeling Psyche as a rubble pile with a regular hexagonal close packing and a vertical impact angle.

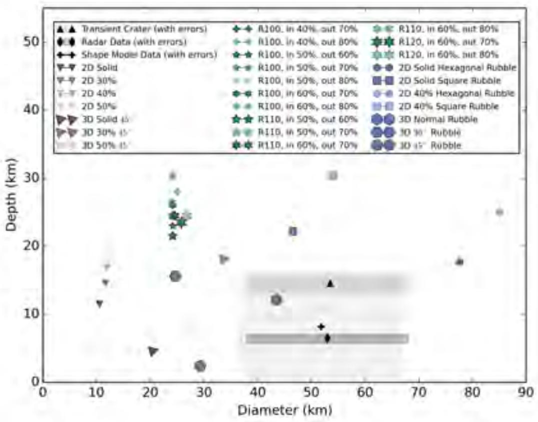

Figure 2: Crater aspect ratios of simulations from our porosity study using Monel as both target and impactor.

Conclusions: Our simulations indicate that Psyche is more likely to be a rubble pile of multiple solid boulders than a single body with either uniform or layered microporosity. Simulations modeling Psyche as a uniform rubble pile resulted in crater profiles with depth-to-diameter ratios more closely resembling Psyche's deepest impact crater than simulations with other porosity configurations. Furthermore, the 3D simulation with a regular hexagonal packing of solid boulders and a normal impact angle resulted in a crater with depth and diameter values within the uncertainties.

We cannot rule out microporosity with an oblique impact angle from our simulations alone, although such a composition is less likely to be found in a large asteroid such as Psyche. Our results demonstrate that bulk density alone is insufficient when modeling target asteroids in impact cratering simulations.

References

[1] D. F. Lupishko. On the Bulk Density of the M-type Asteroid 16 Psyche. *Solar System Research*, 40(3):214–218, 2006.

[2] David Y. Oh et al. Psyche: Journey to a Metal World. In *52nd AIAA/SAE/ASEE Joint Propulsion Conference*, page 4541, 2016.

[3] LT Elkins-Tanton et al. Observations, meteorites, and models: A preflight assessment of the composition and formation of (16) psyche. *Journal of Geophysical Research: Planets*, 125(3):e2019JE006296, 2020.

[4] Wendy K Caldwell et al. Understanding Asteroid 16 Psyche's composition through 3D impact crater modeling. *Icarus*, 351:113962, 2020.

[5] Michael K. Shepard et al. Radar observations and shape model of asteroid 16 Psyche. *Icarus*, 281:388–403, 2017.

[6] James L. Hill. *User's Manual for FLAG version 3.6.0*. The Lagrangian Applications Project, Los Alamos National Laboratory, January 2017. LA-CP-17-20057.

[7] D. Burton. Connectivity structures and differencing techniques for staggered-grid free-lagrange hydroynamics. Technical Report UCRL-JC-110555, Lawrence Livermore National Laboratory, Livermore, CA, 1992.

[8] D. Burton. Multidimensional discretization of conservation laws for unstructured polyhedral grids. Technical Report UCRL-JC-118306, Lawrence Livermore National Laboratory, Livermore, CA, 1994.

[9] D. Burton. Consistent finite-volume discretization of hydrodynamic conservation laws for unstructured grids. Technical Report UCRL-JC-118788, Lawrence Livermore National Laboratory, Livermore, CA, 1994.

[10] Wendy K. Caldwell et al. Verification and Validation of the FLAG Hydrocode for Impact Cratering Simulations. *Journal of Verification, Validation and Uncertainty Quantification*, 3(3):031004, 2018.

[11] W. K. Caldwell et al. Benchmarking numerical methods for impact and cratering applications. *Applied Sciences*, 11(6):2504, 2021.

[12] CS Plesko et al. Impact hazard mitigation of a highly porous contact binary asteroid. *Phys Rev E*, 90:033107, 2019.

[13] M.A. Kenamond. (U) AMR in FLAG. Technical Report LA-UR-20-27533, Los Alamos National Laboratory, Los Alamos, N.M., 2020.

[14] Lewis E. Shoemaker and Gaylord D. Smith. A Century of Monel Metal: 1906–2006. *JOM*, 58(9):22–26, 2006.

[15] Ulrich Riller. Structural characteristics of the Sudbury impact structure, Canada: Impact-induced versus orogenic deformation – A review. *Meteoritics & Planetary Science*, 40(11):1723–1740, 2005.

[16] H. Jay Melosh. *Planetary Surface Processes*, volume 13. Cambridge University Press, 2011.

[17] D. J. Steinberg et al. A constitutive model for metals applicable at high-strain rate. *Journal of Applied Physics*, 51(3):1498–1504, 1980.

Acknowledgments The authors wish to acknowledge Scott Doebling and C.J. Solomon for their assistance in data transfer. This work was supported in part by a completion fellowship from the Arizona State University Graduate College, a grant from the Center for Space and Earth Science for Research and Development in Space Science, the Advanced Simulation and Computing (ASC)–Integrated Codes program at Los Alamos National Laboratory (LANL), and the ASC–Threat Reduction program at LANL. Los Alamos National Laboratory, and affirmative action/equal opportunity employer, is operated by Triad National Security, LLC, for the National Nuclear Security Administration of the U.S. Department of Energy under contract 89233218NCA000001.

LA-UR-22-26193

THE MARE PROTOLITH THICKNESS AND COMPETENCE: A CONTROL OF ROCKY CRATER POPULATIONS.

M. A. Chertok[1], P. G. Lucey[1], E. S. Costello[1], and S. M. Ireland[2], [1]University of Hawai'i at Mānoa mchertok@hawaii.edu, [2]Miami University.

Introduction: The Moon's surface is covered by a regolith that develops as meteorites bombard the lunar surface, forming a poorly sorted layer of fragmental debris. New rocks are excavated and thrown onto the surface when an impactor of a large enough size and high enough velocity penetrates the regolith, reaching the underlying competent material. As the regolith deepens, the smaller impacts are confined within the regolith, leaving only larger impactors able to excavate rocks [1]. Remote sensing studies of the local variations in the abundance of rocks on the lunar surface can illuminate our understanding of the thickness of the regolith [e.g., 2].

Older surfaces are expected to have thicker regolith; therefore, there would be fewer rocks exposed. We tested this notion by measuring the abundance of rocks as a function of mare unit age and found that the distribution of ejecta rocks shows that there is a poor correlation between age and rock abundance [3]. While differences in age do not explain variations in rocky crater populations, the nature of the mare protolith may be an alternate important control on rock abundance. Head and Wilson [4] propose diversity among mare protoliths where differing structural characteristics were developed upon emplacement. Such variations in the competence of the lava flows have effects on the ability of an impactor to break up and excavate blocks of rock.

The maria offers a uniquely wide range of well-dated volcanic deposits. Hiesinger et al. [5, 6, 7] constrained the ages of mare units using crater counting techniques and found ages ranging from 1.2-4.2 Gyr [8]. We report on each dated surface's productivity in exposing rocks as a function of impactor size using crater size-frequency distributions (SFDs). Additionally, we investigate variations across the anomalously rocky Mare Humorum by inspecting crater SFDs for units associated with a resurfacing event that fully flooded some units, but not others [9]. By focusing on this region in our study, we can isolate the effects of the competence of the original Humorum flows, the competence of the resurfacing flow, and their combined thickness on the SFD.

Site Selection: This study features rocky crater counts of 18 lunar mare sites. These sites overlap with Hiesinger et al. counted areas [5, 6, 7] but are larger to collect adequate statistics on rocky craters that are less abundant than the total population. Counted areas range in size from 3,200 - 3,700 km^2 (Humorum sites are smaller due to smaller unit sizes). Sites include seven locations within Oceanus Procellarum, two in Mare Imbrium, two in Mare Nubium, one in Mare Serenitatis, four in Mare Humorum, and two in Mare Tranquillitatis.

Data: We use shaded relief imagery generated from the merged LOLA/Terrain camera DEM data set for the crater counting [10] and rock abundance or "rockiness" is quantified using thermal inertia data from LRO Diviner following Bandfield et al., 2011. During the lunar night, boulders retain their heat more efficiently than the insulating regolith, which makes rocks detectable as temperature anomalies [11]. From the rock abundance parameter, we can then determine how crater SFDs vary with the degree of rockiness.

Methods: The CraterTools plug-in for ArcMap [12] was used to count craters, all of which are greater than 200 m in diameter to ensure penetration to bedrock. Secondary impact craters were included in the crater counts to capture the entirety of the crater population. CraterPy [13] was used to extract rock abundance statistics from the crater ejecta, which is defined to extend from 1.1 to 2 crater radii. The average rock abundance of the ejecta was used to develop rock abundance binning for the crater size-frequency distributions. The bins are defined by 1% increments of rock abundance. A crater is added to every bin where its ejecta rock abundance is greater than or equal to that bin limit.

Results: Mare Humorum has the most rocky craters per area of any study site, despite being relatively old. A single unit in Humorum has more than 100 craters that contain a mean of 3% coverage of rocks, greater than any other unit of similar size.

We computed size-frequency distributions for each site's total population and the various degrees of rock abundance. A central unit in Humorum, for example, encompasses a wide range of ejecta rock abundance. Figure 2 shows the various phases of the relationship between crater size and rock abundance. Larger craters are generally more rocky than smaller craters at this site, which results in a "pinching" appearance of the SFD. Essentially, the converging behavior indicates that at a certain diameter and above all craters have high rock concentrations and only small craters lack rocks. As the rock abundance cutoff is increased, craters of all sizes begin to be excluded.

The crater size-frequency distribution for Mare Imbrium (Figure 2) features the parallel behavior throughout all levels of rock abundance. There is a wide gap between the size-frequency distributions at each step. The rockiest craters at this site are a size-representative subset of the total crater population, where rocky craters share the same distribution of sizes but at lower abundances.

All counted sites exhibit variable behavior in their SFDs. Some sites show strong departures from the slope of the total population as rock abundance cutoffs are increased, and others show the parallel slope behavior with increasing rock abundance.

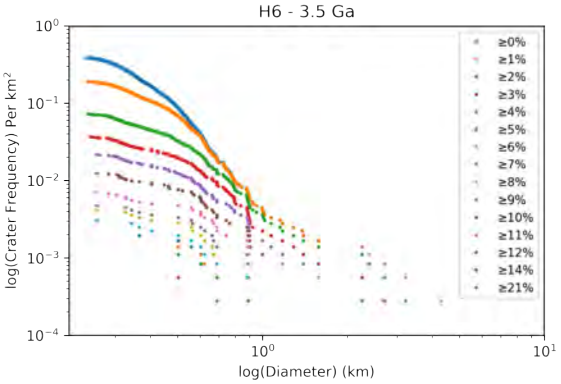

Figure 1: Size-frequency distribution of craters at Mare Humorum increasing in rockiness.

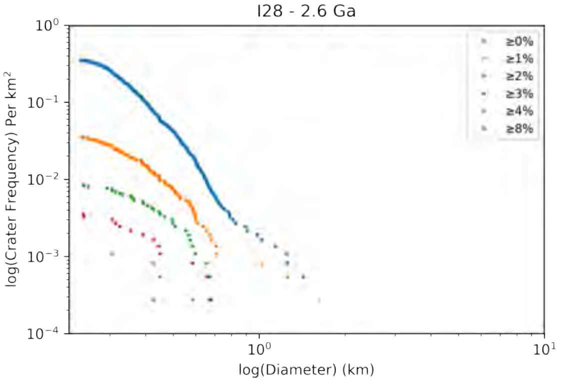

Figure 2: Size-frequency distribution of craters at Mare Imbrium increasing in rockiness.

Upon closer inspection of Humorum basin, the SFDs of two central sites overlying 500-1000 m thick lava flows [14] show the converging behavior, whereas the SFDs of the two marginal sites (0-500 m thick flows [14]) show the parallel behavior, consistent with Figure 2.

Discussion: Mechanical properties such as vesicularity, crystallinity, and density, among others, may influence an impactor's ability to break up and eject rock beneath the regolith [4]. These protolith features may be responsible for the anomalously rocky surface of Humorum, such that a thick, competent lava flow could provide an ample supply of rocks. Rock-poor surfaces may indicate that the lava flows were thin or friable such that destruction of rock is possible. Variations across Humorum show that there may be a correlation between the converging SFD and thick lava flow deposits. Large impactors can sample a vast supply of competent rock. Conversely, the parallel SFD sites in Humorum are on the margins of the basin where flows are thinner. The regolith itself may have local variability in thickness causing smaller impactors to exhume powdery mare regolith rather than the competent basalts buried deep.

The varying degrees in pinching of the size-frequency distributions (Figures 1 and 2) may illuminate local variations in regolith thickness. These distributions are uniquely sensitive to rockiness as a function of size, so for variable regolith thicknesses, we would indiscriminately lose craters of all sizes with increasing rock abundance. The more irregular the contact between regolith and underlying mare basalts, the more small craters will have the ability to excavate rock. This behavior is shown in the more parallel size-frequency distributions (Figure 2). In the case of the converging size-frequency distributions (Figure 1), the slope shallows with increasing rock abundance. Thus, the pinching behavior is indicative of a loss of small craters. As the pinching behavior starts to exhibit more parallel characteristics, the size-representative population of rocky craters indicates that the regolith is somewhat irregularly thick. In summary, the parallel behavior is indicative of a highly irregular regolith thickness compared to size-frequency distributions featuring a pinching behavior.

Conclusions: We have determined that rocks on the lunar surface may be dependent on the nature of the regolith and underlying mare basalts. To probe the thickness of the regolith and the competence of mare basalts, we can examine the behavior of crater size-frequency distributions. Therefore, crater distributions and rock abundance values can be used to explore the complexities of the lunar subsurface.

References: [1] McKay et al. (1991). *In Lunar Source-Boo*k, pp. 285–356., [2] Elder et al. (2019). *JGR: Planets*, 124(12), 3373-3384. [3] Chertok et al. (2022) *LPSC 53.* #1031., [4] Head & Wilson (2020), Geophys. Res. Letters, 47(20)., [5] Hiesinger et al. (2000). *JGR*. 105, 29239–29275., [6] Hiesinger et al. (2003). *JGR*. 108, 5065., [7] Hiesinger et al. (2010) *JGR: Planets*. 115(E3)., [8] Papike, J. et al. (1998) *Reviews in Min. and Geochem., 36*, 5.1-5.234., [9] Head (1974). *5th Lunar Conf., V1,* pp. 207-222., [10] Barker et al. (2016), *Icarus*, 273, 46-355., [11] Bandfield et al. (2011), *JGR*, 116(E12)., [12] Kneissl et al. (2011). *Planetary and Space Sci*. 59, 1243–1254. [13] Tai Udovicic, C. J. (2021) *Craterpy*. [14] Budney & Lucey (1998). *JGR: Planets,* 103(E7), 16855-16870.

USING SECONDARY CRATERS TO ASSESS STRENGTH DIFFERENCES BETWEEN NEIGHBORING SURFACE UNITS.

J. W. Conrad[1] and C. I. Fassett[1], [1]NASA Marshall Space Flight Center, Huntsville, AL 35805. (jack.w.conrad@nasa.gov)

Introduction: An issue with Martian remote sensing studies is the difficulty inferring surface and crustal material properties. For direct information we rely on the instruments of landed missions, like *InSight*, and extrapolate to other locations. To apply this, we would like to use a methodology that can benefit from remote sensing data. We are exploring using secondary craters, which are often thought of as nuisances when determining accurate ages, to calculate crustal properties. The upside of secondary craters is that they are from ejecta blocks that move at relatively lower speeds. This lets them reside in a different crater scaling regime [1], one that is more sensitive to the crust's effective strength (Y_{eff}) and porosity/internal friction (through the μ and K_D terms [2]).

Crater Scaling and Methodology: There are multiple parameters that influence the size of secondary craters, but we can measure craters in ways that isolate the dependence of crater size to just Y_{eff}. We focus on secondary clusters and rays that have impacted into distinct but bordering geological units. Separate clusters/rays that are equidistant, but in bordering units are also considered. These secondaries can be used to determine Y_{eff} thanks to one important factor: all the secondaries in this cluster are from the same distant primary, and as a result, the ejecta velocity, median block sizes, and densities are expected to be the same (at least to first order). Thus, variations between secondary crater sizes in the two units are due to material property differences like Y_{eff}. Thanks to the steep size frequency distributions (SFD) of secondaries [3], observable secondary crater sizes are tightly clustered, and we can simply use differences in median secondary sizes between two geologic units to constrain the ratio of Y_{eff}. We are also able to use the SFD to check if our counted craters are secondaries and if the two crater counting areas are from the same source and thus have the same power law slope.

Our methodology needs to take care to identify secondaries near the contact region of two geologic units. Primaries are typically easy to pick out based on degradation state or morphology. Additionally, where secondaries are clustered, they tend to be numerically dominant. For surveying sites of interest, we aim towards younger/larger primary craters, as those tend to have fresher/larger secondaries. Once we identify a primary that fits, we note the geologic boundaries surrounding it and if others have mapped out secondary fields in those areas. We then determine two counting areas at approximately same distance from the primary, one in each unit. Following that, we identify and count secondaries in each area, and analyze those results.

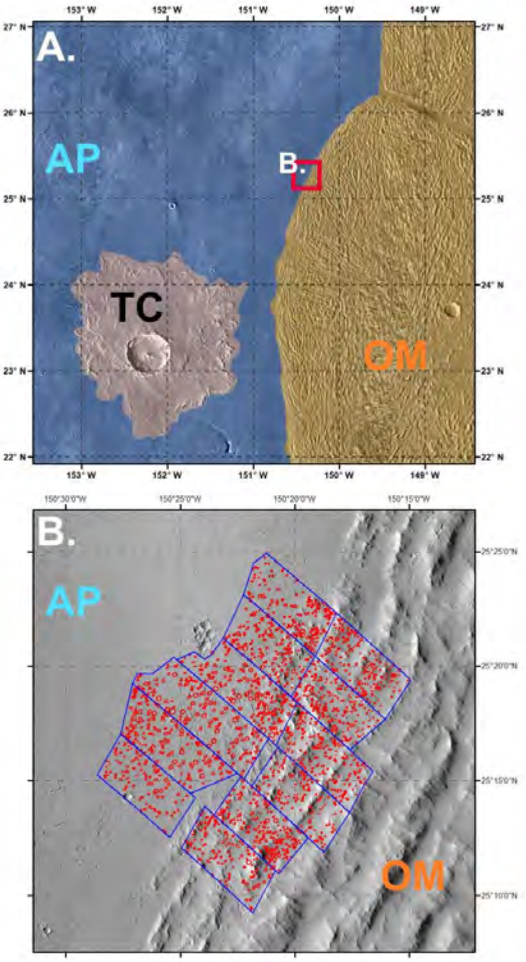

Figure 1: A. Map of TC study area, which includes the bordering units of Amazonis Planitia (AP; blue) and the Olympus Mon Aureole (OM; orange). Red square: The location of the bottom panel. B. Secondary crater counts for the two units. Divided up to test range effects, which are minimal.

Example Results: For our first attempt, we applied this technique on the secondary crater fields of Tooting Crater, Mars (TC; [4]). TC is a young complex crater that is situated in the Amazonis Planitia (AP) region, and the surrounding area can be observed in Fig. 1A. TC has many fresh secondary craters that are relatively easy to count. In the northeast section of TC's secondary field (found at -150.35° lon, 25.25° lat), there is a geologic unit boundary between AP and the Olympus Mons

Aureole (OM) that contains many secondaries from the same cluster across the boundary.

AP is a volcanic plain, like Elysium Planitia, which lies in the northern lowlands. OM, however, is a unit made from successive landslides off Olympus Mons that might be expected to be relatively weak compared to the AP volcanic plains. In addition, a recent observation of increased buried water ice in the unit [5], especially compared to AP, might drive the Y_{eff} value lower and the secondary sizes further from each other.

What we find when we count the secondaries in that cluster (Fig. 1), however, is that the median diameter of secondaries in AP is 96.5 m, much larger than those in OM, at 58.8 m. We can use [1] to translate from these median diameters to a Y_{eff} ratio of OM to AP if we set μ to be constant (~0.5). For secondary debris sizes around a tenth the mean crater size, we get a Y_{eff} ratio OM:AP of ~8.5. This implies that the crust of OM is considerably stronger than AP, which is the opposite of what we hypothesized based on the geology. This tells us that either our picture of the geology here is incomplete, or that another target property like porosity may play a bigger role in crater scaling.

As a second pass at this analysis technique, we looked at the region around Mojave crater (MC). MC is another young complex crater with an abundance of secondaries that can be easily sourced from it. The primary geologic units surrounding MC are Noachian highlands (e.g., mNH) and Hesperian transition (e.g., Ht). These respectively represent old, relatively unmodified, and younger, water modified units.

We found two study areas with equidistant clusters of MC secondaries in the two units. While not the same cluster bisected by the border as in the TC study, they do conform to the same SFC slope. The characteristic crater diameters in our counts are 275 m and 170 m for Ht, and 200 m and 110 m for mNH for the northern (Fig. 2B) and southern (Fig. 2C) aeras respectively. These values give us a Y_{eff} ratio mNH:Ht of ~4.9 and ~6.7 for the two areas. The variance is likely a product of the 30 km difference from MC and the inconsistency in using this technique on two slightly separated secondary clusters. The observed difference is relatively robust, however, and the calculated ratio implies that the Ht terrain is weaker than mNH (or less porous). Since the difference in strength is again opposite to intuition, it may suggest that porosity variations are playing a key role in producing the observed differences.

Future Work: We plan on exploring how differences in porosity could explain the signal we observe in the secondaries of TC and MC. We also are attempting to expand to the Moon and Mercury.

Acknowledgments: J.W.C. is supported by an appointment to the NASA Postdoctoral Program at Marshall Space Flight Center. This work was also done with support from the Solar System Workings program.

References: [1] Holsapple, K.A. and Schmidt, R.M. (1987) *JGR: Solid Earth, 92(B7),* 6350–6376. [2] Prieur, N. C. et al. (2017) *JGR: Planets*. 122, 1704-1725. [3] McEwen, A.S. and Bierhaus, E.B. (2006) *Annl. Rev. EPS.* 34:535-567. [4] Mouginis-Mark, P.J. and Boyce, J.M. (2012) *Chemrie der Erde 72*: 1-23. [5] Wilson, J.T. et al. (2018) *Icarus,* 299, pp.148-160.

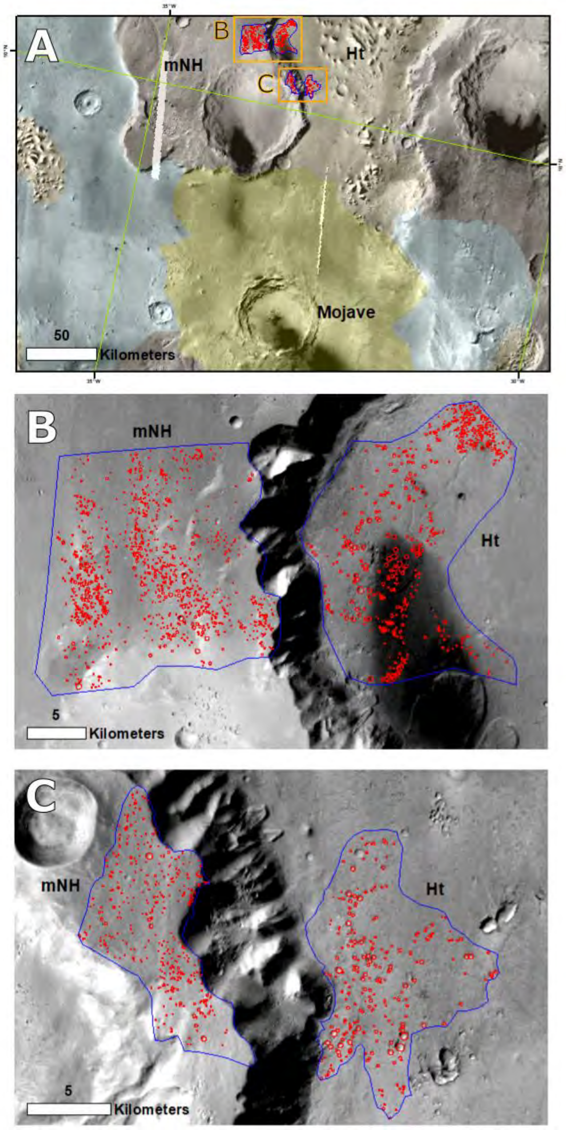

Figure 2: A. Map of the region surrounding Mojave Crater, Mars. Orange squares are the locations of the bottom panels. B. North location of interest. Multiple clusters and rays of secondaries are found equidistant from Mojave at 200 km. Left: mNH and Right: Ht. C. Same, but at 170 km. Craters are generally larger in the Ht terrain. Signal of differences in strength or lower porosity?

LARGE IMPACTS ON ICY BODIES AS A FEASIBLE MECHANISM FOR INDUCING HABITABILITY: THE CASE OF MENRVA CRATER ON TITAN.

A. P. Crósta[1]; E. A. Silber[2], R. M. C. Lopes[3], M. J. Malaska[3], [1]Geosciences Institute, State University of Campinas, P.O. Box 6152, 13083-970, Campinas, SP, Brazil crosta@unicamp.br; [2]Western University, London, ON, Canada; [3]Jet Propulsion Laboratory, California Institute of Technology, Pasadena, CA, USA.

Introduction: Titan is a unique potentially habitable world: it is, at the same time, an ocean world, an icy world, an organic world, and has a dense atmosphere. Although Titan's low surface temperatures are not conducive to life, the liquid ocean underneath the ice shell is warm enough at ~260K to be potentially suitable for life. Titan´s surface, in turn, is coated by a complex mixture of organic molecules, and has plenty of liquid methane in the form of rivers, lakes and seas. Thus, pre-biotic and biotic life forms may have developed in its water ocean underneath the ice shell, provided pathways connecting surface materials and subsurface water ocean existed. For these pathways to exist, its relatively thick ice shell (between 80 and 100 km thick) would have to be broken or penetrated. Large hypervelocity impacts are among the likely mechanisms capable of inducing the connection between the atmosphere/surface layer and the underground liquid ocean.

The effects and consequences of large cosmic impacts on rocky planetary bodies is nowadays reasonably well constrained and understood. The same cannot be said about impacts on icy bodies, of which little is still known. The knowledge is even more limited on planetary bodies with ice shells formed by mixtures of ice and methane clathrates with an underlying liquid ocean, as in the case of Titan [1-3].

We examine the role of large impacts on Titan in creating such conditions, as hypervelocity collisions of large bodies may have allowed exchange of materials (organic compounds, water, etc.) between the surface, the near subsurface and the ocean, creating niches for the development of primitive lifeforms. To investigate impact-induced potential exchange pathways we modeled the formation of the largest crater on Titan, Menrva, with a diameter of ca. 425 km, using numerical simulations performed in iSALE-2D shock physics code.

The formation of Menrva crater represents a geological event of significant consequences to the evolution of Titan´s ice crust. Very large craters such as this are prone to have formed earlier in the geological history of the solar system. However, the degree of preservation of Menrva's main morpho-structural features, suggests a younger formation age, probably in the last billion years [4].

We report on simulations of the Menrva impact event and its physical constraints. Through numerical modeling, we establish constraints for temperature, pression, extents of melt formation in both, lateral and vertical directions, and potential materials exchange among Titan's layers. Among other implications, we examine the role of such massive impact event in promoting habitable environments on Titan.

Modeling the formation of Menrva crater: The reasoning behind our models is that, given a large enough asteroid impact, the ice shell that forms the external layer of Titan's structure would be breached, either entirely or partly, creating pathways connecting the organic-rich mantle that covers its surface, to the sub-surface water ocean.

In the event of an ice shell breach, materials from the deep subsurface ocean, including salts and potential biosignatures of putative subsurface biota, could be emplaced on the surface — likewise, atmospherically-derived organics could be directly injected into the subsurface ocean, where they could undergo aqueous hydrolysis and form potential astrobiological building blocks.

To study the formation of a Menrva-like impact crater, we performed numerical simulations using the iSALE-2D shock physics code. We simulated different scenarios using current estimates of Titan's ice shell's thickness, constrained by the minimum and maximum values of 50 and 125 km, based on geophysical data [5], [6]. We also use different thicknesses for the conductive ice lid (22 and 60 km), and temperatures for the convective ice layer (245 and 255 K). A combination of these parameters, plus impactor sizes (28 and 34 km diameter) and the vertical component of the impact velocity (10 and 7 km/s, respectively), resulted in 28 different scenarios tested, all producing a ca. 425 km diameter crater.

Modeling results: In most of the scenarios, there was a complete breach of the ice shell at ca. 6000 s, except for the cases of a thicker shell and conductive ice lid (i.e., 125 and 60 km thick, respectively). In some, the penetration happened as melt-through into the ice shell.

Regarding the analysis of provenance depths, near surface materials are clearly mixed to great depths and vice versa. A considerable volume of ocean water is deposited within the crater, particularly in the center of the newly formed crater. Likewise, the surficial layer of organics, mostly methane, gets mixed with ice, undergoing complete or partial melt in the central region.

We also used tracers for the trajectories of parcels of the surficial organic layer, ice shell and water ocean (Fig. 1). The results show that melt materials, including organics and water, reach ca. 100 km into the ocean underneath the center of the crater, whereas a mix of complete and partial melt reach 65 km depth and 60 km away from the center. There is also a organics/ice mixing at ca. 10 km depth and >200 km from the center, where the partly melted ice shell with a thin layer of melt materials overturns and bury the organic-rich layer, being covered by a ca. 5 km thick ejecta material.

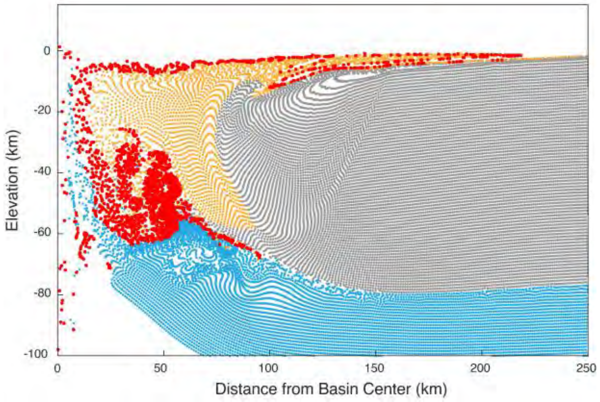

Fig. 1. Material mixing at t=5000 s based on peak shock pressures. Tracers depict the trajectories of parcels of the surficial organic layer, ice shell and water ocean. Red indicates complete melt, yellow partial melt, grey is the ice shell (peak pressure required for incipient melt) and blue represents the water ocean.

Our modelling indicates that material mixing may take place on the surface and in the deep-water ocean (Fig. 2), implying that both are suitable for putative biosignatures, either emplaced directly from subsurface mixing, or resulting from a transient surface habitat created by the impact. Similar results may be expected for craters with diameters in the range 70 to 120 km. In conclusion, large impact craters are preferred sites for future investigations of habitable environments on Titan.

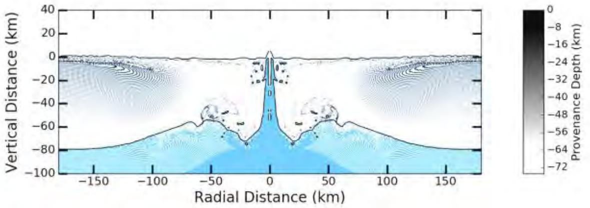

Fig. 2. Vertical mixing and material exchange between the surface and the ocean at t=5950 s. Tracers within the ice shell are colored according to their original depth.

Conclusions: Large hypervelocity impacts can have a key role in creating habitable environments or niches on Titan. A combination of these processes, in an environment containing organic compounds and water, heated to ca. 280 K by the transfer of thermal energy from the impact to the crust, can produce in a near-optimal habitable ecosystem or a habitable zone on Titan. Menrva crater and its immediate surroundings offer a potentially favorable location for future exploratory missions in search for putative biosignatures.

Acknowledgments: This research is part of the JPL-led NASA Astrobiology Institute team 'Habitability of Hydrocarbon Worlds: Titan and Beyond', partly carried out at the Jet Propulsion Laboratory, California Institute of Technology, under contract with NASA. A.P. Crósta acknowledges the financial support from the São Paulo Research Foundation (FAPESP) and the State University of Campinas, Brazil.

References: [1] Crósta A. P. et al. (2021) *Icarus*, 370, 114679. [2] Wakita S. et al. (2022) PSJ, 3, 50. [3] Carnahan E. et al. (2022) *GRL,* 49, e2021GL097602. [4] Hedgepeth et al. 2020 Icarus, 344. [5] Sotin et al. 2010. In: Brown, R.H.; Lebreton, J-P, Waite, J.H., 61-73. Springer. [6] Vance et al. 2018 JGR: Planets, 123, 180–205.

REGIME TRACKING AND BENCHMARKS FOR THE IMPACT MODELING COMMUNITY

M. L. Harwell[1,2]. S. T. Stewart [1], R. I. Citron [1,3,4], W. K. Caldwell [2], and C S. Plesko [2], [1]Department of Earth and Planetary Sciences, University of California, Davis, CA 95616 [2] Los Alamos National Laboratory, Los Alamos, NM, 847544 [3] Massachussets Institute of Technology, Cambridge, MA [4] NASA Goddard (megharwell@ucdavis.edu)

Introduction: The state of the art in impact cratering simulations typically implements multiple physical processes and regimes that are encountered at different times and locations during a cratering event. As the capability of computer models has surpassed the regime of physically feasible, large scale experiments, ensuring the accuracy of the models is important in studying the whole cratering process. While shock-physics codes are vital to understanding the cratering process, capturing the interplay of physics implemented and how they interact has not been well studied.

In addition, the rheology models implemented in impact codes differs across the field. While some models, including parameterized damage strength models (e.g., iSALE [1]) and acoustic fluidization [2], are common, they are not universal. Even when initial conditions are matched and as similar constitutive models as possible are used, details finer than depth to diameter ratios may not agree (e.g., [3, 4, 5, 6]). In the context of impact events, these differences affect observable crater features including the generation and transport of melt, fracture density, and the height of central peaks and peak rings.

At present, we have few standard metrics for investigating the mechanisms that are dominant at each stage of crater formation and comparing them between studies. Studying the interactions between multiple nonlinear processes in impact simulations can be difficult to understand and validate. Differences in the activation of these processes, where each dominates, and for how long affects the observable features in ways that can be used to test and improve the physical models. Understanding these effects is important for discriminating between physical models that result in comparable final crater morphologies but generate different stresses, peak pressures, melt, and bulk debris flows over time. While bulk features, such as final diameter and depth-to-diameter ratio, provide a means of comparison between codes and crater observations, they are not sufficient to understand the physical response of materials in the intermediate stages of crater formation.

Here, we present preliminary work on developing a new conceptual approach for probing the physical processes that are active throughout impact crater simulations. As the dominant physical processes and regimes evolve, we track when each process is activated to gain a 4D view of the event: a history that is resolved in both space and time. This 4D view of cratering will be used to inform future model development, laboratory-based tests, and comparisons to field observations. Not only does a 4D understanding of impact cratering process enable more robust studies of individual impact craters and crater populations, but it also allows for more directed validation efforts. For example, a 4D view can be used to identify aspects of a constitutive model that drive the behavior of a specific parcel of material as it undergoes deformation during the impact event. Then, the specific regimes that are dominant could be isolated for validation through laboratory experiments and for cross code consistency, as done in the MEMIN project [7]. Studies at this level of detail could be structured to address open questions in planetary science ranging from how much ground ice is melted during impact bombardment on Mars [8, 9] to the spatial distribution of projectile iron following late accretion impacts [10].

Methods In our approach, we implement material variables to track the activation of each implemented physical regime throughout an impact cratering simulation. We want to systematically record which physics packages are called while the target material experiences compression and deformation under the effects of varied initial conditions.

Though challenging to visualize and analyze, animations of the time evolution of regime activation and physical properties such as yield strength or fiction coefficient provide modelers with additional intuition of cratering mechanics and spatial maps of dominant processes. The time history of deformation for Lagrangian tracer particles or SPH particles provide alternate views of the history of materials that begin and end in specific locations of interest. These types of data can be compared between codes and for extraction and comparison to experimental studies and field observations.

The sampling of physical regimes by material parcels has been tested in both a simple impact simulation and simple tests at their extremes. The simple tests are designed to isolate different processes within the rheology model. While these results are preliminary, they provide a basis of discussing the evolution of rheology regimes acting on parcels of material under impact conditions.

A 4D look at cratering We are developing the ability to track regime changes in cratering simulations to watch the evolution of the dominant rheologic mechanisms throughout an impact event. Through tracers, we can watch how a single parcel of material experiences cratering, zooming in on the conditions experienced at specific locations in the target through the impact. This history provides insight into which regimes dominate in simulations and where to focus future development and validation efforts.

A Simple 1D problems We demonstrate the capability of regime tracking in a simple, 1D slab impact. A basalt slab of 10 cm thickness is impacted into a 1 m basalt slab at 7 km/s, driving a shock into the basalt target. Through varying the initial conditions of the run (lithostatic pressure, temperature, impact velocity), we are able to activate different failure mechanisms and test the constitutive regimes encountered by the material.

In the case shown, the intact material fails under a Collins failure envelope at the shock front [1, 11].

We plan to develop a suite of benchmark tests to activate different rheological regimes that can be used by the community in the developing and testing of various codes.

Conclusion Impact models must be capable of handling a broad range of rheological regimes. The cumulative effects of traversing through these various physical processes determines the simulated outcome of observable features.

In building simple tests and methods of visualizing the evolution of rheology dominant throughout the cratering process, we intend to provide impact modelers with a means of building intuition about impact events as well as provide a basis for verification of physics packages within their codes, validation of their codes, and comparison between available models.

Ideally, this framework to improving the sensitivity of models through constraining mid-stage crater formation will lead to models with enough fidelity to match observed features of specific craters. Through comparison with specific basins, we can use observables to constrain the intermediate steps of crater formation. This provides us with a way to check and correct the behavior of models. Potentially, models can improve enough to become predictive tools sensitive to showing properties specific to individual craters, including crater melt volume produced and the flow of that melt.

Acknowledgements: This work is supported by Simons Foundation Grant #554203 and NASA Grant 80NSSC18K0828. LA-UR-22-26192

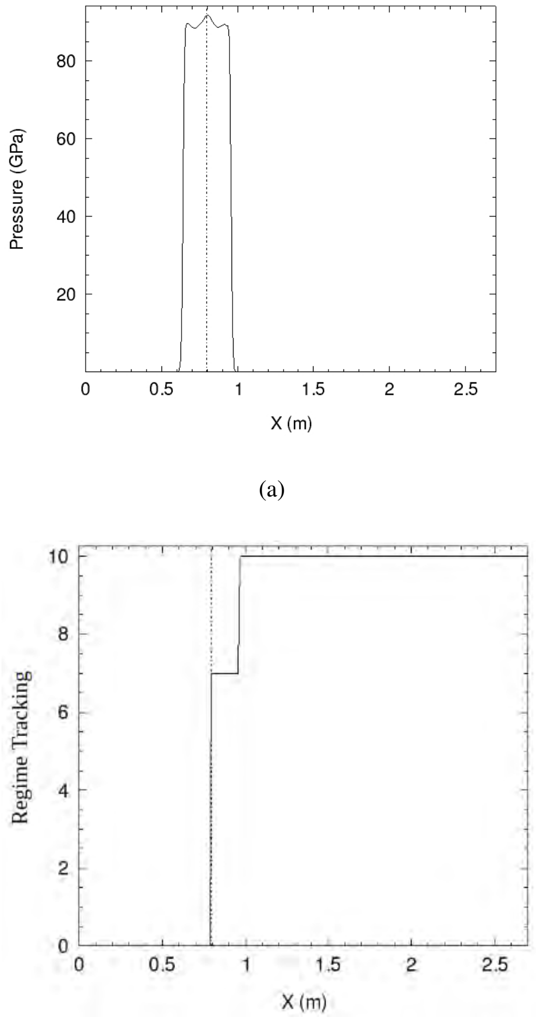

(a)

(b)

Figure 1: Pressure vs position (a) and regime tracking vs position (b) as slab impacts target at 27.1 μs. 10 denotes the unshocked material, and 7 corresponds to failure under the Collins' parameterized damage model [1]). The dashed line is the material boundary between slabs.

References [1] Collins G. S. et al. (2004) *MAPS*, *39*, 217. [2] Melosh H. J. (1979) *Journal of Geophysical Research: Solid Earth*, *84*, 7513–7520. [3] Pierazzo E. et al. (2008) *MAPS 43*, 1917. [4] Caldwell W. K. et al. (2021) *Applied Sciences*, *11*, 2504. [5] Weaver R. P. et al., Technical Report LA-UR-16-20205 LANL (2016). [6] Cheng A. F. et al. (2020) *Icarus*, *352*, 113989. [7] Kenkmann T. et al. (2018) *MAPS*, *53*, 1543. [8] Martellato E. et al. (2020) *JGR: Planets*, *125*, e2019JE006108. [9] Senft L. E. and Stewart S. T. (2008) *Meteoritics & Planetary Science*, *43*, 1993–2013. [10] Citron R. I. and Stewart S. T. (2022) *The Planetary Science Journal*, *3*, 116. [11] Kawazoe T. et al. (2009) *Physics of the Earth and Planetary Interiors*, *174*, 128–137.

MODELING MICROMETEORITE BOMBARDMENT INTO METAL TARGETS USING THE FLAG HYDROCODE.

M. C. Holmes, W. K. Caldwell, Los Alamos National Laboratory, Los Alamos, NM 87545, matthewh@lanl.gov, wkcaldwell@lanl.gov

Introduction: Microcratering on the millimeter scale is the dominant process causing erosion of rock surfaces exposed to the lunar environment [1]. The geometry of an impact crater can depend upon impactor size, velocity, and material as well as upon the target material, ambient pressure, and local gravity [2]. However, the main difference between microcraters and larger craters is that target strength dominates excavation in the former case, whereas gravity plays the dominant role in the latter [3]. Therefore, in order to accurately model micrometeorite impacts it is necessary for a hydrocode to incorporate a strength model to be applied to solid materials.

The free Lagrange (FLAG) hydrocode [4] developed at the Los Alamos National Laboratory is one such code. Furthermore, FLAG has undergone verification and validation processes with respect to impact cratering simulations to ensure accuracy of the results [5]. Hence, this code can help us better understand the effects of micrometeorite impacts into metal targets.

Research Plan: We are interested in micrometeorites with diameter on the order of $100\ \mu\mathrm{m}$. Target materials of interest include aluminum, copper, tin, glass, and Pyrex (borosilicate glass), while carbon, ceramics, concrete, and silicates are being considered for the projectile's composition.

Ultimately we are interested in repeated as well as nearly simultaneous impacts into a single target. To this end, we will study impacts into existing microcraters, as well as initialize simulations with multiple impactors to strike a single target.

Preliminary Results: Within the 2D axisymmetric geometry we model an aluminum impactor striking an aluminum target, both being modeled within FLAG as fluids, and compare impact craters as a function of impactor diameter. Figure 1 shows results from simulations with impactor diameters of (from left to right) $L = 100,\ 500,$ and $1000\ \mu\mathrm{m}$, and each with impact velocity $v_i = 5000\ \mathrm{m/s}$ and mesh resolution of 10 cells per projectile radius.

The computational domain and geometry are scaled with L to facilitate direct visual comparison. We note that the three craters are nearly identical up to scaling when compared at a time which is a multiple of τ, where $\tau = L/v_i$ depends on L.

References

[1] F. Hörz, J. B. Hartung, and D. E. Gault. Micrometeorite craters on lunar rock surfaces. *Journal of Geophysical Research*, 76(23):5770–5798, 1971.

[2] K. A. Holsapple and R. M. Schmidt. On the scaling of crater dimensions: 2. impact processes. *Journal of Geophysical Research*, 87(B3):1849–1870, 1982.

[3] H. J. Melosh. *Impact cratering: a geologic process*. Oxford University Press, Inc., 1989.

[4] James L. Hill. Flag user's manual. Technical report, Los Alamos National Laboratory, January 2017. LA-CP-17-20057.

[5] W. K. Caldwell, A. Hunter, C. S. Plesko, and S. Wirkus. Verification and validation of the flag hydrocode for impact cratering simulations. *Journal of Verification, Validation and Uncertainty Quantification*, 3(3):031004 (9 pages), 2018.

Acknowledgements: This work was supported by the Advanced Simulation and Computing (ASC)–Verification and Validation (V&V) program at LANL. Los Alamos National Laboratory, an affirmative action/equal opportunity employer, is operated by Triad National Security, LLC, for the National Nuclear Security Administration of the U.S. Department of Energy under contract 89233218NCA000001.

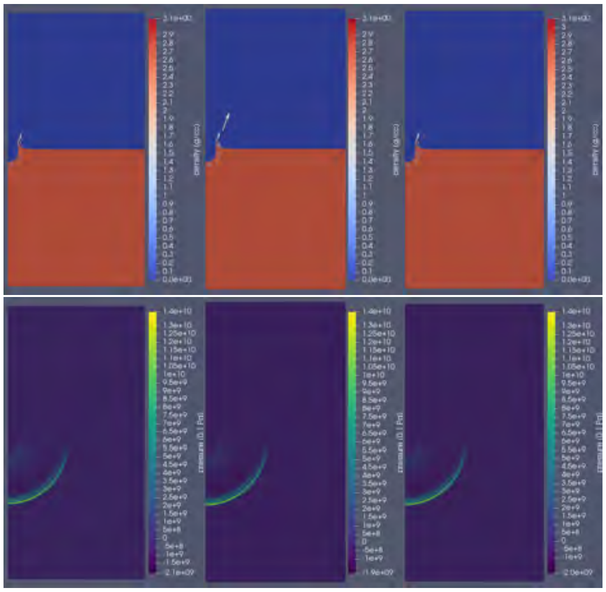

Figure 1: Density, velocity, and pressure data at approximate simulation time $t = 10\tau$.

UPDATE ON THE MORPHOMETRIC MEASUREMENTS FOR THE ROBBINS LUNAR CRATER DATABASE.

R. H. Hoover*[1,2], S. J. Robins[1] and B. M. Hynek[2] *rhoover@boulder.swri.edu, [1]Southwest Research Institute, 1050 Walnut St #300, Boulder, [2]Department of Geological Sciences, University of Colorado Boulder, CO 80309

Background: Impact cratering is one of the most common geologic processes across the solar system, and studying the impact craters of any particular body can provide insight into wide variety of planetary science questions. Researching impact craters can help answer questions relating to modern day surface processes affecting a body, surface and near surface geology, past and present impactor populations, and safety of potential landing sites. Additionally, impact cratering occurs on all solid surface bodies in the solar system and studying variations and differences of those impact craters are important for assessing geologic differences and similarities between planetary bodies. In this research, we have been and are continuing to collect and analyze the morphometric properties of lunar impact craters >1 km in diameter (D).

Motivation: Robbins has recently complied a lunar crater database, identifying the location and diameter for approximately all 1.3 million craters $D > 1$ km.[1] The purpose of this research is to semi-manually calculate the depth of each crater identified in that database to be a better reference for the community.

Methods: Three main topographic datasets are used to collect morphometric data for the lunar crater database. The datasets include the Lunar Orbiter Laser Altimeter (LOLA) Reduced Data Record (RDR) data product[2], the Kaguya DTM tied with LOLA data with ±60° coverage[3], and the Lunar Reconnaissance Orbiter Camera (LROC) Wide Angle Camera (WAC) stereo-based topographic product with ±85° coverage[4]. LOLA RDR and the Kaguya DTM will be used for all measurements ±60°, LROC WAC and LOLA RDR will be used for ±60°-85°, and only LOLA RDR will be used for the poles. The LOLA RDR is acquired from the NASA Planetary Data System LOLA RDR Query Tool V2.0 and is provided as a .CSV file with latitude, longitude, and topography of each data point. The WAC DTM and Kaguya DTM are acquired from the USGS PDS Cartography and imaging Science Node. LOLA RDR are used for the entire Moon, while the stereo-based data are used where they exist. Using multiple datasets for the same kinds of measurements will allow us to determine if there are any biases in the data.

Morphometric measurements are collected for crater rim elevation, surrounding surface elevation, floor depth, and crater volume, using a code written by Robbins in *Igor* which allows for a semi-automated/-manual extraction of these data. The Moon is divided into 20°×22.5°±0.2° sub regions, plus a region for each pole, to help manage file and data volume for a total of 130 sub-regions.

Topographic data and the locations and diameters of all craters are first loaded into the program *Igor*. To measure each individual crater, *Igor* first draws simple, ideal circles for the crater rim, 50% of that to encompass the floor, and then 200%–300% as an annulus for the surrounding surface. The user then checks the location of the polygons to confirm the identification of each feature (e.g., can you see a crater in the topography? is it offset?) and adjust the location of the features as necessary. For example, if the crater rim of a nearby crater intersects the crater rim of interest, the area of intersection will be removed from the polygon identifying the crater rim to ensure that the measurement only includes the rim of the crater of interest. After checking, adjusting, or manually drawing the polygons, *Igor* runs an automated code to identify data points from the DTM and LOLA RDR within each polygon to determine the rim elevation, the crater floor elevation and the elevation of the surround surface. These are points-within-a-polygon calculations except for the rim, where the highest points within a small neighborhood are found and saved. Additionally, any data within 1 crater radius of any other existing comparably-sized crater or smaller are removed so they will not affect the depth calculations. Once these elevations have been determined, the code stores them in a data table and they are used to estimate crater depth and crater volume.

Results: Collection of the depth measurements is currently ongoing, and at the time of this abstract submission it is ~40% complete. Hoover has currently completed measurements for craters $D = 1$–25 km for 48 sub-regions. This includes all regions ±60° latitude and 0°–180° longitude. The Kaguya DTM and the LOLA RDR were used for these particular measurements. Figure 1 displays the current set of depth versus diameter data from Kaguya and LOLA for approximately 615,000 craters. Figure 2 displays the depth measurement from Kaguya compared to LOLA for the same set of craters. As seen in Figures 1 and 2, there is very good agreement between the two, as one would hope and expect, though depths tend to be slightly deeper in the laser shot data. This is likely because the laser is good enough to capture fine-scale topography that the raster data cannot. This sort of mismatch will be studied once data are fully gathered, for it has implications in these sorts of measurements for any body and from any instrument.

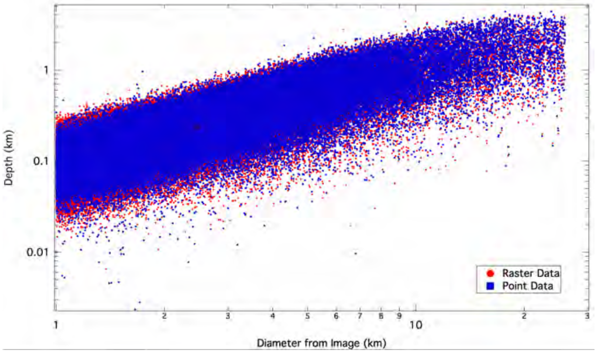

Figure 1: Depth versus diameter plot of craters ±60° latitude and 0°-180° longitude. Raster data shown in red indicates measurements from the Kaguya DTM while point data displayed in blue indicates measurements from LOLA RDR.

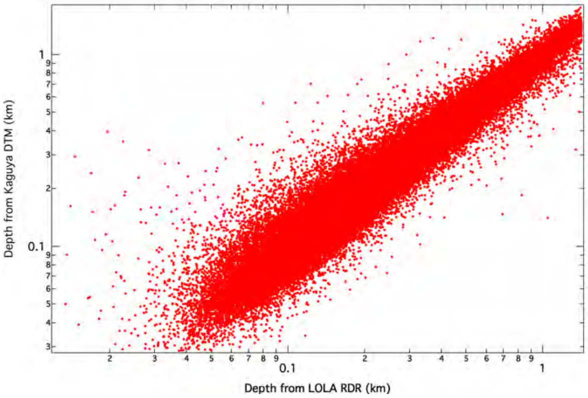

Figure 2: Depth measurements of craters ±60° latitude and 0°-180° longitude from the Kaguya DTM compared to depth measurements from LOLA RDR.

Ongoing Data Collection: Measurements for all craters D = 1–25 km and ±60° latitude using the Kaguya DTM and LOLA RDR data are ongoing and will be near completion by August. The next step will be to measure the craters >25 km for all regions and then collect measurements for polar craters using LROC-WAC DTMs and LOLA RDR data. Progress and updates will be complied for presentation at the 13th Planetary Crater Consortium Meeting.

References: [1] Robbins, (2019) *JGR Planets* **124:4**, 871-892. [2] Neumann, (2009) *Lunar Orbiter laser Altimeter Raw Data Set*, LRO-L-LOLA-3-RDR-V1.0, NASA Planetary Data System, 2010. [3] Baker et al., (2016) *Icarus* **273**, 346-355. [4] Wagner et al., (2015) *46th LPSC* Abstract #1473.

UNDERSTANDING THE GLOBAL SPATIAL DISTRIBUTION OF IMPACT CRATERS ON THE MOON USING THE BUFFERED NON-SPARSENESS CORRECTION TECHNIQUE.

Y. H. Huang[1], C. Riedel[2], J. M. Soderblom[1], S. B. Krein[1], C. Orgel[3,4], M. Hirabayashi[5], D. A. Minton[6], [1]Department of Earth, Atmospheric, and Planetary Sciences, Massachusetts Institute of Technology, Cambridge, Massachusetts 02139, USA (yahuei@mit.edu), [2]Institute of Computer Science, University of Potsdam, Potsdam, Germany 14476, [3] Institute of Geological Science, Freie Universität, Berlin, Germany, [4] European Space Research and Technology Centre (ESA/ESTEC), Noordwijk, The Netherlands, [5]Department of Aerospace Engineering, Auburn University, Auburn, Alabama 36849 USA, [6]Department of Earth, Atmopsheric, and Planetary Sciences, Purdue University, West Lafayette, Indiana 47907 USA.

Summary of updated lunar crater density map and spatial analysis: We previously updated the global density of all lunar impact craters ≥20 kilometers in diameter [1] (Figure 1), initially produced by Head et al. [2], by using the buffered non-sparseness correction technique (BNSC) [3–5]. Younger surfaces such as Procellarum KREEP Terrane and Orientale and Moscoviense Basins regions exhibit similar results for BNSC and traditional crater counting (TRAD) approaches, while older surfaces, such as the southern nearside and farside highlands exhibit more significant differences with the BNSC approach. We confirm this result from a statistical breakpoint analysis (Figure 2) and Z-statistics (Figure 3) for global lunar craters ≥20 km in diameter.

Method: To derive a global lunar crater number density map, we applied the TRAD approach and the BNSC technique to the lunar crater catalog updated by Kadish et al., [6] from the original catalog by Head et al., [2]. This global lunar catalog counts 5158 craters of ≥20 km in diameter. We considered 400 nodes distributed in a quasi equal-area fashion and then determined the surface density of craters ≥20 km in diameter by calculating the crater number density within a radius of 450 km centered on each node. In the final map, the density values represented in each raster cell correspond to the mean crater density value of all overlapping circular reference areas. The TRAD approach reflects the total number of all craters that fall within the 450 km-diameter circles (equal crater count area), while the BNSC technique assigns a new reference area for each individual crater within each node. For a given crater that is evaluated, its new reference area excludes the area of any larger craters and their ejecta [3–5].

Results: We statistically analyze relationships between the BNSC-derived and TRAD-derived global lunar crater densities (Figures 2–3). Global TRAD-derived N(20) values appear to roll over, accompanied by a greater variation, while global BNSC-derived N(20) values are close to double the TRAD-derived value. This relationship is better characterized by at least two slope breaks at BNSC-derived N(20) values of 85 and 278. The regime with the global lunar crater N(20) number density of <85 depicts a nearly 1-to-1 relationship, suggesting that the ≥20 km-in-diameter-forming events for the youngest surfaces, e.g., the western PKT, are sparsely distributed. Outside this part of the lunar surface, the global lunar crater number density N(20) experiences nonsparseness. The BNSC measurements on surface units with ≥2% of geometric saturation, defined by traditional crater counts, increases nonlinearly. This suggests that the lunar highlands' cratering record with ≥2% of geometric saturation is likely to have been affected by geometric overlapping of ≥20 km-in-diameter craters.

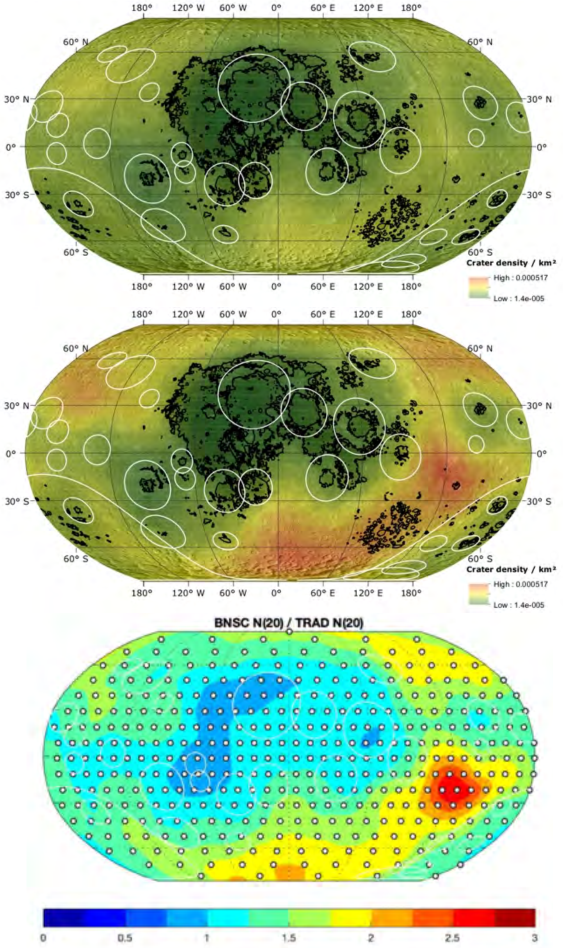

Figure 1: Global lunar crater density map in a Robinson projection (craters ≥20 km in diameter). The top and middle panels represent the map using the traditional crater counting and the buffered non-sparseness correction, while the bottom panel shows the difference between these two approaches in the unit of ratio with color scheme binning into 0.25. White circles highlight

basins with available absolute model ages [5]. White data points in the bottom panel show the nodes for calculating crater density. The unit of crater density is in km^2, and the conventional N(20) can be obtained by multiplying 10^{6}km^2 to the displayed numbers ranging from 1.4×10^{-5} to 5.17×10^{-4} km^{-2}.

We apply Z-statistics to the global TRAD-derived lunar crater number density to provide insight into the spatial relationships between the visible crater distribution [7-10] and a degree of crater saturation (Figure 3). Z-statistics uses information of crater count area size, nearest neighbor distances, and the number of points to evaluate the spatial distributions. We calculate Z-scores by $Z = (d_{obs} - d_{exp})/\sigma$, where d_{obs} is the mean value of the observed nearest distance distribution for any pair of points, and d_{exp} and σ are the expected nearest distance and standard deviation for a given number of points (n) and a sector area (A) from Poisson process [11]. The d_{exp} is expressed as $0.5/\sqrt{n/A}$, and the σ is $\sqrt{(4-\pi)A/(4\pi n^2)}$. The random distribution depicts Z-scores ranging from -1 to 1. Negative Z-scores indicate that the observed nearest distance distribution of points is smaller than the one expected from a random distribution; therefore, the distribution is clustered. Conversely, positive Z-scores indicate an ordered distribution. Note that the Z-score estimated from the numerical approach [8] should be similar to the analytical Z-scores [12].

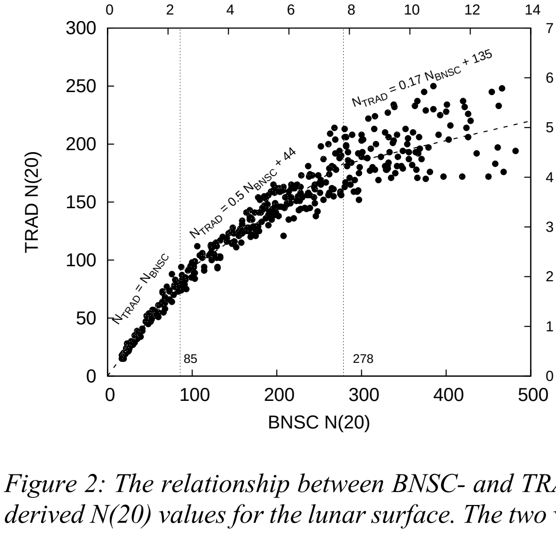

Figure 2: The relationship between BNSC- and TRAD-derived N(20) values for the lunar surface. The two vertical dash lines mark a statistically significant breakpoint at BNSC-derived N(20) values of 85 and 278 from Bayesian Information Criterion analysis[13,14], representing the best-fit slopes for each regime. The geometric saturation rate on the secondary axes is calculated from Gault [15].

Implications: The relationship between the ratio of BNSC-derived N(20) values to TRAD-derived N(20) values and the analytical Z-scores for the lunar surface, as shown in Figure 3, are generally consistent with our results from the global crater density measurement. The youngest surfaces, such as the western PKT and Orientale Basin formation, have not reached a crater saturation for the crater diameter of ≥20 km, corresponding to the analytical Z-scores ranging from -2 and 2 and the ratio ranging from 0.8 to ~1.2, whereas the lunar surface with craters that TRAD-derived and BNSC-derived N(20) differs more deviate from the random distribution and exhibits more uniforum (Z-scores range from 2 to 10), supporting previous findings on uniform distributions for non-sparsely distributed craters on the icy moons and the Moon [e.g., 9].

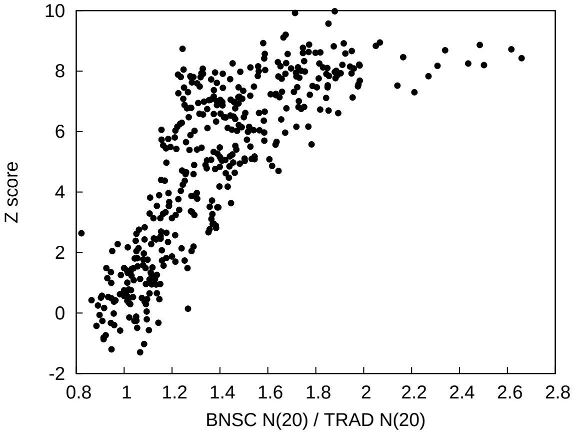

Figure 3: The relationship between the ratio of BNSC-derived N(20) to TRAD-derived N(20) values and the analytical Z-scores.

Acknowledgments: This research was supported by Lunar Data Analysis Program grant 80NSSC20K1417.

References: [1] Huang, Y.H. et al. *Lunar Planet. Sci. Conf.* 53rd (2022). [2] Head, J. et al., *Science* 329, 1504–1507, (2010). [3] Kneissl, T. et al., *Icarus*, 277, 187–195, (2016) [4] Riedel, C. et al., *Earth and Space Science*, 5, 258–267, (2018). [5] Orgel, C. et al. *J. Geophys. Res.: Planets,* 123, 748–762, (2018). [6] Kadish, S. J. et al., *Lunar Planet. Sci. Conf.* 42nd (2011). [7] Squyres, S.W. et al. *Icarus*, 125, 67-82 (1997). [8] Michael, G. et al. *Icarus*, 277, 279-285 (2016). [9] Kirchoff, M. Meteorit. Planet. Sci., 53(4), 874-890 (2018). [10] Riedel, C. et al. *J. Geophys. Res.: Planets,* 126(3), e2020JE006693 (2021). [11] Clark, P.J. and Evans, F. C. *Ecology* 35, 445-453 (1954). [12] Hirata, H. *Icarus*, 288, 69-77 (2017). [13] Jeffreys, H. *Theorey of Probability* (1961). [14] Kass, R. E. and L. Wasserman *J. Am. Stat. Assoc.*, 90, 928-934 (1995). [15] Gault, D. E. *Radio Sci.,* 5(2), 273-291 (1970).

UPDATES ON THE SEARCH FOR TERTIARY CRATERS (SECONDARY CRATERS OF SECONDARY CRATERS) ON THE MOON.

M. R. Huffman and K. N. Singer, Southwest Research Institute (mikaylarhuffman@gmail.com).

Introduction: Impact cratering events are relevant for geochronology, planetary formation, and providing data-based checks for theory. Each primary cratering event produces ejecta, fragments of which can reimpact the surface, creating secondary impact craters [1]. Secondary craters could produce their own ejecta, which could again impact the surface, creating secondaries of secondaries – known as tertiary impact craters.

Tertiary craters have been discussed a few times in the literature [1], but are difficult to identify. With the help of high resolution images from the Lunar Reconnaissance Orbiter Camera (LROC) Narrow Angle Camera (NAC), we are the first (to our knowledge) to make a concerted effort to systematically search for tertiary craters on the Moon.

We present a set of tertiary craters from a small, fresh primary crater to the SSW of Glushko crater on the Moon. We informally refer to this unnamed crater as "Wallace." Wallace is ~1.8 km in diameter and is located at 281.054°E, 3.100°N.

Image Processing and Analysis: We used the LROC Wide Angle Camera (WAC) global mosaic, the WAC global mosaic with no shadows, and the LRO DIVINER H-Parameter Map to search for young, fresh primary craters [2]. We then processed selected WAC and NAC images in the USGS ISIS program and analyzed and mapped processed images in ArcGIS Pro using geodesic distances. See [3] for more information regarding our methodology.

Results: We mapped 9,404 secondary craters around Wallace to date. We focus on two tertiary-producing secondary craters. Both are 9.6 km to the NNW of Wallace. The first, which we informally refer to as "Gromit," is 62 m in diameter, and is located at 280.996°E, 3.413°N. The second, which we call "Cheese," is 42 m in diameter and is located at 280.995°E, 3.407°N. We determined these are most likely to be secondary craters of Wallace (and not just scoured small primaries) in [3].

We have mapped 14 confirmed tertiary craters around Gromit, with 62 additional potential tertiary craters. Cheese has 1 confirmed associated tertiary crater. We use several characteristics to identify the craters most likely to be tertiary impacts [4]:

1. Extreme elliptical shape, with the long axis aligning more closely with the productive secondary than with the primary,
2. Downrange associated projectile, sometimes with boulder trails leading to the tertiary, whose direction from the tertiary is more closely aligned with ejection from the secondary than from the primary,
3. Shallow depths, with small depth to diameter ratios, and
4. Reasonable size-ratio compared to the size of the productive secondary crater.

If a potential tertiary crater has all of these aspects we call it a "confirmed" tertiary.

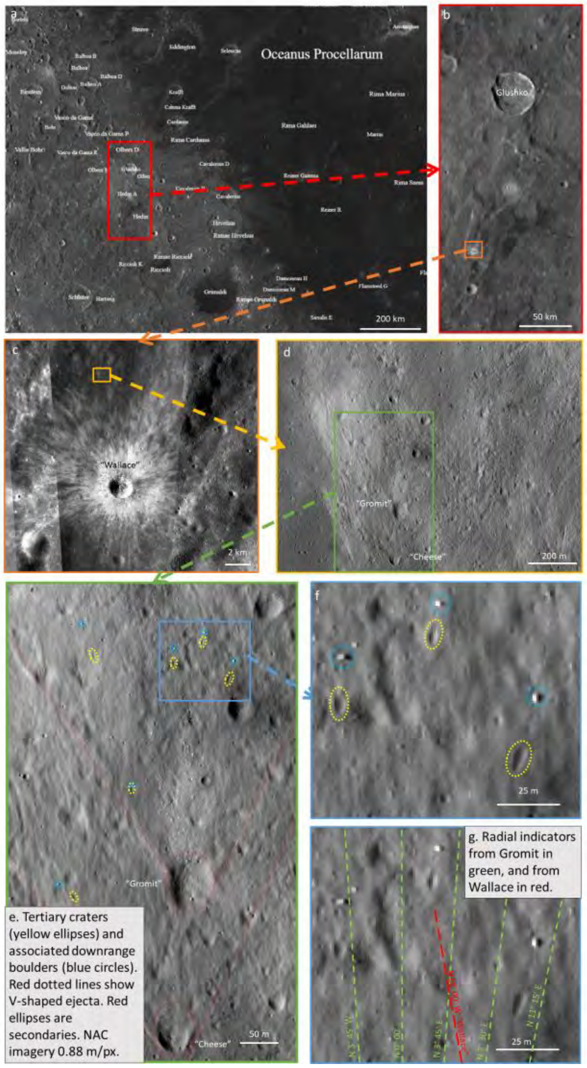

e. Tertiary craters (yellow ellipses) and associated downrange boulders (blue circles). Red dotted lines show V-shaped ejecta. Red ellipses are secondaries. NAC imagery 0.88 m/px.

g. Radial indicators from Gromit in green, and from Wallace in red.

Fig 1: Wallace (primary crater), Gromit (secondary crater), and Cheese (secondary crater) in context, as well as several examples of tertiary craters. The most likely tertiary craters are elongated dents radial to the secondaries, many of which have downrange boulders.

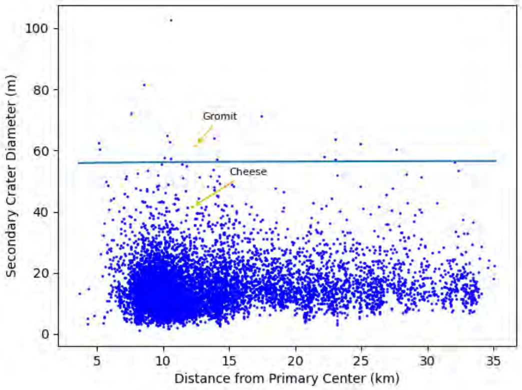

Fig 2: The distribution of Wallace's secondary craters. The diameter of each secondary crater is shown compared to its distance from Wallace's center. The 99th quantile of the distribution is plotted as a blue line. Gromit and Cheese are shown in orange.

Discussion: The largest secondary craters tend to be 4-6% the size of their productive primary, although a few can be a bit larger [5, 6, 7, 8]. Gromit's confirmed tertiaries are 4.9±1.5 m, which is 7.9±2.4% the size of Gromit. These are slightly larger than the 4-6% rule of thumb, but overlaps within uncertainty. In addition, we used only the largest, most identifiable tertiaries for this analysis. If the smaller potential tertiaries were included, it would likely drive this value down. Cheese's tertiary is 3.8 m in diameter, which is 9.2% of Cheese's diameter. Cheese's tertiary's morphology includes all four of the characteristics outlined above.

Several of these tertiary craters (~39%) have associated downrange boulders that are presumably an ejecta fragment from the secondary that that created the tertiary and then bounced out and arrived at its current location. We calculated the impact velocity and "bounce" velocities of these tertiary-forming ejecta fragments/boulders using the tertiary distance from the secondary and the boulder distance from the tertiary. We also estimated the mass of the boulder from its size and an assumed density of 2875 kg/m^3 (Wallace lays near the boundary of the Mare and Highlands, thus we use an intermediate value) [9].

Although scaling laws [e.g., 10] are formulated around hypervelocity impact events, we checked the sizes of impactors that would be predicted given the tertiary sizes and the boulder impact velocities from [11], eqn 5. We estimated the size of the impactor that would have produced the tertiaries for the strength regime (due to the small size of our craters and relatively low impact velocities [3, 4]). We compare this to the measured boulder sizes to provide a data-based check on scaling laws at these low velocities. The observed boulder sizes fall between the end member predictions of tertiary-forming impactor sizes using a solid, hard rock surface and a more porous, regolith surface (approximated by sand with a bit of strength).

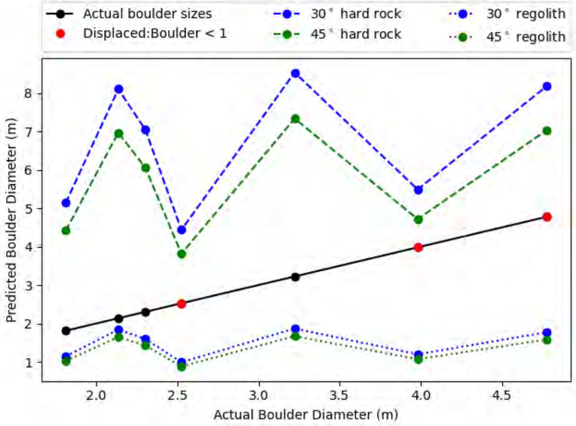

Fig 3: Actual boulder sizes compared to estimated tertiary-forming impactor sizes. For each tertiary, we calculated a predicted impactor size using the scaling relations, the size of the tertiary, and the tertiary-forming impactor velocity. The black line has a slope of one, since it shows the actual boulder sizes plotted against themselves. Red dots represent boulder-tertiary pairs where the tertiary's displaced volume is less than the measured volume of the boulder. The non-solid lines are the predicted tertiary-forming impactor sizes, all in the strength regime. The top, dashed lines are for a hard rock surface and the bottom, dotted lines are for a regolith surface.

Future Work: We continue our systematic search for other tertiary-producing primaries on the Moon. After assembling a dataset of fresh primaries with well-preserved secondary fields, we will investigate the freshest ones for more tertiary craters. We will also compare our findings to more theory-based predictions.

Acknowledgments: We thank NASA's Solar System Workings program for funding.

References: [1] Melosh H. J. (1989). [2] NASA, ASU, and ACT. Lunar QuickMap. [3] Huffman M. R. and Singer K. N. (2022) *LPSC53*, Abstract #2018. [4] Huffman M. R. (2022) *Undergraduate Honors Theses, William & Mary*, Paper 1853. [5] McEwen A. S. and Bierhaus E. B. (2006) *Earth and Planet. Sci., 34*, 535-567. [6] Allen C. C. (1979) *Geophys. Research Letters., 6.1*, 51-54. [7] Schultz P. H. and Singer J. (1980), *LPSC11*, Abstract #1370. [8] Xiao Z. et al. (2014) *Icarus, 228*, 260-275. [9] Kiefer W. S. et al. (2012) *Geophys. Research Letters., 39.7*. [10] Housen K. R. and Holsapple K. A. (2011) *Icarus, 211*, 856-875. [11] Singer K. N. et al. (2020) *JGR Planets, 125.8*.

PRELIMINARY RESULTS FROM CRATER MAPPING AND ANALYSIS FOR THE SOUTH POLAR LAYERED DEPOSITS, MARS.

M. E. Landis[1], M. E. DeCoster[2], A. M. Stickle[2], E. G. Rivera-Valentín[3], [1]Laboratory for Atmospheric and Space Physics, University of Colorado, Boulder, CO (margaret.landis@lasp.colorado.edu), [2]Johns Hopkins University Applied Physics Laboratory, Laurel, MD, [3]Lunar and Planetary Institute (USRA), Houston, TX.

Introduction The South Polar Layered Deposits (SPLD) on Mars represent the larger of the two surface ice sheets that combined contain approximately the same volume as the Greenland ice sheet ([1], and references therein). This large volume of water ice is key to understanding the long-term water supply to the martian atmosphere, including changes in climate in the recent past. However, while the surface of the North Polar Layered Deposits (NPLD) provides evidence for clear climate changes or resurfacing events in the geologically recent past (e.g., [2-4]), the geologic history and surface ages of the SPLD are not well constrained. Estimates range from a few hundred thousand years to Myrs, depending on the size of craters counted and crater production function used to interpret the results [5-7]. Recent small impacts on the SPLD indicate that the upper few meters in some locations may be composed primarily of dust or very-dusty ice [8], suggesting that a long-term hiatus in accumulation may be occurring.

This fundamental issue of the SPLD surface exposure age, combined with expanded higher-resolution image coverage since the last cratering studies were undertaken, improvements in understanding impactor populations from multiple sources, and ability to use impact cratering simulations with layered targets (more similar to the SPLD than pure water ice or dust/bedrock) are motivation for us to revisit cataloging the SPLD impact craters to interpret what their distribution can tell us about the history of this largest extant surface ice sheet on Mars.

New crater catalog: The SPLD surface has been divided into two geologic units, Planum Australe 1 (Aa1) and Planum Australe 2 (Aa2) by [9]. Aa2 includes most of the SPLD surface, including most of the region of interest from which we are presenting crater morphologies (Fig. 1, each catalog feature is a green dot). Aa1 underlies Aa2 and makes up the geologic unit containing the troughs near the South Pole Residual Cap (SPRC) and a significant portion of Promethei Lingula (~80-85° S, ~110° E). New small impacts into the SPLD [8] also occur in the Aa2 region, suggesting that the upper few meters of material in the Aa2 region are dominated by lower-albedo, dusty material.

We use Mars Reconnaissance Orbiter (MRO) Context Camera (CTX) data from solar longitude (Ls) 230° to 10° the subsequent Mars Year to record the location and diameter of craters using USGS Crater Helper Tools. CTX images were binned to 6 m/pixel resolution. CTX data covers most of the SPLD in this seasonal time frame, with significant gaps in coverage occurring outside the area from which we present craters (Fig. 1). We have now counted ~600 circular features ranging from ~100 m to ~28 km diameter in the region shown in Fig. 1, including one secondary crater field around McMurdo crater (Fig. 1 red box, Fig. 2).

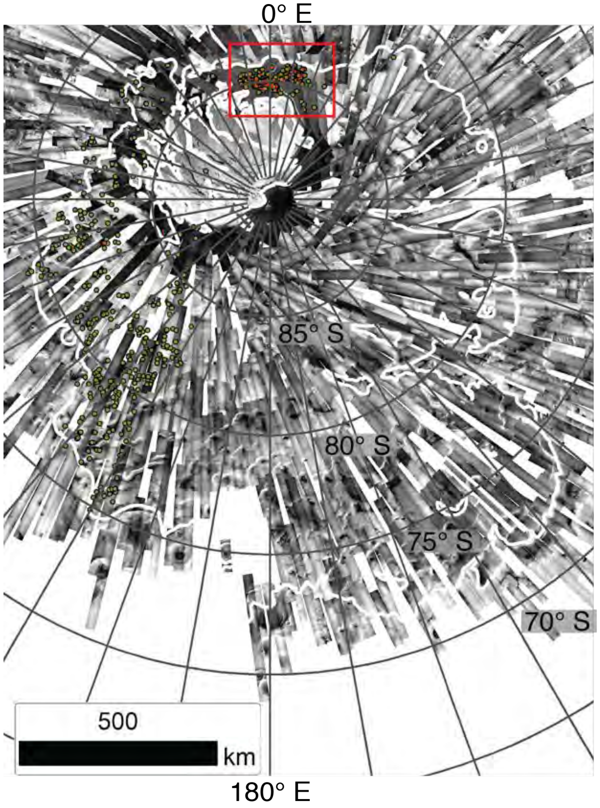

Figure 1. *Map of the current circular features cataloged (green dots) for the SPLD region. White polygon shows the edge of the SPLD. Background is CTX data used for crater counting. Secondary crater field around McMurdo crater is shown in a red box.*

Crater Statistics: Due to the challenging nature of the SPLD surface, we take an approach where we assign each crater a confidence level, from 1 (definitely a crater) through 3 (slightly more likely to be a crater than not) and a preservation state, with 1 being incredibly well preserved with a raised rim and ejecta, through 3 where it is near erasure. We tracked "ghost craters" (where only a circular rim remains) and secondary craters from McMurdo as separate preservation state categories. We tracked circular features that were unlikely to be craters as well. These were included for completeness and as a non-crater statistical comparison to the other confidence categories of craters, which were all compared to each other to look for statistical difference. Craters that are part of a secondary field around McMurdo crater (Fig. 2) that show a statistically distinct cumulative crater size-frequency distribution (SFD) slope from the crater population that does not include obvious secondaries.

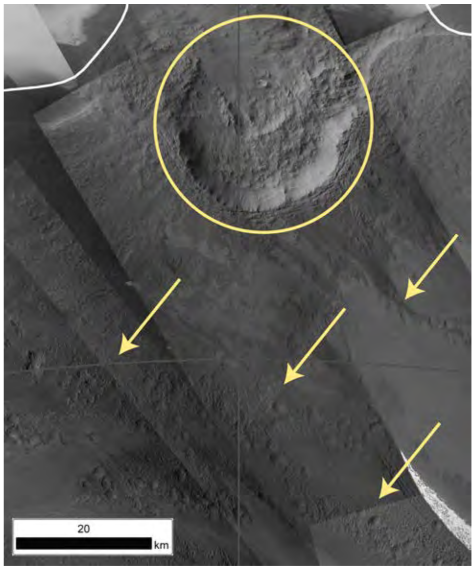

Figure 2. *McMurdo secondary crater field (part of the red box in Fig. 1) shown. McMurdo crater is circled, potential chains of secondary craters are pointed out by the arrows.*

The cumulative size-frequency distribution plot [10] for the category 1 craters of all measured diameters is shown in Fig. 3a. The roll off diameter assumed from the resolution of the CTX images (~6 m/pixel) should be ~60 m, but we find it to be much higher here (~600-800 m) in part likely due to the complex nature of the surface. This difference is show in Fig. 3b, where the CSFD below the roll-off diameter is not shown. For the entire SPLD area counted, there do not appear to be statistically significant breaks in slope in the cumulative CSFD. Future work includes making a crater density map to test if there are significant spatial variations in crater density, and to determine if the bump at ~3 km becomes more statistically significant with counting of additional craters.

Crater Simulations: To understand the effect of the dusty ice on crater formation and final diameters compared to lithic targets frequently used for crater production functions, we are using CTH code with layered dust and ice targets to model these impacts. Initial results from a layered dust and ice target from one second after impact are shown in Fig. 4. Refinements to this model are part of future work, including considering ice/dust contents and vertical distributions from other studies of the SPLD.

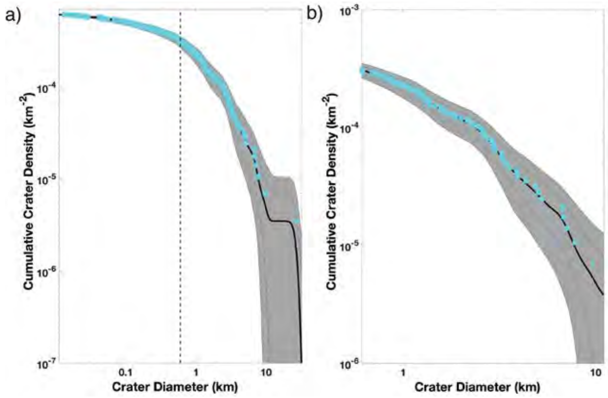

Figure 3. *Cumulative size-frequency distribution plots for the category 1 craters counted at time of writing. Cyan squares are the data with cyan error bars following Poisson statistics. The gray space follows the method for estimating cratering statistics suggested by [11], where the dashed black lines are 1-sigma and out to the gray area boundary is 2-sigma uncertainty.*

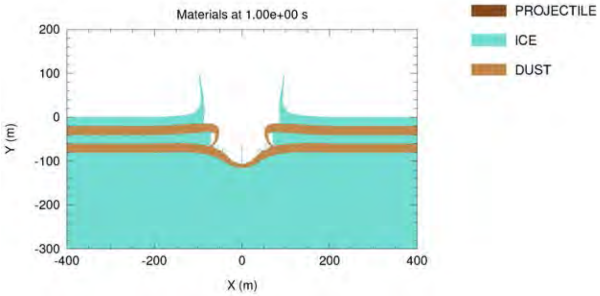

Figure 4. *A dunite projectile was simulated impacting into layers of dust (30% porosity, weakly consolidated silicate) and 5-phase ice [12] with alternating layers of 20 m of ice and 20 m of dust at the top of the target.*

Acknowledgments: This work was supported in part by MDAP 80NSSC20K0152.

References: [1] Byrne, S., (2009) *An. Rev.*, 2009. 37(1): p. 535-560. [2] Smith, I.B., et al., (2016) *Science*, 2016. 352(6289) [3] Banks, M.E., et. al., (2010) *JGR*, 2010. 115(E8). [4] Landis, M.E., et al., (2016) *GRL*, 43(7). [5] Herkenhoff, K. & J.J. Plaut (2000) *Icarus*. 144(2) [6] Koutnik, M., S. et al. (2002), JGR. 107(E11) [7] Landis, M.E., et al., LPI Contributions, 2018. 2086. [8] Landis, M.E., et al. 12th Planetary Crater Consortium (virtual). 2021. [9] Kolb, E.J. & K.L. Tanaka (2006) *Mars*. [10] Crater Analysis Techniques Working Group (1979). *Icarus*, 37(2). [11] Robbins, S.J., et al., (2018). *Icarus* 53(4): p. 891-931 [12] Senft, L.E. & S.T. Stewart, (2008) *M&PS*. 43(12).

THE SIZES OF IMPACTORS THAT FORMED ASTEROIDS FAMILIES. J. Leliwa-Kopystynski[1] and I. Wlodarczyk[2], [1]University of Warsaw, Institute of Geophysics, Pasteur 5, 02-093 Warszawa, Poland, jkopyst@mimuw.edu.pl, [2]Chorzow Astronomical Observatory, Al. Planetarium 4, 41-500 Chorzow, Poland, astrobit@ka.onet.pl

Introduction: The sizes of the impactors that produced 13 asteroid families (AFs) were estimated. Our starting data for the AFs considered here are these of [1]. The most probable impact velocity of the impactor originated from any of the six regions of the asteroid belt onto the parent body (PB) was calculated based on the results presented by [2], gathered in Table 1.

Table 1. Weighted average velocities of collision of asteroids located in one of the six belts (first column) and bombarded by an asteroid from any of these belts (second column). Twenty-one values of impact velocity and probability of occurring of an impact (calculated by [2] but not cited here) were used as the weights to calculate the weighted average of mutual impact velocities (third column). The belts' names and their ranges used by [2] differ slightly from those used by [1].

Table 1.

Belt	Ranges of major semiaxis	v_{imp} m s^{-1}
Inner	2.1 < a < 2.5 (3:1J)	5089
Middle	2.5 < a < 2.823 (5:2J)	5266
Pristine	2.823 < a < 2.956 (7:3J)	3670
Outer	2.956 < a < 3.28 (2:1J)	4634
Cybele	3.28 < a < 3.51	5042
High-inclination	sin i > 0.34 ($i > 20^0$) (ν6 secular resonance)	8920

Computation and results: The Vesta, Juno, and Euphrosyne families, with the impactor to PB size ratio equal to about 0.015, are exceptional. The PBs of these families lost only 0.0008, 0.0014, and 0.0061 of their mass, respectively. Densities of the impactor and PB's densities are poorly-known parameters that strongly influence the results. Thus, an estimation of the relative error $\Delta r_{imp}/r_{imp}$ made using the method of full differential with assumed values of the errors $\Delta\rho/\rho = 0.5$ (more or less arbitrary) and $\Delta v_{imp}/v_{imp} = 0.3$ (according to Table 1) leads to the radio $\Delta r_{imp}/r_{imp} \approx 0.4$.

Table 2

1 FIN	2 Family name	3 R_{LM} km	4 R_{PB} km	5 f	6 ρ kg m^{-3}	7 v_{imp} km s^{-1}	8 r_{imp} km	9 N
401	4 Vesta non-dif.	262.5	262.571	0.0008	3456	5.089	4.2	19170
502	15 Eunomia	115.844	118.048	0.055	2834	5.266	4.1	11571
404	20 Massalia	67.84	68.612	0.033	3224	5.089	1.5	26285
602	24 Themis	99	128.917	0.55	2780	4.634	10	5835
606	221 Eos	47.734	61.330	0.53	2710	4.634	3.0	16805
517	3815 Konig	10.064	15.084	0.70	1415	5.089	0.23	381
609	490 Veritas	59.402	64.321	0.21	3000	4.634	2.6	1835
406	163 Erigone	40.790	46.075	0.31	3000	5.089	1.5	2742
501	3 Juno	123.298	123.361	0.0014	3680	5.266	1.5	2866
504	128 Nemesis	81.258	82.270	0.052	1820	5.266	1.7	5835
505	145 Adeona	63.892	85.125	0.58	1820	5.266	4.2	10081
403	298 Baptistina	10.568	20.349	0.86	2000	5.089	0.44	3120
901	31 Euphrosyne	133.54	133.813	0.0061	1180	4.634	2.0	1867

The columns are:
1 – Family Identification Number,
3 – Radius of the Largest Member LM [3]
4 – Radius of the Parent Body PB calculated by us based on columns 3 and 9 with the assumption that the density of all FMs is the same.
5 – Fraction of mass lost by the PB during impact,
6 – Density of the LM, according to [3] or assumed. PB and impactor's density is assumed to be equal to that of LM.
7 – Impact velocity according to Table 1,
8 – The lower limit of the impactor radius is calculated using the formula

$$r_{imp}^3 = \frac{1}{\varepsilon} G \frac{8\pi}{5} R_{PB}^5 \rho v_{imp}^{-2} \left(1 - \left(\frac{R_{LM}}{R_{PB}} \right)^5 \right) \quad \text{with } \varepsilon = 1.$$

Here ε is the parameter. During an impact, the fraction (1 – ε) of impact energy E_{imp} is accumulated in the LM. It is used to break the intermolecular bonds inside its matter (deformation, crushing, powdering, heating).
The product εE_{imp} presents diminishing the PB's gravitational energy by rejecting a part of its mass equal to $M_{PB} – M_{LM}$.
9. – Number of the family members calculated by one of us (IW) using the Hierarchical Clustering Method. In this work, we used the database [4] actualized in 2018. It contains 463653 numbered asteroids.

References:

[1] [Nesvorny D. et al. (2015) *Asteroids IV*, 297-321. [2] Cibulkova et al. (2014) *Icarus*, 241, 358-372. [3] Carry B. (2012) *P&SS*, 73, 98-118. [4} (https://newton.spacedys.com/~astdys2/propsynth/all.syn).

Heavy metal cratering: impact experiments and simulations in Fe-Ni alloys

Simone Marchi & Amanda Alexander

Southwest Research Institute
Boulder, CO 80302, USA

Cratering is a prominent evolutionary process across the Solar System. Crater morphologies, regolith generation, bulk fracturing and projectile implantation are all examples of rocky planets and asteroid surface evolution resulting from impact processes. While a considerable body of literature is available on collisions on rocky/icy bodies, less work is available for metallic targets. The latter has become of wide interest due to the upcoming NASA Psyche mission, poised to study the likely metal-rich 225-km main belt asteroid, (16) Psyche.

In this work, we present a suite of impact experiments performed at the NASA Ames Vertical Gun Range facility on several types of iron meteorites and foundry-cast ingots that have similar Fe-Ni compositions. Our experiments were designed to better understand crater formation (e.g., size, depth), over a range of impact conditions, including target temperature and composition.

An unexpected observation from these experiments was extensive cracking of iron meteorites through the meteorite volume as a result of the hypervelocity impacts. Post-impact in situ analysis has been performed via X-ray computed tomography to quantify cracking properties within the bulk meteorite volume, and we discuss implications for Psyche’s porosity. We also present a suite of numerical simulations with iSALE and CTH shock physics codes aimed at reproducing the impact experiments (crater diameters and depths).

VISCOUS RELAXATION OF CRATERS ON PLUTO: POSSIBLE INDICATION OF EARLY HIGH HEAT FLOW.

William B. McKinnon[1], P. M. Schenk[2], M. T. Bland[3], K. N. Singer[4], and S. J. Robbins[4]; [1]Dept. Earth and Planet. Sci. & McDonnell Center for the Space Sci., Washington Univ. in St. Louis, Saint Louis, MO 63130 (mckinnon@wustl.edu), [2]LPI, Houston, TX 77058, [3]USGS Astrogeology, Flagstaff, AZ 86001, [4]SwRI, Boulder, CO 80302.

Introduction: Impact craters, with their well-defined initial shapes, have proven useful as heat flow probes of a number of icy bodies, provided characteristics of viscous relaxation can be identified (e.g., on Ganymede [1], Enceladus [2], and Ceres [3]). For Pluto's numerous craters such identifications are hampered/complicated by infilling and erosion by mobile, volatile ices, but not in every case [4]. Large craters offer relatively deep probes of rheological structure, and low-albedo regions are generally volatile-ice free. Two large, old craters in dark, western Cthulhu are probably the best examples for *possible* viscous relaxation on Pluto: Oort (~120-km diameter) and Edgeworth (~145-km diameter) (Fig. 1). They are similar enough in size, location, and apparent age (morphological preservation) that one suspects they resulted from the impact of a Kuiper belt binary, though we have no explicit evidence that they are in fact coeval. Edgeworth is particularly shallow (Fig. 1) and its floor appears bowed up above the original ground plane, a classic hallmark of viscous relaxation. In this presentation we will examine the evidence for the viscous relaxation of both Oort and Edgeworth, and derive constraints on Pluto's heat flow integrated through time.

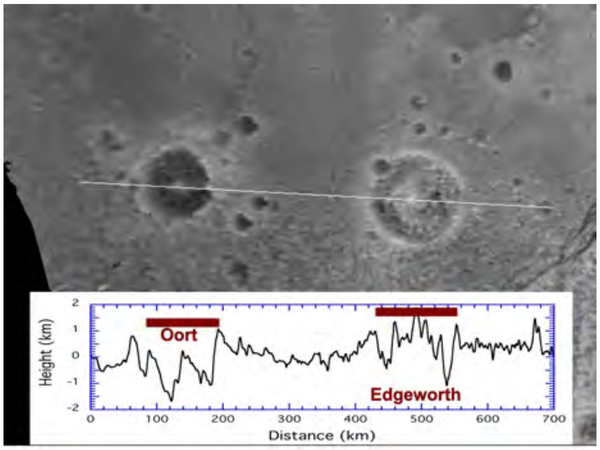

Figure 1. Stereo-derived digital terrain model (DTM) of western Cthulhu (from [5]), with transect. Both the general flatness of this terrain (see [6]) and the distinct appearances of Oort and Edgeworth are apparent. Noise increases in the DTM solution to the south (towards bottom). The only larger impacts seen on the *New Horizons* encounter hemisphere are the Burney multiring and great Sputnik basins.

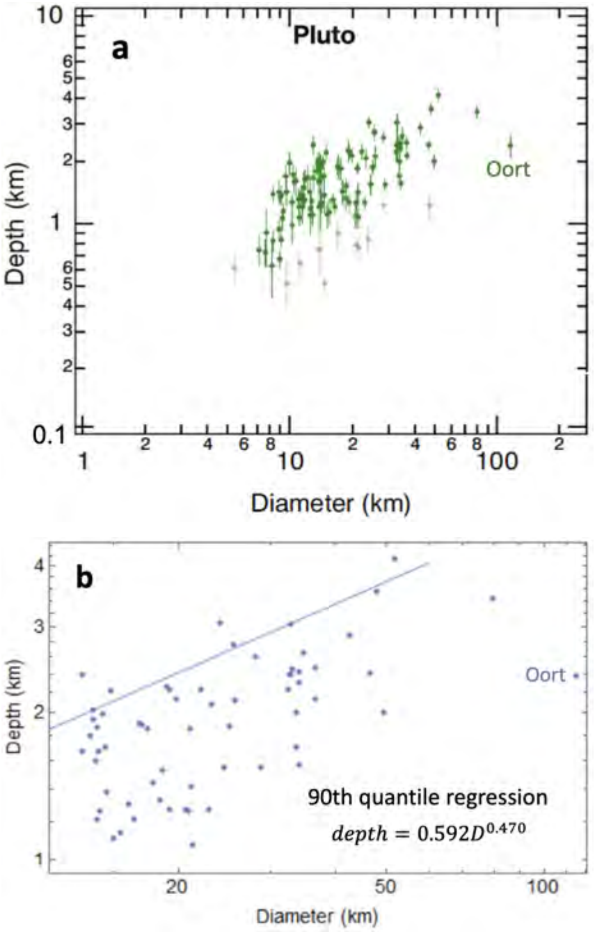

Figure 2. Rim-to-floor depths of (nominally) minimally modified craters on Pluto, from [7]. **(a)** All morphological types, with lighter shading for those that are shallower. **(b)** Example quantile regression fit (this work) for craters with $D > 13$ km, above the simple-to-complex transition [7]. Edgeworth, at $D \approx 145$ km, has an effective depth near 1 km [5].

Crater Depths on Pluto: In order to model the viscous relaxation of large craters we need to estimate their pristine, post-impact depths. We extrapolate from smaller, unrelaxed complex craters, utilizing the depth-diameter (d/D) data set generated by [7] from the 2018 DTM [5]. This data set (Fig. 2a) is more extensive and supersedes the depth/diameter data plotted for Pluto in [5]. Rather than fit the depth-diameter data as is, or even the deepest 75% per diameter bin [7], we use quantile regression to estimate the upper envelope of crater depths (illustrated in Fig. 2b). This is because the spread in depths at a given diameter clearly indicates a role for modification. That is, even if not obviously or manifestly eroded, infilling and/or burial may express subtly, especially at the resolutions available. For 90th, 95th, and 99th quantile regressions, we estimate the pristine rim-to-floor depth of Oort (115-km diameter in this data set) to have been 5.5/8.0/5.7 km, and that of Edgeworth to have been 6.1/9.1/6.2 km. These ranges are indicative of the systematic uncertainties involved in the extrapolation, but we judge that Edgeworth must have been at least 6 km deep originally, and now stands at a "relaxation fraction" of at least 85%,

Large craters on icy satellites are sometimes anomalously shallow regardless of viscous relaxation [8]. Europa is prime example, though in Europa's case the distinctive morphologies of its largest craters and ringed basins plus the overall geological youth of its surface indicate little if any role for viscous relaxation. The likely great age for Pluto's surface [4,9,10] and its largest craters does not allow for viscous relaxation to be dismissed. Moreover, the second largest crater in Fig. 1 is Elliot, an 80-km-diameter impact with clear evidence for nitrogen-ice infill that can easily account to its shallowness compared with the quantile regression fits.

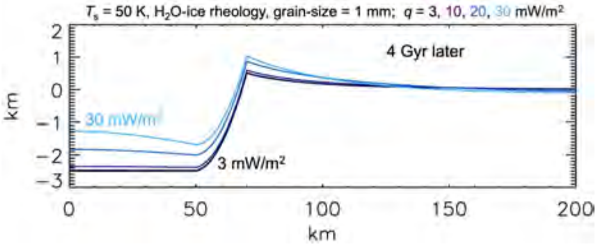

Figure 3. Preliminary finite element simulation of the relaxation of Edgeworth crater on Pluto, from [11]. Note that we argue that Edgeworth was initially substantially deeper than shown here.

Finite Element Models: We have begun a suite of finite element simulations along the lines of [1–3] but for Pluto specific conditions (e.g., 50 K surface, 0.62 m/s^2 surface gravity) (Fig. 3). Our preliminary calculations for Edgeworth [11] show that essentially no relaxation occurs over 4 billion years for a constant heat flow of 3 mW/m^2, and little for 5 mW/m^2. These are heat flows appropriate to Pluto's long-term evolution from radiogenic heating alone [12]. Not surprisingly, under such conditions Pluto's lithosphere is simply too cold and thick to relax or yield. To explain Edgeworth's (or Oort's) floor as a product of viscous relaxation requires warmer ice temperatures at depth (higher heat flows), from Fig. 3 at least 30 mW/m^2 over 4 billion years (heat flows that are not easy to explain [12]). In addition, both regolith and surface ice fracturing, as well as clathrate formation, could act to markedly lower surface ice conductivity and raise temperatures throughout Pluto's icy shell. We are exploring a range of sustained heat flows, early high-heat flow epochs, and effective higher surface temperatures in simulations of viscous relaxation of craters at these large scales on Pluto. New results and their implications will be presented at the meeting.

Acknowledgments: This work supported by NASA's *New Horizons* mission.

References: [1] Bland M. T. et al. (2017) *Icarus 296*, 275–288. [2] Bland M. T. et al. (2012) *GRL 39*, 17204. [3] Bland M. T. et al. (2016) *Nat. Geosci. 9*, 538–542. [4] Singer K. N. et al. (2021) in *Pluto System After New Horizons* (S. A. Stern et al., eds.) Univ of Ariz. Press, 121–145. [5] Schenk P. M. et al. (2018) *Icarus*, *314*, 400-433 [6] McKinnon W.B. et al. (2021) in *Pluto System After New Horizons* (S. A. Stern et al., eds.) Univ of Ariz. Press, 507–543. [7] Robbins S. J. et al. (2021) *Icarus 356*, 113902. [8] Schenk P. M. (2002) *Nature 417,* 419–420. [9] Moore J. M. et al. (2016) *Science 351*, 1284–1293. [10] Moore J. M. and McKinnon W. B. (2001) *Annu. Rev. Earth Planet. Sci. 49*, 173–200. [11] McKinnon W. B. (2018) *49th LPSC,* Abstract #2715. [12] Nimmo F. and McKinnon W.B. (2021) in *Pluto System After New Horizons* (S. A. Stern et al., eds.) Univ of Ariz. Press, 89–103.

DECAYING OBLIQUE ORBITS AS A HYPOTHESIS FOR THE ORIGIN OF NEARLY HORIZONTAL IMPACT CRATERS - A SURVEY OF SOME CANDIDATE PATERAE ON MARS.

R. B. Moore, Member of the Royal Society of Victoria (Australia) science@academicmail.org

Introduction: Paterae (literally shallow bowl) are unusually-shaped features that may occur in lowlands or highlands and may or may not be related to known geological causes such as volcanoes tectonism or impacts. The definition refers to a bowl because often volcanic craters and impact basins are of that shape, if occasionally distended. An example is Orcus patera on Mars. One of many theories for its origin, has been given anecdotally as being from an impact with a shallow or oblique impact angle. It is interesting to ask how common such events may be, as the spatial frequency of such features can aid in obtaining confidence that the attributed cause is correct. Until such an observational survey has been undertaken, modelling remains constrained by a lack of proposed examples.

By contrast, a*b initio* modelling done without reference to actual examples has been completed in 2013 by Elbeshausen [1] and showed that in cases of impacts between 5° and 10° from horizontal a significant proportion of the meteorite survives and may even form a secondary crater ahead of the first impact. The question arises: under what circumstances do such impacts occur, for instance from what direction relative to the ecliptic and the celestial equator of the body being impacted.

The possibility of multiple impacts, beyond two, with each impact being near horizontal (also called extremely "oblique") has been raised regarding Earth [2][3] and as such it was proposed [3][4] that a rubble pile asteroid may dissociate, perhaps even in space, due to some gravitational influence, and it's parts then impact a planet. Alternatively, dissociation may occur upon interaction with a target planet's gravity and atmosphere combined. The current study investigates how a non-equatorially aligned approach angle, and rather a relative N-S compass heading, may signify a lack of opportunity for moons to absorb such collisions as orthogonal impacts.

Methods: Paterae of Mars were surveyed using the digital elevation model (DEM) mode of ESRI ArcGIS [5]. Moon orbits were only generally factored into the hypothesis in the sense that because moons travel, on average, close to the plane of the ecliptic, that plane may be taken as an average moon orbital plane. As such the hypothesis can be tested: that if selected patera are due to oblique impacts, then moons can perhaps have intervened little in the asteroid's interaction with the target planet. A dataset containing a significant proportion of paterae of this type being equatorially aligned would tend to not support the model. Any paterae (such as volcanoes and faults) that are clearly not candidates as oblique impacts were left out of the dataset, as were any accepted semi-oblique craters. Large candidate craters easily observable using Esri ArcGIS were included, of greater than 20 km length. The survey was not exhaustive, so it is to be considered a semi random sample.

Results and Discussion: The model being tested is shown in Figures 1 and 2. The test is a basic statistical one, intended to show due cause for further studies. For instance, if the candidate paterae represent nearly horizontal impacts then future studies could compare this frequency to oblique impacts on Earth and ask why are there so many on Mars? The test undertaken, discerning the degree of each non-equatorially aligned approach angle, might be judged positive if the compass heading of a proposed impact is greater than the current angle of the ecliptic plane to the Martian equatorial plane. However, over a 10 million year scale the obliquity of the Martian celestial pole to the equator may reach 35° periodically [6], while currently it is around 25°. As such, 35° was taken as the lower limit to represent a significant compass heading relative to the hypothesis, so comprising a fairly stringent test. In Fig 1, the specific patera under study is the Orcus patera, and a hypothetical pre-Orcus asteroid would have had the orbital angle shown.

In Fig 2 the phenomenon of orbital decay is pictured, illustrating that the final outcome of the proposed interaction is a collision. The impactor

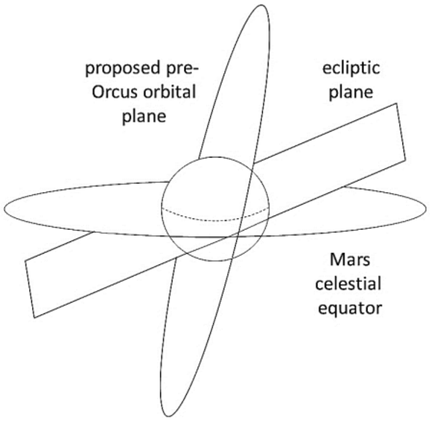

Figure 1. The relationship of the proposed orbit of a pre-Orcus asteroid relative to the plane of the ecliptic and the Mars celestial equator.

Table 1. Martian paterae >20 km long and other features potentially related to candidate oblique impacts

Ident	Co-ord N	Co-ord E	Name if any	Heading	Length (km)	Width (km)	Depth (km)	Base	Rel	CE
1	15	178.5	Orcus patera	~(60)N	385	145	0.95	F	3&4	N
ehdW	18.5	120		~(45)S	39.5	13.5	0.15	U?		N
peridE	25	90		~(30)S	24.5	11	0.15	U		N
huySl	-21	54.5		~(85)S	78	27.5	1.8	U		Y?
huySs	-19.5	54		~(80)S	49	20	0.2	F		N
gillW	16	3		~(60)S	133	47	1	U		Y
becNs	26	344.5		~(85)S	30	15.5	0.9	U		N
becNl	26.5	350		~(45)S	66	26	0.5	U		N
mclW	21.5	334.5		~(85)s	53	19.5	0.1	F		N
sahN	-21	72		~(88)S	98.5	49	0.75	F		N
briS	-16.5	86		~(35)S	58	14	0.2	F		N
lopS	-17.5	95.5		~(35)S	86	19.5	0.5	F		N
2 harS	15	76.5		~(88)S	25	14.5	0.75	U	5	Y
3	32	183	Erebus S	-	46.5	42.5	~0.2	F	1	
4	36	187	Erebus N	-	128	119	+0.05	F	1	
5	14.8	76.5		-	13.5	11.5	0.5	U	2	

Key. **Ident:** numerical identifier for discussion, or direction from a nearby named crater. **Coord:** N North, E East. **Heading:** direction impactor was heading towards, ( )N is degrees angled north from equatorial plane, ( )S is degrees angled south from equatorial plane. **Width:** is max width. **Base:** partially filled F or essentially unfilled U or ?. **Rel:** potentially related to which other impact on the list if any. **CE:** Clear ejecta blankets Y/N. [**Above line:** nominally a primary. **Below:** nom secondary impact]

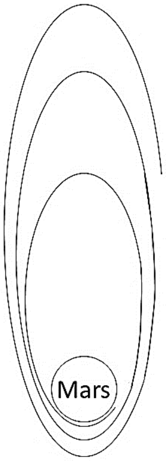

Figure 2. Orthogonal view of a decaying elliptical orbit of a proposed pre-Orcus asteroid.

approaches from over or rather under the horizon and encounters a long curved contact envelope with the relatively dense lower Martian atmosphere, perhaps denser at the time the impact may have occurred. A piece of proposed meteoritic material from such an impact on earth showed a 5 mm putative fusion crust [3], much thicker than for orthogonal impacts, due perhaps to a long fetch of contact.

In Table 1, the example of Orcus patera is tested by surveying other similar paterae on Mars, many smaller than Orcus patera but >20 km length, though some were also found under 20 km long. Two craters are clear candidates for a complex event, namely crater 5 is a potential secondary related to patera 2harS. Classic butterfly ejecta [7] are visible around patera gillW (West of Gill crater). Features of patera observed may indicate direction of approach of impacts. Although these observations could in subtle cases be out by 180°, enough resolution is present in the DEM model to resolve direction fairly well, using such indicators as dip [8], forward banking, forward ejecta and debris.

Regardless of potential 180° errors, the hypothesis proved tentatively supported in that 12 of 13 paterae investigated have compass headings at or well beyond 35° deviation from the Martian equatorial plane. A cursory inspection of smaller near-horizontal paterae also showed a similar pattern of obliquity (not shown).

Additional future focus may fall on the potential secondaries of the proposed pre-Orcus meteorite impact, a case of skipping if so. The largest secondary is a circular crater about 600 km from Orcus patera but while circular it bears a clear debris trail heading distally (northwest) in relation to Orcus patera. The crater is unnamed as far as this writer is aware, however the distal debris trail from it has previously been coined Erebus Montes. This additional hypothesis is consistent with a model whereby: upon first impact, an oblique impactor does break up, and in the case of a large meteorite now shattered, the cluster of its parts can have a joint impact downrange, before being separated and spread further. The momentum of each part only dissipates at its final resting place, and the relative resting places appear inter related through arcs. The observation of such a candidate secondary accords well with computer modeling done by others [1].

References: [1] Elbeshausen D. (2013) *LPS XLIV* Abstr #1916. [2] Haines P. W. (2000). *Catastrophic Events:* Geozentrum, Vienna, Abstr #3093. [3] Moore R.B. (2021) *AGU Fall Meeting* essoar.10509101.1.[4] Moore R.B. MetSoc 2022 Abstr #6133. [5] Meilke P., Fiva A. *et al.* expore-mars.esri.com. [6] Laskar et al.(2002) Nature 419, 375. [7] Herrick R.R., Hessen K.K. (2006) *Met & Planetary Science* 41:1483–1495. [8] Kenkmann *et al.* (2012) LPS XLIII Abstr #1440.

THE MODIFICATION OF UDZHA CRATER IN THE MARTIAN NORTH POLAR LAYERED DEPOSITS.

A. V. Pathare[1], A. Russell[1], A. Howard[1], G. Morgan[1], M. Perry[1], and N. Putzig[1]. [1]Planetary Science Institute (1700 E. Fort Lowell, Suite 106, Tucson, AZ 85719; pathare@psi.edu).

Introduction: We have begun an MDAP-funded study of the modification of surface and buried craters in the Martian polar regions. **Fig. 1** shows the 45-km diameter Udzha Crater (located near the periphery of the North Polar Layered Deposits [NPLD] at 81.8°N and 77.2°E), the interior of which contains thick layered deposits with incipient troughs inside the craggy remnants of its crater rim.

Radar Analysis: Using a depth-converted version of the latest available 3D SHARAD (Shallow Radar) radargram of the north polar region ([1], see https://sharad.psi.edu/3D), we are mapping the near-surface radar stratigraphy within Udzha Crater (**Fig. 3**). We first mapped the well-documented WRAP (widespread recent accumulation package: [2]) throughout Udzha's interior (**Fig. 3a**), and then mapped two other prominent layer packages that are slightly deeper (**Fig. 3b,c**), corresponding respectively to layers "**a**" (green trace), "**b**" (blue trace), and "**c**" (red trace) in the radargram profile shown at the bottom of **Fig 3**.

Interestingly, the blue "b" layer can only be mapped in the deep interior of Udzha (**Fig. 3b**), where it appears to create an angular unconformity with the underlying red "c" layer (**Fig. 3**, bottom). Additionally, the WRAP layer is notably thinner in the deep interior (**Fig. 3a**, central green regions) relative to the rim crest of Udzha that abuts the adjoining NPLD (**Fig. 3a**, dark blue regions). Lastly, we note that our preliminary analysis of SHARAD surface radar returns (**Fig. 2**) indicates that the (non-corrected) surface power distribution of Udzha matches closely with that of the entire NPLD, suggesting similar broad scale near-surface dielectric properties.

Modification History: Collectively, these radar observations suggest that there may have been localized episodes of preferential deposition and erosion within the Udzha Crater cavity. We will model the modification history of Udzha using MARSSIM [3], thereby enabling us to assess the hypothesis of [4] that impact craters act as localized depocenters that drive further accumulation in the NPLD.

References: [1] Foss, F. J. et al. (2017) *The Leading Edge, 36(1)*, 43-57. [2] Smith I. B. et al. (2016) *Science, 352 (6289),* 1075-1078. [3] Howard A. D. (2020) *GSA Annual Meeting,* Abstract #355189. [4] Brothers, T. C. et al. (2015), *JGR Planets, 120(7),* 1357-1375.

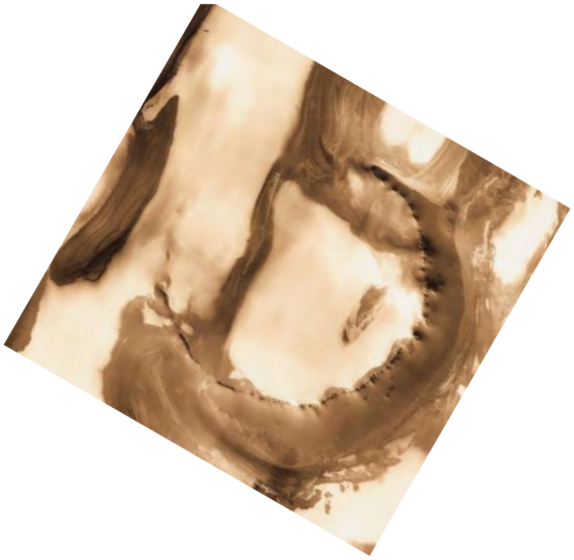

Figure 1: THEMIS (Thermal Emission Imaging System) image of 45-km diameter Udzha Crater, located in the NPLD at 81.5°N and 77.1°E. North is to the upper left. Credit: NASA/JPL-Caltech/ASU.

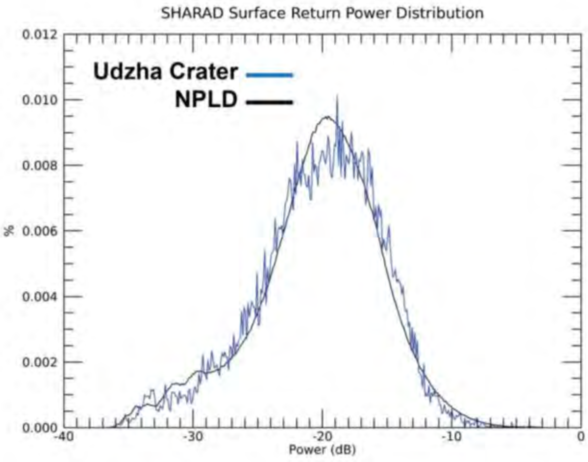

Figure 2: Preliminary SHARAD surface return power distributions (non-corrected) for Udzha Crater (blue line) compared to the entire NPLD (black line).

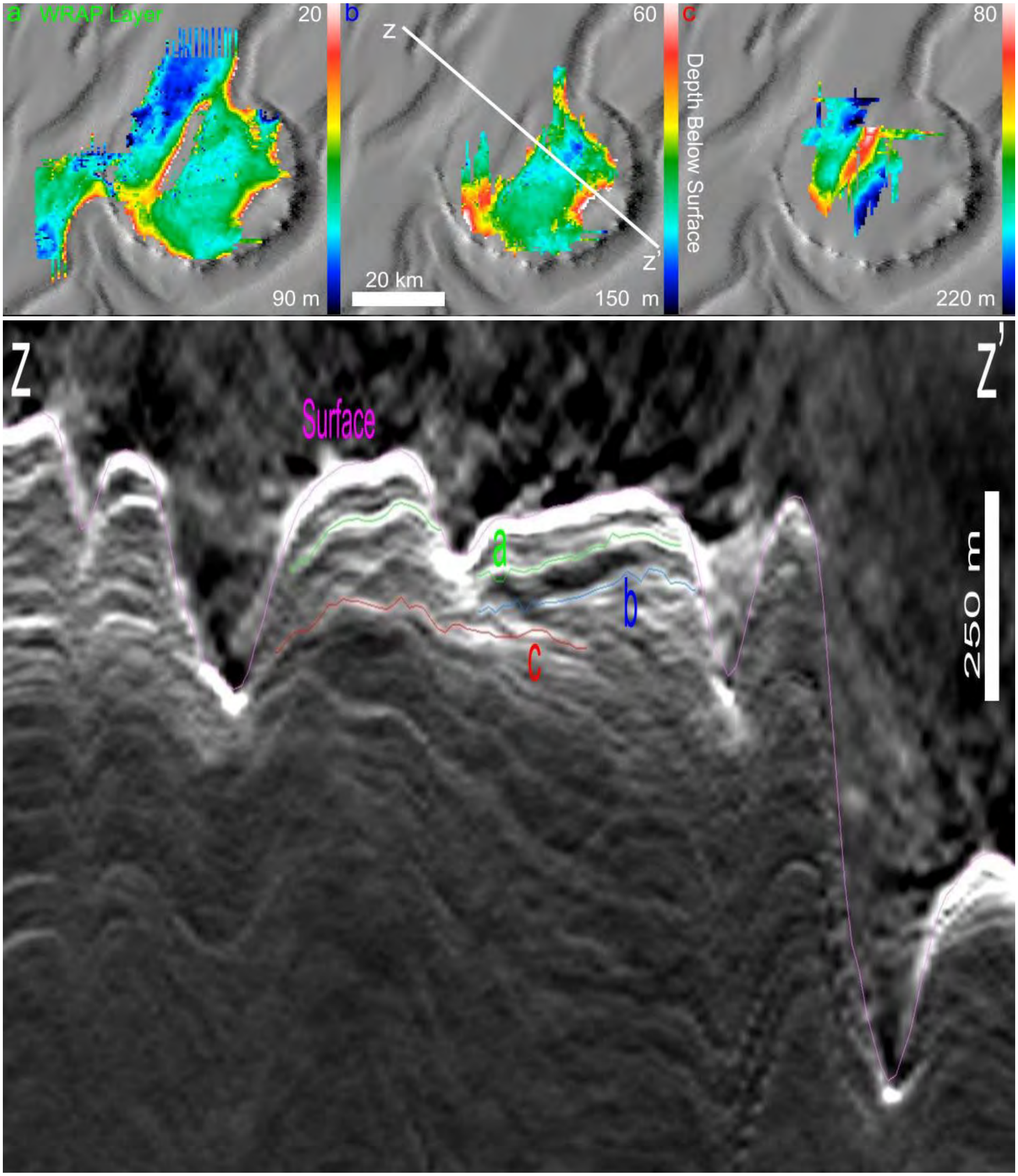

Figure 3: (top) Spatial distribution in the vicinity of Udzha Crater of SHARAD-derived stratigraphic radar layer packages “a” / “b” / “c” – note “a” corresponds to the so-called “WRAP” layer [2]. **(bottom)** SHARAD Radargram along profile (shown in **b**) illustrating tracing of layer packages “a” / “b” / “c” in the interior of Udzha Crater.

Automatic Data Aggregation to Assist in the Systematic Classification of Small Lunar Craters

L. Powers[1], A. Dickinson[1], T. Ways[1], K. S. Martin-Wells[1] [1]Ursinus College (Pfahler Hall, 601 E. Main Street, Collegeville, PA 19426, lipowers@ursinus.edu).

Introduction: Crater counting and classification are foundational to many techniques by which the surfaces of planetary bodies are characterized. However, research has shown that differences in crater counting methods between different crater counting procedures—and even for repeated counts by the same counter—yield variable results.[1] This is likely unavoidable, but are there steps that we can take to make our crater counts as repeatable and transparent as possible, given these inherent limitations?

In this work, we consider the properties that human counters use to determine whether features are craters, as well as what properties have been used in the literature to classify small primary vs. secondary craters on the Moon. We then attempt to capture some of the key elements of this human decision-making by aggregating data that can be automatically extracted from a variety of lunar datasets based on a rough human "guess" of an ellipse that is fit to a crater rim.

While it is unlikely that this automatic data aggregation will be able to replace the counting and classification of human counters, we hope to develop a tool that will allow us to provide more systematic, quantitative rationale for our human classifications, allowing us to be more transparent and repeatable in our crater classifications and counts.

Methods: In developing our data aggregation system, we have considered the ways in which human counters identify craters and what properties have been used by previous workers to distinguish small primary craters from secondary craters. For example, a human counter who is searching for small, fresh lunar primary craters is likely to look for features with circular planforms, raised rims, and depth to diameter ratios of ~1/5.[2] The presence of a well-preserved, azimuthally-symmetric continuous ejecta blanket would indicate a recent impact from near normal, while an uprange zone of avoidance in the ejecta blanket or a "butterfly" ejecta pattern would suggest progressively more oblique impact conditions.[3]

A variety of datasets have been used in the literature to characterize the shape of continuous ejecta and crater rays. Rays and continuous ejecta are evident as albedo features in visible wavelength imagery.[4] Optical maturity also reveals the presence of rays and continuous ejecta, given that for fresh craters, they are composed of optically immature material.[4] Similarly, the rocky ejecta blankets of fresh craters may present as elevated rock abundance features in thermal measurements.[5]

Secondary craters that form at relatively low velocities near their parent craters are often also identified by human crater counters on the basis of their morphology. "Classic" secondary crater morphologies include elliptical planforms, shallow depths relative to crater diameters, v-shaped uprange dunes, downrange braided or textured surfaces, and dense spatial clustering.[6] While secondary craters that form further from their parent craters may produce deeper craters relative to their diameters and more circular planforms due to higher impact speeds, workers have identified even these secondary craters on the basis of properties such as spatial clustering.[1] Downrange "tails" of anomalous thermal inertia and radar CPR have also been recorded in association with distal secondary craters.[7]

Our goal is to automatically extract and aggregate quantitative data that is representative of these kinds of observations, as they are often implicitly gathered by human counters during the process of classification.

Data: Test populations were comprised of pre-selected, well-defined primary and secondary craters ranging between 0.6-2 km that were located near Tycho secondary crater chains with classic secondary crater morphologies. Tycho was selected for study because its well-preserved secondary population has been characterized by other workers, employing a variety of datasets.[6,8-14]

We defined the size of our craters by fitting an ellipse to their rims using the "5-pt Ellipse" tool in the JMARS desktop software program.[15] The major axis of this ellipse was used as our crater diameter. The ellipticity of each crater was also calculated based on this fit. Data for each crater was extracted from the "Clementine UVVIS/Optical Maturity - Numeric" (128 PPD)[16], "Rock Abundance (Full Mission)" (128 PPD)[5,11], and "LOLA 1024 PPD Elevation - Numeric"[17] layers that are available in the JMARS, as well as from a layer of Arecibo-GBT ground based 12.6 cm radar CPR data that was obtained from the PDS and imported into JMARS.[18]

These data were extracted from JMARS using the Map Sampling tool, outputting the average and maximum pixel value of the region within the area of the ellipse that was created during counting. These values, and the ratio between the average and maximum, were then compared to set parameters for the counting region. This method was also used over a circle created 1.5 crater radii larger in diameter with respect to the original crater, in order to analyze the possible ejecta blanket of these craters. This data was in turn compared to the pixel values from within the crater rim from the original count.

Elevation profiles were extracted from the LOLA 1024 ppd Elevation layer along four transects of each crater at 45 degree azimuthal spacing. In future work, these elevation profiles will be used to fit depth to diameter ratios for each crater. The relative degree of clustering of each crater will also be computed. Together, these measurements will help to capture some of the key components that human counters use to distinguish between the morphology of secondary craters and small primary craters.

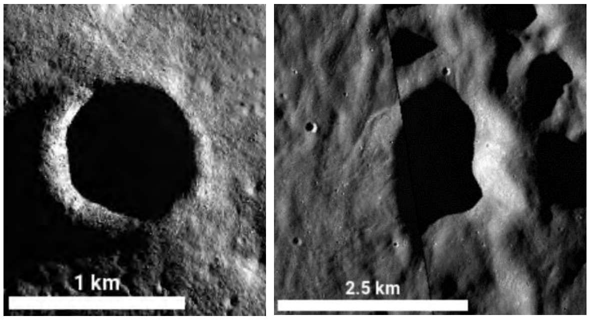

Figure 1: (Left) LROC NAC mosaic image of example primary used in preliminary testing, -54.336°N, 352.992°E, NAC Product ID:M1123625005RC. (Right) LROC NAC mosaic image of example secondary used in preliminary testing, -58.806°N, 345.053°E NAC Product ID: M1111896762RC, M1111896762LC.

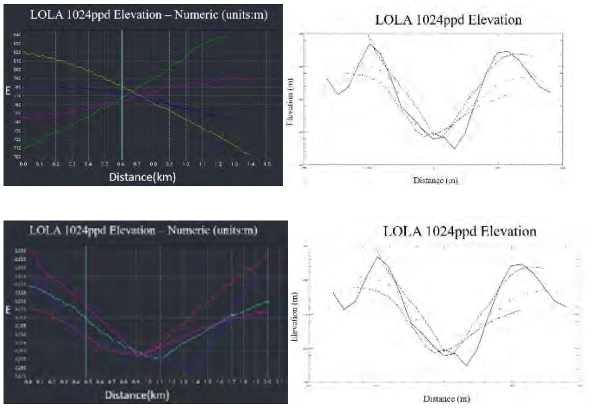

Figure 2:(Top left) Elevation profile plot extracted from JMARS for example primary crater in Figure 1. (Top right) Corresponding elevation plot generated with extracted LOLA data for example primary. (Bottom left) Elevation plot extracted from JMARS for example secondary crater in Figure 1. (Bottom right) Corresponding elevation plot generated with extracted LOLA data for example secondary.

Conclusions: Using a classical example of a primary and secondary crater with diameters of 0.82 km and 1.82 km respectively, our model showed definable differences between the two in average pixel values of optical maturity, rock abundance, and radar polarization data. We observe that for some craters below ~1.5 km in diameter local topography dominates in elevation profiles, as shown in Figure 2. This produces unique challenges when creating depth-to-diameter ratios and will be the subject of future work.

Other difficulties that remain to be addressed include the differences in registration of the different datasets in JMARS, which skews the results of automatic data extraction based on the ellipse centers fit relative to the LROC WAC and NAC data. However, with further testing and development, we hope to produce a systematic data aggregation and recommendation procedure that will make our crater counts and classifications more transparent and repeatable.

Acknowledgments: We gratefully acknowledge the JMARS software and associated PDS data products, without which this work would not have been possible.

References: [1] Robbins, S.J., et al. (2014) *Icarus, 234*,109-131. [2] Melosh, H.J. (1989) *Oxford University Press.* [3] Herrick, R.R. and Forsberg-Taylor, N.K. (2003) *Meteorics & Planet. Sci., 38*, 1551-1578. [4] Hawke, B.R. et al. (2004) *Lunar and Planet. Sci. Conference LX.* [5] Bandfield, J.L., et al., (2011), *J. Geophys. Res. 116*, E12. [6] Lucchitta, B.K.(1976) *Icarus, 30*, 80-96. [7] Martin-Wells, K.S. et al. (2017) *Icarus, 291*, 176-191. [8] Campbell, B.S., et al. (1992) *Proc. Lunar Planet. Sci. Conf. 22nd*, 259-274. [9] Plescia, J.B. and Robinson (2019) *Icarus, 321*, 974-993. [10] Krüger, T., van der Bogert, C.H. and Hiesinger, H. (2016) *Icarus, 273*, 164-181. [11] Bandfield, J.L. et al. (2017) *Icarus, 283*, 282-299. [12] Dhingra, D., Head, J.W. and Pieters, C.M. (2017) *Icarus, 283*, 268-281. [13] Zanetti, M. et al. (2017) *Icarus, 298*, 64-77. [14] Bray, V.J. et al. (2018) *Icarus, 301*, 26-36. [15] H. Riris, J. et al. (2017) *Proc. SPIE 10565, International Conference on Space Optics — ICSO* 2010. [16] Lucey, P. G., G. J. Taylor, and E. Malaret, (1995), *Science, 268*, 1150-1153. [17] Riris, H., et al. (2017) *Proc. SPIE 10565, International Conference on Space Optics — ICSO 2010.* [18]Campell, B. A., (2010) *Icarus, 208,* 565-573.

PROGRESS TOWARDS DERIVING NEW EMPIRICAL CRATER PRODUCTION FUNCTIONS FOR VOLCANIC TERRAIN ON MERCURY, MOON, AND MARS.

S.J. Robbins*[,1] *stuart@boulder.swri.edu. [1]Southwest Research Institute, 1050 Walnut Street, Suite 300, Boulder, CO 80302.

Overview: The venerable crater production function (PF) describes the size-frequency distribution (SFD) of impact craters that form on a planetary surface. That PF is dependent on the impactor population that formed the craters and the terrain into which that population impacted. A model-based PF convolves those effects with various scaling laws in order to develop the model PF. An observation-based or empirical PF will attempt to identify only a population of craters that has not been modified since they formed, and one that only consists of those craters which formed from extra-planetary impactors (*e.g.*, not secondary craters, not volcanic pit craters).

The focus of this abstract is on work that I have been doing towards the latter, building a observation-based PF for Mercury, Moon, and Mars. This work has been ongoing since 2015, but evolving methods and datasets that are "almost released" for the last several years have caused it to drag out. Due to further delays, this is a "blind abstract," written without significant results to share, but with the anticipation of those results in time for the August 2022 Planetary Crater Consortium meeting.

Original Proposed Work, Overview: I originally proposed – and was funded – to create a new generation of PFs for D = 0.5–50 km for Moon and Mars, and D = 5–50 km for Mercury. This work is motivated by the fact that the two main PFs in use by the planetary science community disagree by factors of several in the critical D ~2–10 km range [*e.g.*, 1]. It was and is hoped that a new, independent investigation using modern datasets and modern techniques might determine which – if either – is more accurate and release a new reference for the community. The PF is a critical tool for it is against the PF that impactor populations are compared, that craters in certain regions are compared to determine erosion/modification, and they are used for modeling absolute ages of surfaces.

This work is focused on regions that are relatively young (lunar maria, martian volcanic plains, hermean basin floors) to build the PF for smaller impact craters, and it uses the rims of large basins for larger impact craters (basin rims form a mostly cohesive unit, and they are old so retain a record of larger impacts that have not yet had time to form on younger, volcanic terrain). Significant care is being made to avoid secondary impact craters, which is also the primary reason why the PFs will be truncated at the specified minimum diameters. They are truncated at the larger diameters to avoid small-number statistics. This work also focuses on volcanic terrain (except the largest craters) to avoid the effects of terrain strength on the forming crater.

Mars Analysis: Original, Evolution, and Current: The original Mars analysis was to identify impact craters on the calderas of several large supervolcanoes, the two vast, smooth planes of Amazonis and Elysium, and the rims of numerous large crater basins for the large end of the PF. Because of the existing global Mars impact crater database [2], little new work was going to be done.

However, in roughly 2017 (two years into the original three-year project), it was recognized that the THEMIS-based crater database did not hold up well against much better CTX camera images (THEMIS is a thermal infrared camera with images at 100 mpp, while CTX is a visible-light camera with images at 6 mpp). I, along with colleagues at the Southwest Research Institute, embarked on what has so far turned out to be a five-year mission, to seek out new methods and new techniques, to boldly go [sic] where no cartographer had gone before, and create a fully cartographically and cosmetically controlled CTX dataset upon-which craters could be more reliably mapped (among many other scientific endeavors). Now that that dataset for the equatorial region of Mars has been made, and the rest funded, work can return to a wholesale re-analysis and cataloging of Martian impact craters, though on a somewhat reduced surface area due to depleted funds. Fortunately, unrelated funding also requires a new crater mapping exercise over young Martian terrains and to also separate secondary craters, so some additional work can be done that was going to need to be cut out.

Mercury Analysis: Original, Evolution, and Current: The original Mercury analysis was to identify and measure impact craters on several large impact crater floors and rims, mapping each separately and then merging the results to produce the empirical production function. The existing Mercury basemaps that are in the NASA PDS were to be used.

For separately funded work through PGG, I was able to cartographically control all *MESSENGER*-MDIS images in the Rembrandt basin area, producing several mosaic products at a variety of incidence angles, East-West sun directions, and at better pixel scales than are available in the PDS mosaic. These mosaics were much better for identifying impact craters, and I wanted to use the cartographic control tools developed for CTX on Mars to control these Mercury data and make basemaps on which to identify and measure craters.

Unfortunately, several attempts were made, but the nature of the overlapping Mercury data was not appropriate for how our cartographic control code was optimized for CTX images (CTX images have usually very few, small overlaps from one image to another, very similar lighting geometries, and almost identical pixel scales; in contrast, MDIS images often have dozens of images for any given location on the planet with anywhere from dawn to noon to dusk imaging and pixel scales from tens of meters to tens of kilometers, presenting a very different optimization problem). So, while the code works, it was not feasible to do this work for Mercury, despite putting off the crater work for several years trying.

Therefore, I have returned to the originally proposed work and will be done over the coming year: Identify those impact craters on existing basemaps for the $D = 5–50$ km production function.

Moon Analysis: Original, Evolution, and Current: In the original proposal, craters on the Moon would be selected in a similar way to those on Mercury, identifying craters on young lunar maria and on basin rims for larger craters. During the first three years of the period of performance, when not involved with the active *New Horizons* mission, I generated what is now a ≈2.1 million entry global impact crater database [3] for the Moon. Additionally, we received further funding from NASA-PDART to add morphometric and morphologic data (*e.g.*, secondary crater classifications) to each crater $D \geq 1$ km in the database.

The massive database construction that was published in 2018 already meant that the lunar data were gathered in the third year of the three-year SSW. Ergo, this further delayed work.

Ongoing Work, and Wrapping This Project Up in the Next Year: I am in what is the last reasonable year for this work, with all the pieces in place to wrap this up over the coming ≤12 months. At the August 2022 PCC meeting, I will present work to-date and solicit recommendations and comments on how it is progressing and the analysis methods. It is anticipated that this will become a solid, new reference for the community and hopefully resolve the shape of the PF in the areas of most significant disagreement between the work of Neukum and Hartmann, specifically the ~1–10 km range, at least for volcanic and volcanic-like terrain. It will also be among the first empirical works to derive the PF independently for Mars and Mercury rather than use scaling arguments to transfer the PF from the Moon.

Finally, one of the primary lessons learned so far from this effort has, however, been learned: Don't let "perfect" be the enemy of "good enough." Additionally, there does come a point where one cannot rely on better data to come out that will make their project better [4].

References: [1] Neukum *et al*. (2001) doi: 10.1023/A:1011989004263. [2] Robbins & Hynek (2012) doi: 10.1029/2011JE003966. [3] Robbins (2018) doi: 10.1029/2018JE005592. Gottbrath *et al*. (1999) arXiv: https://arxiv.org/abs/astro-ph/9912202

Funding: The current and future overall work for all three bodies comes from NASA SSW NNX15AH97G. Some work for Mercury was performed on NASA PGG NNX14AP51G. The initial Mars work was done on NASA NESSF NNX07AU85H and MDAP NNX10AL65G, while some future Mars work will also be done on NASA MDAP 80NSSC21K1427. Some of the lunar work was funded in part by the Maryland Space Grant award for CosmoQuest support, *Lunar Reconnaissance Orbiter* LAMP instrument as a Participating Scientist, and NASA SSERVI Award "ISET" to Southwest Research Institute NNH13ZDA006C. Some of the future lunar work is also being done through NASA PDART NNX17AL05G.

MODELING A PLANETOCENTRIC SOURCE OF IMPACTORS FOR THE URANIAN SATELLITES.

N. L. Rossignoli [1,2] and R. P. Di Sisto [1,2], [1]Instituto de Astrofísica de La Plata, CCT La Plata - CONICET - UNLP, 1900 La Plata, Argentina (nrossignoli@fcaglp.unlp.edu.ar), [2]Facultad de Ciencias Astronómicas y Geofísicas, Universidad Nacional de La Plata, 1900 La Plata, Argentina

Introduction: The system of Uranus and its regular moons presents unique characteristics to explore different cratering populations. Uranus' large spin-axial tilt has motivated multiple studies based on a giant impact that could also lead to the formation of its regular satellites from the resultant debris disk (e.g. [1–4]). Recently, a study by Woo et al. [4] has been able to reproduce the observed mass and bulk composition of Uranus' satellite system by accretion from an impact generated disk. Naturally, after the formation of the moons a residual mass is left which could compose a planetocentric source of impactors for the recently formed satellites.

In a previous study [5], we have modeled the impact cratering process on the five mid-sized satellites of Uranus considering heliocentric impactors originated in the Scattered Disk. When comparing our results with the observational crater counts [6, 7] we found that an alternative impactor population may be necessary to explain the highly cratered surfaces of Umbriel, Titania and Oberon. On this basis, in this work we model planetocentric sources of impactors resulting from a residual disk after the moons formation that can account for the reanalyzed observational crater counts by Kirchoff et al. [8].

Methodology: In order to model a planetocentric source of impactors for the mid-sized Uranian satellites we explore different profiles for planetocentric disks with a positive trend in the mass-distance distribution. For the simulation, we consider disks that spread between 3 $\mathrm{R_U}$ and 30 $\mathrm{R_U}$, where $\mathrm{R_U}$ is Uranus' radius. The number of particles in each disk is given by $N(a) \propto a^n$, where n varies between $n = 1/2$ for Disk 1 and $n = 5/2$ for Disk 4. Given that the residual debris disk is expected to be excited after the satellites' formation, we model the particle parameters for the simulations with semimajor axes between 3 $\mathrm{R_U} \leq a \leq$ 30 $\mathrm{R_U}$, inclinations between $0° \leq i \leq 15°$ considering Uranus's positive spin axis as its north pole and eccentricities between $0 \leq e \leq 0.25$, while the rest of the orbital parameters take random values. We then simulate the dynamical evolution of the disk particles over 10 million years considering the current configuration of the Uranian satellite system. At the end of the simulation we compute the collision probability for each satellite and the impact velocity. With these results, we build a cumulative size distribution (CSD) of the planetocentric impactors, calibrating the results of the simulation with Oberon's crater counts presented in Kirchoff et al. [8].

The CSD of these impactors is given by:

$$N(>d) = C\left(\frac{1\mathrm{km}}{d}\right)^q \qquad \text{for} \qquad d \gtrsim 1\ \mathrm{km}, \tag{1}$$

where q=2 and C is found to be highly dependent on the disk model and varies between $C = 44655$ for Disk 1 and $C = 27119$ for Disk 4. The modeled CSD is then used to compute the planetocentric crater distribution on Miranda, Ariel, Umbriel and Titania and compare our results with the updated crater counts [8].

In order to obtain the transient crater diameter D_t as a function of the impactor diameter d we use the crater scaling law [9]:

$$D_\mathrm{t} = K_1\left[\left(\frac{gd}{2v_\mathrm{i}^2}\right)\left(\frac{\rho_\mathrm{t}}{\rho_\mathrm{i}}\right)^{\frac{2\nu}{\mu}} + K_2\left(\frac{Y}{\rho_\mathrm{t} v_\mathrm{i}^2}\right)^{\frac{2+\mu}{2}}\left(\frac{\rho_\mathrm{t}}{\rho_\mathrm{i}}\right)^{\frac{\nu(2+\mu)}{\mu}}\right]^{-\frac{\mu}{2+\mu}} d, \tag{2}$$

where g and ρ_t are the target's gravity and density respectively, μ=0.38, ν=0.397, K_1=1.67, K_2=1 and Y=1 MPa. For the impactor density we use $\rho_\mathrm{i} = 1\ \mathrm{gr\,cm^{-3}}$. The final crater size D is obtained considering that above a certain impact energy, craters collapse into complex shapes.

Results and Discussion: General results: Mean satellite radius R_s and semimajor axis a in km, collision velocity v_i in km/s for disks D1 and D4, collision probability for disks D1 and D4.

Satellite	R_s	a	v_i [D1]	p [D1]	v_i [D4]	p [D4]
Miranda	235.8	129900	1.59	0.03	1.83	0.01
Ariel	578.9	190900	1.38	0.11	1.55	0.05
Umbriel	584.7	266000	1.23	0.14	1.33	0.1
Titania	788.9	436300	1.20	0.31	1.16	0.35
Oberon	761.4	583500	1.03	0.32	1.05	0.41

In this section we present the predicted planetocentric crater distributions for the five mid-sized Uranian satellites. Figs. 1 and 2 show the cumulative number of craters per square kilometer as a function of crater diameter for both disks D1 and D4 and the heliocentric model [5], together with observed crater counts for the 'cratered dense' terrain in Miranda and the 'cratered' terrain in Ariel as presented in Kirchoff et al. [8].

Our results in Fig. 1 show that for the cratered terrains of Miranda and Ariel, the predicted crater distribution obtained with the Disk 1 model overestimates the number of observed craters, while the Disk 4 results fit the observed distribution in Ariel but underestimate the number of observed craters in Miranda. Considering that both satellites show evidence of endogenic resurfacing, it may be possible that many craters have been obliterated

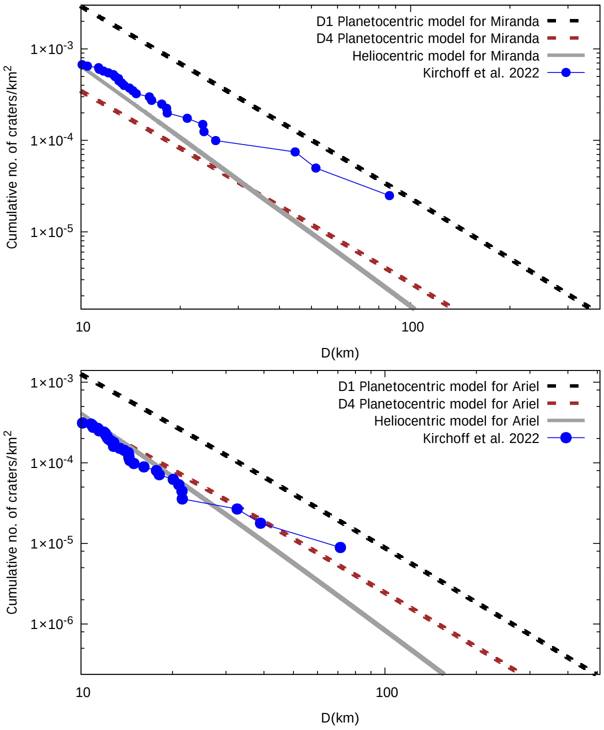

Figure 1: Cumulative number of craters per square kilometer on Miranda (top panel) and Ariel (bottom panel) as a function of crater diameter. Dashed lines represent the modeled planetocentric crater distributions for disks D1 and D4, gray solid line indicates the heliocentric crater distribution [5] and color points indicate observed crater counts [8].

over the age of the Solar System, which is consistent with an overestimation of the number of predicted craters in the Disk 1 model.

Our results for Umbriel, Titania and Oberon (Fig. 2) show that a planetocentric source of impactors may be able to account for the observed crater distributions in these satellites, particularly for the Disk 1 model. In fact, our results are consistent with Oberon and Umbriel exhibiting densely cratered surfaces, while Titania has a lower crater frequency which may indicate that it has been endogenically resurfaced.

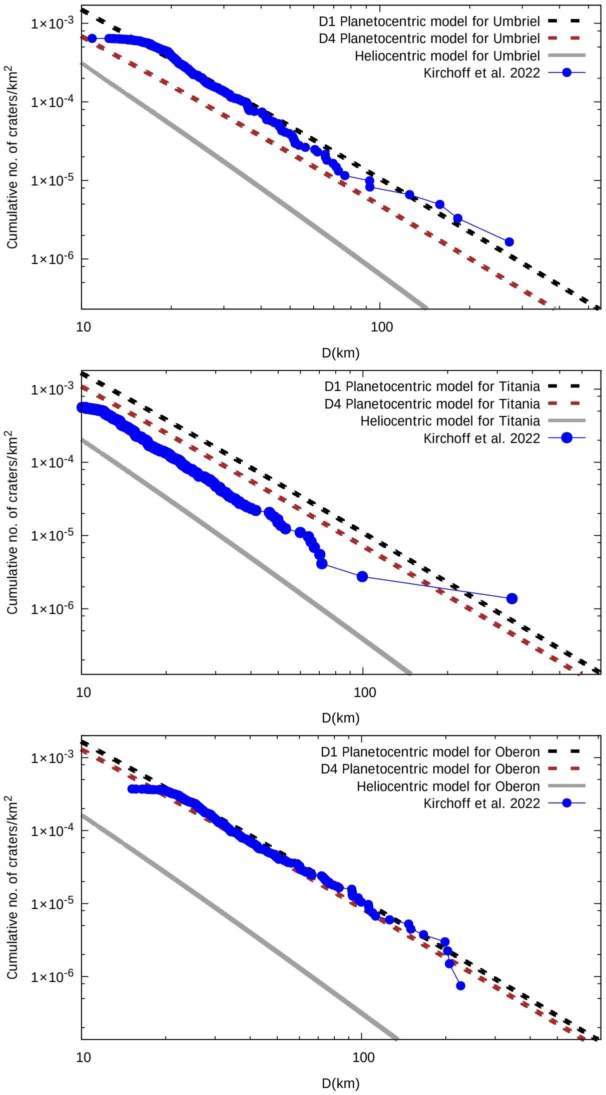

Figure 2: Cumulative number of craters per square kilometer on Umbriel (top panel), Titania (middle panel) and Oberon (bottom panel) as a function of crater diameter. Dashed lines represent the modeled planetocentric crater distributions for disks D1 and D4, gray solid line indicates the heliocentric crater distribution [5] and color points indicate observed crater counts [8].

References: **[1]** J. A. Kegerreis et al. *ApJ* 861.1 (2018). **[2]** C. Reinhardt et al. *MNRAS* 492.4 (2020). **[3]** S. Ida et al. *Nat. Astron.* 4 (2020). **[4]** J. M. Y. Woo et al. *Icarus* 375 (2022). **[5]** N.L. Rossignoli and R. P. Di Sisto. In: *12th PCCM*. Vol. 12. LPICo. 2021. **[6]** J. B. Plescia. *Journal of Geophysical Research* 92.A13 (1987). **[7]** R. G. Strom. *Icarus* 70.3 (1987). **[8]** M. R. Kirchoff et al. *PSJ* 3.2 (2022). **[9]** K. A. Holsapple and K. R. Housen. *Icarus* 187 (2007).

REDUCED GRAVITY EJECTA EMPLACEMENT EXPERIMENTS.

K. D. Runyon[1] , O. S. Barnouin[1], C. Tsang[2], D. D. Durda[3], C. M. Ernst[1], H. T. Smith[1], A. Martin[1], A. Nguyen[4] V. Klein[3], [1]Johns Hopkins Applied Physics Laboratory, Laurel, MD USA (Kirby.runyon@jhuapl.edu), [2]Boulder, CO, [3]Southwest Research Institute, Boulder, CO, [4]Vassar College, Poughkeepsie, NY.

Introduction: Impact cratering dominates surface geological processes among solid bodies in the solar system. As a corollary, the excavated and emplaced crater ejecta complement this surface process domination; on even small bodies such as asteroids Ryugu and Bennu, ejecta can be retained [e.g., Richardson et al., 2007; Arakawa et al., 2020; Perry et al., 2022]. Missions to small bodies such as Lucy, Psyche, Mars Moon Explorer, and others, and numerous robotic and even human missions to the Moon, will provide abundant opportunities to better characterize the processes and resulting facies related to ejecta emplacement. Crucially, these upcoming missions will all be on worlds with low gravity (<2 m/s^2).

The concept of *scaling* is important when extending the results of laboratory impact cratering to planetary size and velocity regimes [e.g., Schmidt and Holsapple, 1980; Holsapple, 1993; Housen et al., 1983; Housen and Holsapple, 2011]. Two useful parameters for cratering are the cratering (or excavation) efficiency defined as the *removed mass*/*emplaced mass* or

$$M/m; \qquad \text{Eq. 1}$$

and the inverse-Froude number, π_2, as the product of the body's gravity and the size scale (impactor diameter or ejecta curtain width) divided by the square of the velocity, or

$$\pi_2 = 3.22gr/v^2, \qquad \text{Eq. 2}$$

where 3.22 is a factor used for experimental historical consistency [Schultz and Gault, 1985]. Laboratory results [Runyon and Barnouin, 2018] show that granular ejecta slides, erodes, and mixes with granular regolith following deposition, leading to geologically interesting stratigraphy. These experiments were not sufficient in number however to show whether any scaling rules exist for ejecta deposition; hence more work has been needed.

Figure 1. The glovebox with the ejecta catapult in parabolic flight. Note the six armholes (partly obscured). Video still credit: Zero-G/Steve Boxall.

Two questions in our ongoing research are, "How does crater ejecta mobilize regolith on small bodies?" and "Does ejecta emplacement follow scaling rules, especially power laws?" Unlocking the secrets of the evolution of small bodies requires correlating samples and surface units to their provenance and providing geologic context for returned samples. This geologic goal benefits from reduced gravity experiments to understand the interplay between chaotic granularity effects and the slow (few cm/s) deposition and runout speeds expected on small bodies. Our experiments are uniquely tailored to understanding transport histories and dynamics (e.g., implantation, exhumation, mobilization) of geologic materials on small bodies.

Methods: To understand ejecta emplacement on worlds with low gravity, we designed an experimental apparatus for inclusion on a reduced-gravity parabolic flight on The Zero Gravity Corporation's ("Zero-G") modified Boeing 727-200 aircraft. A six-arm-hole glovebox contained an ejecta catapult and regolith-ejecta simulant target trays filled with sand (Fig. 1 & 2). The catapult simulates a portion of a granular ejecta curtain using colored sand, and enables studying ejecta dynamics and deposits without needing to also simulate the progenitor crater (Fig. 2); it is based on a much larger, ground-based facility in the Planetary Impact Lab at Johns Hopkins APL [Runyon and Barnouin, 2018].

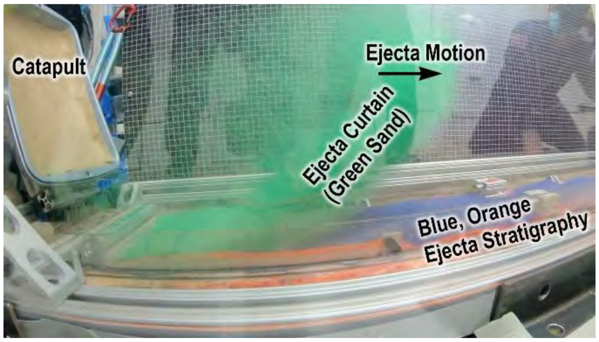

Figure 2. GoPro video still from a Martian gravity (~3.72 m/s^2) parabola showing an ejecta curtain and deposit made of green sand being emplaced over prior deposits of blue and orange sand. The just-fired catapult is seen on the left; the two springs are visible behind it. Reflections of personnel are visible in the glovebox sides. GoPro camera lens distortion renders the straight metal sides to appear curved.

Our parabolic flight campaign began in December, 2021 and consisted of 30 parabolas: 10 of Martian gravity (3.72 m/s^2), 10 of lunar gravity (1.62 m/s^2), and 10 of near-microgravity. In actuality, variations in the precision of the parabolas flown allow for moments of milli- or centi-gravity with accelerations on the order of 1-10 cm/s^2; this is very nearly the gravity expected on large asteroids (Fig. 3). By conducting similar catapult ejecta experiments at a range of gravity levels and deposit speeds, we were able to explore a range of π_2 values and thus test the hypothesis that a M/m vs. π_2 power law exists for ejecta emplacement. This experimental setup also allowed us to observe differences in ejecta runout, mixing, and eroding with the sand in the target trays.

Status and Future Work: We are in the midst of analyzing video data for ejecta curtain size and velocity. Preliminary results show that the ground-projected curtain width (r in Eq. 2) is 5 ± 2 cm for both Martian and lunar gravity and 7 ± 2 cm for near-microgravity. Acceleration values for the 10 Martian and 10 lunar gravity parabolas are 3.46 ± 0.20 m/s^2 and 1.45 ± 0.19 m/s^2 for Martian and lunar gravities respectively. For four of the near-microgravity parabolas the acceleration was 0.21 ± 0.19 m/s^2. Fig. 2 shows orange, blue, and green ejecta layers from subsequent ejecta emplacements.

Future analysis of existing data and a follow-on flight will complete the scaling and geologic analyses. Our future flight (scheduled for fall, 2022) will use crushed colored chalk with a size-frequency distribution more akin to asteroidal regolith, such as on Bennu (power-law slope of -3.0 ± 0.2; Burke et al., 2021).

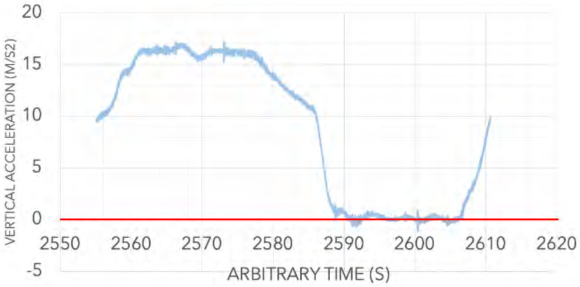

Figure 3. Accelerometer plot from the first "zero" gravity parabola. Note the lower right region in which the gravity oscillates around zero (red line) and spends much of the time very slightly positive, which is ideal for approximating the gravity on asteroids and other small bodies. Catapult ejecta emplacement only takes 2-3 seconds and so can take advantage of slightly-positive-g windows of opportunity.

Supplemental Figure. Co-authors Ernst, Runyon, Tsang, and Smith pose with the experiment during a near-zero gravity parabola. Credit: Zero-G/Steve Boxall.

References: **Arakawa,** M., Saiki, T., Wada, K., Ogawa, K., Kadono, T., Shirai, K., ... & Miura, A. (2020). An artificial impact on the asteroid (162173) Ryugu formed a crater in the gravity-dominated regime. Science, 368(6486), 67-71. | **Burke**, K. N., DellaGiustina, D. N., Bennett, C. A., Walsh, K. J., Pajola, M., Bierhaus, E. B., ... & Lauretta, D. S. (2021). Particle size-frequency distributions of the OSIRIS-REx candidate sample sites on asteroid (101955) Bennu. Remote Sensing, 13(7), 1315. | **Holsapple**, K.A., 1993. The scaling of impact processes in planetary sciences. Annu. Rev. Earth Planet. Sci., 21, 333-373. | **Housen**, K.R., Holsapple, K.A., 2011. Ejecta from impact craters. Icarus, 211, 856-875, doi:10.1016/j.icarus.2010.09.017. | **Housen**, K.R., Schmidt, R.M., and Holsapple, K.A., 1983. Crater ejecta scaling laws: Fundamental forms based on dimensional analysis. JGR, 88, B3, 2485-2499. | **Perry**, M. E., Barnouin, O. S., Daly, R. T., Bierhaus, E. B., Ballouz, R. L., Walsh, K. J., ... & Lauretta, D. S. (2022). Low surface strength of the asteroid Bennu inferred from impact ejecta deposit. Nature Geoscience, 1-6, doi: 10.1038/s41561-022-00937-y. | **Richardson**, J.E., Melosh, H.J., Lisse, C.M., Carcich, B., 2007. A ballistics analysis of the Deep Impact ejecta plume: Determining Comet Tempel 1's gravity, mass, and density. Icarus, 191, doi:10.1016/j.icarus.2007.08.033. | **Runyon**, K. D., & Barnouin, O. S. (2018). Preliminary laboratory investigations of ejecta emplacement dynamics and morphology with planetary applications. Planetary and Space Science, 160, 39-55. | **Schmidt**, R.M., Holsapple, K.A., 1980. Theory and experiments on centrifuge cratering. JGR 85, B1, doi:10.1029/JB085iB01p00235. | **Schultz**, P. H., & Gault, D. E. (1985). Clustered impacts: Experiments and implications. Journal of Geophysical Research: Solid Earth, 90(B5), 3701-3732.

TRACKING INCREMENTAL STRAIN HISTORIES AS A SHOCK WAVE PASSES THROUGH ROCKS DURING METEORITE IMPACT USING CALCITE TWIN ANALYSIS.

A. Schedl, Department of Chemistry and Physics, West Virginia State University, schedlad@wvstateu.edu
.

Introduction: Numerical models have been used to understand impact processes. Recent modeling studies have focused on understanding the strain and stress histories of a meteorite impact [1, 2]. One approach to examining these stress and strain histories is calcite twin analysis, an established technique used in structural and tectonic studies, e. g. [3]. For this abstract I apply a subset of calcite twin analysis, Groshong's [4] calcite strain gauge. The strain gauge determines a strain increment and this increment of strain will be compared to the strain histories given in Rae et al. [2]. Structural and tectonic studies show the strain gauge records the earliest increment of strain, e. g. layer parallel shortening prior to buckling during folding. Two factors explain this behavior, (1) other processes accommodate deformation such as, fracture, faulting, cataclastic flow and (2) twinning is strain hardening, i. e., as strain increases it becomes more difficult to produce additional twins. In this study two structures are examined Serpent Mound, a proven impact crater [5], and Jeptha Knob, a structure that is very likely of impact origin.

Methodology: Groshong's strain gauge [4, 6] is based on the crystallography of calcite and its relationship to twinning. Each calcite grain has three symmetrically equivalent twin planes with poles, e_1, e_2 and e_3 {0112}. Depending on the orientation and magnitude of the principal stresses, twinning may occur on any one of the planes (a twin set) and up to all three of the planes (three twin sets). Each twin set is treated as a 'strain gauge. The amount of shear strain measured by this strain gauge is determined from the twin intensity (twins/mm) and twin widths. The orientation of the twin plane and the c-axis gives the orientation of the individual strain gauges. A least squares regression is applied to a large number of these measurements to find the complete strain tensor for the sample. Principal strains are found by determining the eigenvectors and eigenvalues of the strain tensor. Calcite twinning does not change mineral volume, so the calculated strains are deviatoric strains.

Strain in porous limestone is heterogeneous and the effect of heterogeneity needs to be filtered out. This filtering is done by using the calculated bulk strain tensor for the sample, and then calculating the expected shear strain for each measured twin set. The difference between expected value and the measured shear value for the grain is considered to be noise in the data set. A negative expected value (NEV) implies the twin set has the wrong sense of shear to be twinned for a given bulk strain. The percent NEV is a measure of how homogeneous the strain is. In a deformed rock, NEVs <20% is considered to be homogeneous deformation. The best match between experimentally applied strain (magnitude and direction) and the measured strain was achieved when 20% of the largest magnitude deviations were removed from the data set [6]. The removal of these deviant twin sets is referred to as cleaning.

Groshong's strain gauge measures incremental strains and sometimes calcite twin analysis is able to recognize two deformation events that are at high angles to one another. Teufel [7] investigated using NEVs to identify two deformation events in experiments. For both the perpendicular and 45° data sets the NEVs were ≈40%. The data for the grains with positive expected values (PEVs) were separated from the grains with NEVs making two data sets. The strains were determined for the PEVs data set and the NEVs data set with cleaning applied. The calculated strain magnitudes and directions were consistent with the experimentally applied strains.

High NEVs could also be the result of heterogeneous strain rather than two episodes of deformation. One way of checking is to plotting contoured Turner compression axes on a stereonet. Mechanical twinning initiates when shear stresses on a particular plane in a crystal exceeds ≈10 MPa. As differential stress ramps up, twinning is first initiated, when the **C-axis** is at a 45° angle to the twin plane. Using this initiation condition, the crystallographic *c*-axis, the pole to the twin plane (*e*) and the compression axis (**C-axis**) are assumed to be coplanar, so they have a fixed angular relation to one another. The direction of compression for the rocks is determined by determining the **C-axis** for at least 25 grains/slide, plotting the data on a stereonet and contour the data [8]. The maximum contour gives the approximate compression direction. If the contoured maximum of **C-axes** is well defined on the stereonet and the **C-axes** maxima is roughly coincident with the ε_1 direction and the maxima, then the deformation is not heterogeneous.

In this study the following U-stage measurements were made, the orientation of the *c*-axis for each grain, the poles to the twin plane *e* for each twin set in a grain, the number of twins for each twin set, the width of the twins and the width of the grain perpendicular to the twin plane for each twin set. Using these U-stage measurements, the program CSG [9] determined strain magnitudes and directions, twin intensities and the orientations of the **C-axes** and **T-axes** for each analyzed grain.

Strain results are reported for 5 oriented samples collected from outcrop at Serpent Mound. For these samples two perpendicular thin sections were cut. At Jeptha Knob results from one thin section from a core located at the center of the structure are reported.

Results: In the table below are given the cleaned strain results for 95SPM8 from Serpent Mound along with percent NEV before cleaning. For the Jeptha Knob sample JK 78-1-8 NEV=43%, so the sample was split into positive and negative values and the data were analyzed separately and the results are given in the table below along with the NEVs before cleaning. Also shown in the table is $\sqrt{J_2}$, the square root of the second strain invariant $J_2 = -(\varepsilon_2\varepsilon_3 + \varepsilon_3\varepsilon_1 + \varepsilon_1\varepsilon_2)$ and $\sqrt{J_2}$ is a measure of the total distortion of the rock due to calcite twinning [7].

Table 1: Strain Data Samples 95SPM8 and JK 78-1-8

Sample Number	Strain Direction ε_1		Strain Magnitude ε_1	Strain Magnitude ε_2	Strain Magnitude ε_3	$\sqrt{J_2}$	Twin Intensity	NEV
	Trend (°)	Plunge (°)	(%)	(%)	(%)	(%)	(twins/ mm)	%
95SPM8	229.4	56.9	12.6	-3.96	-8.36	11.2	161	14
JK 78-1-8(PEV)	245.3	76.3	5.67	-1.75	-3.42	5.03	151.3	10
JK 78-1-8(NEV)	137.6	0.7	3.50	0.23	-3.73	3.62	92.7	0

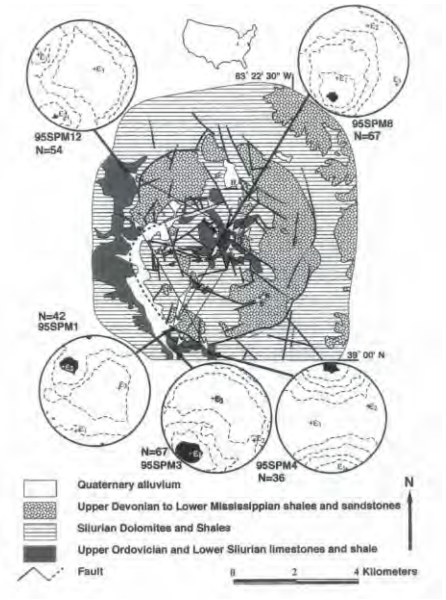

Figure 1: Geologic map of Serpent Mound showing sample locations and ε_1 trajectories at these locations. The filled circles (●) are limestone sample locations and the filled arrowheads connect them to their respective stereonet. On an equal area stereonet, lower hemisphere projection, principal stains (ε_i) are plotted, and **C-axes** are contoured using the Kamb method [8]. Beds have been rotated to horizontal. The lines with double open arrowheads show the projection of ε_1 into map view[10].

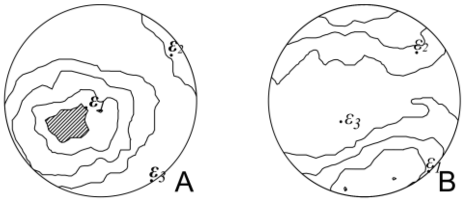

Figure 2: Plots from JK 78-1-8 with bedding rotated into the horizontal plane. **A:** is the stereonet plot of PEV data and **B:** is a stereonet plot of NEV data . **C-axes** are contoured using the Kamb method [8]. Rough coincidence of ε_1 with the contoured maxima of **C-axes** and the bull's eye pattern of the contours indicate that the low percent NEVs in Table 1 is a consequence of two deformation episodes.

Discussion: At Serpent Mound the ε_1 directions converge at the center of the structure (Fig. 1) and the strain ellipsoids are oblate, so calcite strains are caused by the passage of the shock wave [2]. Most samples are collected along the edges or outside the mapped deformation, so shear stresses were below the Hugoniot elastic limit at the time of twinning. Not a surprising result, since the critical resolved shear stress for calcite twinning is 10 MPa. Given the location of most of the samples, there has probably been little lateral movement of the rocks due to impact. Prior to tilt correction the projected elevation of the shock wave source range from -230m to 2750m. After tilt correction elevations range from 900m to 1820m implying 1400±390 m of erosion post impact.. Because of strain hardening and differential stress does not increase much above the Hugoniot elastic at 2-5 GPa [5, 10], so most of the twinning occurs below the Hugoniot elastic limit. The ***K-value*** [11] of sample 95SPM8 is 0.253. Plotting this on Rae et al [2] instantaneous stretching diagram, shows that strain accumulated before peak pressure.

Figure 2 shows two temporally separate deformation events. Figure 2A is taken to be the first event because the deformation is more intense, a higher twin intensity and $\sqrt{J_2}$ (Table 1). The ε_1 direction plunges 76° consistent with the location of the sample. The ε_1 directions shown in figure 2A and 2B are at an angle of 86° to one another. Rae et al. [2] shows there is a 90° rotation of the greatest shortening direction between peak pressure and shock release. The ***K-value*** for the first event is 0.212 and the second event is 1.168 which is consistent with this.

References: [1] Rae A. S. P. e t al. (2019), JGR Planets, 124, 396–417. [2] Rae A. S. P. e t al. (2021), Icarus, 370, 114687. [3] Lacombe O. et al. (2021) Geosciences, 11, 445. [4] Groshong R. H., Jr. (1972) GSA Bull., 82, 2025-2038. [5] Carlton R. W et al. (1998) EPSL 162, 177-185. [6] Groshong R. H., Jr. (1974) GSA Bull., 85, 1855-1864. [7] Teufel L. W. (1980) Tectonophys., 65, 291-309. [8] Kamb W. B. (1959) JGR, 64, 1891-1909. [9] Evans M. A., and Groshong R. H., Jr. (1994) J. Struct. Geol., 16, 277-281. [10] Schedl, A. (2006) EPSL, 244, 530-540. [11] Ramsay, J. G. (1967) Folding and Fracturing of Rocks. 568p.